Ozone removal technologies: activated carbon and MnO_x-based systems

Marzieh Namdari

A Thesis
In the Department
of
Building, Civil, and Environmental Engineering

Presented in Partial Fulfillment of the Requirements
for the Degree of
Doctor of Philosophy (Civil Engineering) at
Concordia University
Montreal, Quebec, Canada

August 2023

CONCORDIA UNIVERSITY
SCHOOL OF GRADUATE STUDIES

This is to certify that the thesis prepared
By: Marzieh Namdari
Entitled: Ozone removal technologies: activated carbon and MnO_x-based systems
and submitted in partial fulfillment of the requirements for the degree of

Doctor of Philosophy (Civil Engineering)

complies with the regulations of the University and meets the accepted standards with respect to originality and quality.
Signed by the final examining committee:

_____ Chair
Dr. Javad Dargahi

_____ External Examiner
Dr. Jianshun (Jensen) Zhang

_____ External to Program
Dr. Alex De Visscher

_____ Examiner
Dr. Catherine Mulligan

_____ Examiner
Dr. Zhi Chen

_____ Thesis Supervisor (s)
Dr. Fariborz Haghighat

_____
Dr. Chang-Seo Lee

Approved by _____
Dr. Chunjiang An, Graduate Program Director

August 23, 2023

_____
Dr. Mourad Debbabi, Dean
Gina Cody School of Engineering and Computer Science

Abstract

Ozone removal technologies: activated carbon and MnO_x-based systems

Marzieh Namdari, Ph.D.

Concordia University, 2021

This study focuses on ozone removal technologies and their performance in various conditions. Ozone is a highly reactive gas and a critical air pollutant, with a permissible workplace level of 100 ppb over 8 hours, according to OSHA. To address the risks associated with high outdoor ozone concentrations and active ozone emission sources, the use of ozone removal technologies is essential.

Various air treatment technologies, such as activated carbon-based media, and catalytic and photocatalytic decomposition systems, have been employed for ozone removal. However, there is limited insight into choosing the best technology based on specific application requirements. This study aims to fill that gap by systematically evaluating ozone removal using granular activated carbon (AC) and granular manganese oxide-cuprous oxide catalysts. The study found that coconut shell-based AC has substantial ozone removal capacity at moderate and mild concentration levels (<200 ppm, >95% efficiency), even surpassing the catalyst. However, all ACs experience deactivation at high concentrations. Catalysts, on the other hand, exhibit a gradual decline in active sites over time. The material properties were found to be closely linked to the ozone removal capacity.

To gain a broader perspective on ozone removal technology feasibility, a statistical approach using the fractional factorial method was employed. This approach considered ozone concentration, humidity level, airflow rate, and media volume, and their effects on the performance of different granular materials. The study revealed that humidity can significantly affect the performance of materials, depending on their physicochemical properties. Among the tested materials, the granular MnOx-based catalyst (CAT-E) demonstrated the best overall performance.

The research also addressed the deactivation issue of MnOx-based catalysts caused by water molecules, particularly at high humidity levels. Physicochemical modifications were investigated through synthesis methods and metal doping. These modifications improved the efficiency of the catalysts, with Ce-doped catalysts showing promising results. However, prolonged exposure to high humidity led to efficiency loss (at 80% RH <20% efficiency 6 h post exposure). To overcome

this, a novel modification technique involving a hydrophobic polymer (poly(vinylidene fluoride)) mixed with catalytic media was employed, resulting in significantly enhanced performance (at 80% RH >50% efficiency 6 h post exposure).

Overall, this study sheds light on ozone removal technologies, their performance under different conditions, and potential modifications to enhance efficiency. These findings have implications for improving ozone removal systems in various applications.

Dedications

to

My parents, Sousan and Ehsan

and

My lovely husband, Amin

Acknowledgements

Firstly, I would like to deeply thank my supervisor, Professor Fariborz Haghighat, for his support, encouragement, patience, and enthusiasm and for his efforts in guiding me through my Ph.D. journey. I appreciate him for giving me the opportunity to work in his lab and for ensuring that I have access to all the required facilities and equipment. He provided outstanding mentorship and training for me during my Ph.D.

I sincerely thank Dr. Chang-Seo Lee for her immense guidance throughout the course of my studies. Her unwavering support has been a constant source of inspiration. She always went the extra mile to teach me problem-solving skills and share her bright perspective, both as a great mentor and a friend.

I would like to extend my gratitude to Professor Mohammad R. K. Mofrad for giving me the opportunity to be a visiting student in his esteemed group at the University of California, Berkeley. I am grateful for the knowledge and skills that I have acquired. I appreciate him for allowing me to use his lab's facilities and resources.

I would like to thank the members of my thesis committee, Dr. Catherine Mulligan, Dr. Alex De Visscher, Dr. Zhi Chen and Dr. Jianshun (Jensen) S. Zhang. Their invaluable advice, comments, and suggestions have greatly contributed to the development of my research.

I am also greatly thankful to Mr. Luc Demers and Ms. Hong Guan for their invaluable assistance during the challenging technical aspects of my research.

I am profoundly grateful to my parents, Sousan and Ehsan, and my siblings, Mohammad and Mahta, for their unconditional love and being the source of my strength throughout my life. Their belief in me and their constant encouragement shaped the person I am today. Thank you for always being there for me.

And, I thank my beloved husband, Amin, for his abundant love, support, and encouragement. Thank you for having belief in my abilities and motivating me and pushing me to broaden my horizons and strive for the best. I feel incredibly fortunate to have you by my side, as you not only listen to my thoughts and ideas but also offer the best advice. Thank you for being my best friend.

Table of Contents

List of Figures

List of Tables

Chapter 1. Introduction

Preface

In accordance with the "Concordia Guidelines for Thesis Preparation", this dissertation is presented in a manuscript-based format. A brief introduction to the subject-matter of this thesis, its objectives and a summary of presented manuscripts and authors' contributions are presented in Chapter 1. Chapter 2 presents an up-to-date and detailed survey of the relevant literature. Chapters 3 to 5 present three original research manuscripts. Finally, thesis conclusion and suggestions for future works are presented in Chapter 6.

1.1. Background

Ozone is one of the most critical inorganic pollutants due to its high reactivity. It has various applications in the industry as an oxidizing agent [1], [2]. Because ozone cannot be stored nor transported in containers, it has to be generated in situ by industrial ozone generators [3], [4]. Therefore, in the industrial environment, ozone generators that work continuously are the main sources of ozone [5]. Ozone leakage can occur since it can destruct ozone generator components and relevant vessels such as tanks, piping, gaskets, joint sealers, and valves [5], [6]. A large number of workers and occupants that deal with ozone generators and other instruments or processes that produce it are at risk of exposure to high levels of ozone. The concentration of ozone has to be monitored precisely near the ozone generator and in the exhaust gas of the system. If any leakage happens, evacuation procedures must be processed [5]. Thus, applying ozone removal technology is highly essential for workers' and occupants' health. Additionally, because of the low solubility of ozone in water (0.456 l O_3/ l H_2O at 15°C [7]), the off-gas flow of the ozone generator system contains high levels of ozone that must be destructed before venting to the atmosphere to protect the environment [5].

Various types of media including activated carbons (ACs), catalysts, and photocatalysts have been studied for ozone removal. AC destructs ozone through chemisorption mechanism, which results in the production of oxygen, CO_2, and CO [8], [9]. The ozone removal efficiency of different kinds of ACs like granular activated carbon (GAC) and activated carbon fiber (ACF) is studied in literature [8], [10], [11]. Stronger chemisorption between ozone and adsorption sites is a key factor. For instance, the ozone removal efficiency of carbon nanotube supported on quartz fiber (CNT/QF) filter is higher than the ACF filter, while the surface area of ACF is far higher than CNT/QF. This is due to the much stronger chemisorption of ozone on CNT [12].

Meanwhile, AC based filters have some drawbacks: AC is combustible, which is hazardous in industrial environments. In addition, the filters become deactivated in a short time; therefore, they need regular replacement following disposal of the used filter. Moreover, ozone can destroy the pore structure of porous filters. For instance, it can shift the pore size distribution of the porous AC filter to larger values. Furthermore, the formation of harmful secondary organic pollutants such as formaldehyde and acetaldehyde through the reaction of ozone with organic compounds is another disadvantage, since the deposition of dust and soot on the filters is inevitable [10], [13]–[15]. The main disadvantage of AC-based filters is their low ozone removal efficiency during long term exposure to ozone, which makes them unstable.

Decomposing ozone into harmless products using photocatalysts and catalysts can be a promising ozone removal technology due to the moderate reaction conditions, high efficiency, and low cost [16]–[18]. According to the following reaction (Equation 1.1), the process of decomposing ozone is thermodynamically favored [19].

$$O_3 \rightarrow {}^{3}/_{2}\, O_2 \qquad \Delta G^{0}_{298} = -163\ KJ.mol^{-1} \tag{1.1}$$

Ozone decomposition reaction can take place on semiconductor materials such as titanium dioxide (TiO_2), which are activated by absorbing light, usually ultraviolet (UV) radiation. This technique is known as photocatalytic oxidation (PCO). Semiconductor materials generate positive holes after absorbing light and become activated. Their subsequent interaction with water results in the formation of hydroxyl radicals, which can initiate the ozone decomposition process [13]. One of the most popular semiconductors that is studied as a photocatalyst is TiO_2 [13], [16], [20]–[23]. The overall photocatalytic ozone decomposition reaction using TiO_2 as a photocatalyst is [16]:

$$O_3 \xrightarrow{TiO_2\ \ hv \geq 3.2\ ev} {}^{3}/_{2}\, O_2 \tag{1.2}$$

The photocatalytic activity of TiO_2 is affected by specific surface area and crystal structure. TiO_2 can have three phases of anatase, rutile, and mixture of anatase-rutile. The rutile phase has the highest activity, and anatase has the least [16], [20]. According to the reports, the ozone conversion of pure TiO_2 photocatalyst decreased rapidly after a period due to the oxidation of the TiO_2 surface by ozone and the formation of an oxidation layer on its surface [21], [22].

There are various catalytic materials for the decomposition of ozone at room temperature such as metals, metal oxides, zeolite, and perlite. Also, the use of transition metal oxides supported on Al_2O_3, SiO_2, TiO_2, and AC was reported for ozone catalytic decomposition [18], [21], [24]. Among

them, MnO_x-based catalysts gained more interest due to their highest catalytic activity, which is attributed to the manganese ability to form oxides with different oxidation states, as well as low price (compare with noble metals), and good stability [17], [24]–[29].

According to the results of recent studies, the density of oxygen vacancies on the surface of the MnO_x catalyst, in addition to its reducibility are responsible for the ozone decomposition efficiency of the catalyst. A catalyst with the higher surface area has a higher density of oxygen vacancies, i.e., the higher density of active sites. Therefore, the morphology and the structure of the catalyst are also of great importance [24]–[26], [28], [29]. However, excessive formation of oxygen vacancies (bulk oxygen vacancy) results in changing the crystal structure and charge distribution significantly, which is not beneficial for ozone decomposition [30], [31].

Several modification procedures are applied to improve the catalytic performance of the MnO_x catalyst. For instance, changing the Mn^{2+} precursors [32], the variation of calcination temperature [33], doping Mn with other transition metal oxides [17], [25], [34]–[36], acid treatment [29], [37], and coating or impregnating the catalyst on a support [26], [38]. Each of these modifications have several effects including enhancement of specific surface area, increasing the adsorption capacity, improvement of oxygen vacancies dispersion, increasing the oxygen vacancy density, increasing the ratio of Mn^{3+}/Mn^{4+}, strengthen the catalyst reducibility, enhancing the diffusion of ozone into the catalyst structure, and decreasing the average oxidation state of Mn, which enhance the catalytic activity toward ozone decomposition.

Despite the high catalytic activity and stability of MnO_x-based catalysts for ozone decomposition, water vapor has a strong but reversible adverse effect on their performance. Water molecules competition with ozone for adsorption on the active sites of the catalyst leading to blocking the active sites, therefore ozone cannot reach them [17], [30], [32], [39], [40]. To overcome this issue, some modification techniques were applied, such as doping and acid treatment. The purpose of these modifications is to make the active sites more hydrophobic and make the adsorption of ozone stronger than the water molecules.

1.2. Research objective

According to the literature, one of the major challenges that MnO_x-based catalysts are facing for ozone decomposition is the detrimental effect of humidity on their performance. Therefore, this research aims to develop a humidity-resistant MnO_x-based catalyst via a feasible procedure for

efficient ozone decomposition. to achieve this goal the following objectives are planned to carry out:

- Designing a bench-scale test set up that enables tuning the operation conditions, particularly humidity level, ozone concentration and airflow rate.
- Testing several common ozone removal materials to understand their performance followed by studying their physicochemical properties before and after exposure to ozone.
- Using the design of experiment (DoE) approach to statistically investigate the direct effects of operational conditions and their interactions on the performance of ACs and catalysts and determine which parameters are significant.
- Modelling the ozone removal packed bed reactor to study the kinetics of the ozone removal process including convection, diffusion, dispersion, and reaction of ozone through the packed bed.
- Translating the results of statistical and kinetic modeling investigations into the mechanism of water molecules' adverse effect on the materials' ozone removal performance
- Synthesizing a novel MnO_x-based catalyst via a feasible procedure and seeking chemical and physical modifications to improve its humidity-resistance feature.
- Testing and characterizing the synthesized catalysts to study its ozone removal performance at different humidity levels and understand the effect of modifications on the catalysts' properties.

1.3. Thesis organization

Chapter 2 presents a review of recent research on ozone removal technologies. Various types of technologies including activated carbon-based ones, photocatalytic, and catalytic systems, are reviewed and investigated based on their advantages and drawbacks. The recent developments in MnO_x-based catalyst for ozone decomposition are elaborated.

Chapter 3 focuses on systematically comparing the common granular activated carbon and catalysts for ozone removal. A bench-scale test set up was designed to test and study several granular media based on their physicochemical properties before and after exposure to ozone.

Chapter 4 investigates the effect of operational conditions on the performance of granular ozone removal media. The experiments were designed and conducted in a bench-scale test set up.

The results were statistically analyzed and kinetically modelled. The direct effect of operational conditions in addition to the impact of their two-way interactions were demonstrated. Finally, the implications of the findings were presented.

Chapter 5 elaborates on developing a MnO_x-based catalyst for efficient ozone decomposition in harsh environments. Different preparation methods and chemical modifications were investigated. The lab-made catalysts were studied thoroughly utilizing numerous physical and chemical characterization techniques. Also, they were tested in the bench-scale test set up for ozone decomposition. A physicochemical approach was applied to modify the catalyst media and improve its performance at high ozone concentration and high humidity level.

Chapter 6 provides a summary of the thesis and key conclusions in addition to potential ideas for future research.

1.4. Contribution of authors

- Chapter 2:

"Active ozone removal technologies for a safe indoor environment: A comprehensive review;" *Building and Environment*, 187, p. 107370, 2021.

Authors: Marzieh Namdari, Chang-Seo Lee, Fariborz Haghighat

Contribution of authors: MN carried out the investigation and wrote the manuscript. CSL and FH assisted with the data interpretation and supervised the work. All the co-authors reviewed and edited the manuscript.

- Chapter 3:

"A systematic comparative study of granular activated carbons and catalysts for ozone removal;" *Building and Environment*, 224, p. 109510, 2022.

Authors: Marzieh Namdari, Chang-Seo Lee, Fariborz Haghighat

Contribution of authors: MN, CSL, and FH conceptualized the work. MN performed the experiments, analyzed the data, and wrote the manuscript. CSL and FH assisted with data interpretation and supervised the work. All co-authors reviewed and edited the manuscript.

- Chapter 4:

"The effect of operational conditions on the performance of granular ozone removal media: statistical experimental design and kinetic modeling;" Building and Environment, 235, p. 110216, 2023

Authors: Marzieh Namdari, Chang-Seo Lee, Fariborz Haghighat

Contribution of authors: MN, CSL, and FH conceptualized the work. MN designed and performed the experiments, analyzed the data, and wrote the manuscript. CSL and FH assisted with data interpretation and supervised the work. All co-authors reviewed and edited the manuscript.

- Chapter 5:

"Synthesis and physicochemical modification of an MnOx-based catalyst for enhanced ozone decomposition in humid condition;" (under review).

Authors: Marzieh Namdari, Mohammad Khavani, Fariborz Haghighat, Chang-Seo Lee, Mohammad R. K. Mofrad

Contribution of authors: MN, CSL, and FH conceptualized the work. MN developed the catalysts, performed the experiments, analyzed the data, and wrote the manuscript. MN and MK performed the computational parts and analyzed the results. MK, FH, CSL, and MKF assisted with data interpretation and supervised the work. All co-authors reviewed and edited the manuscript.

Chapter 2. Active ozone removal technologies for a safe indoor environment: A comprehensive review

2.1. Abstract

Ozone is a highly reactive gas and one of the critical air pollutants for both indoor and outdoor environments. The Occupational Safety and Health Administration (OSHA) determined that the permissible level of ozone is 100 ppb—for 8-hour exposure at workplaces. Therefore, using ozone removal technology can be crucial when outdoor ozone concentration is high and where active ozone emission sources exist. Activated carbon-based filters, catalytic decomposition, and photocatalytic decomposition are air treatment technologies that have been used for ozone removal. The catalytic decomposition approach showed higher efficiency and higher durability with no generation of considerable by-products, particularly manganese oxide (MnO_x) based catalysts, which can decompose ozone to oxygen at room temperature. The low cost, as well as high catalytic activity, are among the advantages of MnO_x-based catalysts. High specific surface area, high density of oxygen vacancy, high reducibility, and low average oxidation state are desirable properties of the catalyst for ozone decomposition. Despite their excellent performance, their loss of activity in humid conditions challenges their widespread applications. This review presents the recent studies on ozone decomposition technologies, particularly MnO_x-based catalysts performance and modification techniques used to improve their performance, and potential future research directions in this field.

2.2. Introduction

Ozone is one of the most critical inorganic pollutants due to its high reactivity and many adverse health effects [1]. These effects include respiratory irritation (e.g. cough, shortness of breath), chest pain, respiratory inflammation, airway tissue damage, a decrease in lung function, deadening the sense of smell, eye irritation, headache, and exacerbation of respiratory diseases and cardiovascular problems [41]–[46]. Ozone takes part in reactions with organic pollutants present in the indoor environment and generates C1 to C10 saturated aldehydes (e.g. formaldehyde, acetaldehyde), acetone, and organic acids [1], [46]–[50]. Therefore, ozone removal from the indoor environments is crucial to avoid the adverse effects of not only ozone itself but also the wide range of hazardous chemical compounds that form through various reactions involving ozone.

Despite the hazards of ozone exposure, it has various applications in the industry as an oxidizing agent [2]. As it cannot be stored nor transported in containers, it has to be generated *in situ* by

ozone generators. Ozone leakage occurs due to the malfunction of ozone generator components such as piping, gaskets, joint sealers, and valves [5], [6], which puts a large number of workers and occupants at risk of exposure to high levels of ozone. To ensure the safety of workers, regulatory bodies and health organizations set exposure limits[3]–[5] (Table 2.1). An ozone removal technology is required to keep the ozone concentration level below these permissible limits or guideline levels. Additionally, meteorological conditions—high temperature, intense solar radiation, high humidity, low wind speed—and human activities that produce NOx and VOCs favor the ozone formation at ground-level. Natural or mechanical ventilation can introduce ozone to the indoor environment. Using ozone removal technology in the ventilation system is a practical approach to prevent occupants' exposure.

The increasing importance of ozone removal from indoor environments, especially industrial workplaces, has recently motivated a large number of studies on the effectiveness of various removal technologies. This paper reviews the current ozone removal technologies, ozone decomposition mechanisms, and the effect of relative humidity on the performance of each technology.

Table 2.1. Ozone concentration permissible limit determined by health organizations

Organization	Exposure limit
WHO[1] (2005) Indoor environment	0.05 ppm (100 μg/m^3) 8 h exposure
Health Canada Residential buildings	0.02 ppm (40 μg/m^3) 8 h exposure
OSHA Workplace	Permissible exposure limit: 0.1 ppm (200 μg/m^3) workers to not be exposed to an average concentration of more than 0.1 ppm for 8 h per day and 5 days per week
NIOSH[2] Workplace	Recommended exposure limit: <0.1 ppm (200 μg/m^3) / no to be exceeded at any time

[1] World health organization
[2] National institute for occupational safety and health

2.3. Activated carbon-based filters

Activated carbons (AC), cheap and conventional adsorbents, are commonly used commercial ozone removal media [10], [12], [51] in forms of granular activated carbon (GAC) and activated carbon fiber (ACF) [8], [10], [11]. AC-based filters convert ozone to oxygen through an adsorptive decomposition mechanism (Equation 2.1 and 2.2) [8], [9], [52]. Therefore, the adsorption capability affects the removal efficiency.

$$C_n \xrightarrow{O_3} \underset{(-COOH, -COH, -C=O)}{surface\ functional\ groups} + O_2 \xrightarrow{O_3} CO_2, CO + O_2 \qquad chemisorption \quad (2.1)$$

$$2O_3 \xrightarrow{C_n} 3O_2 \qquad catalytic\ decomposition \quad (2.2)$$

Adsorption capacity depends on the specific area and strength of the chemical bonds. Specific surface area increases the performance of AC-based filters by increasing the adsorption sites [8], [10], [12]. Chemisorption—depends on AC's grade that determines its origin and the active sites' density, dispersion, and strength—can also increase the ozone decomposition (Figure 2.1, dark blue GAC-A, GAC-D, and ACF have the same surface area but different efficiency) [10]. Some reports show that the effect of chemisorption is dominant compared with the surface area. For example, the ozone removal efficiency of carbon nanotube supported on quartz fiber (CNT/QF) filter—with much stronger ozone chemisorption on CNT than on AC—was in the same range with the AC filter that its specific surface area was more than 20 times greater than CNT/QF (AC: 913 $m^2.g^{-1}$, CNT/QF: 42.84 $m^2.g^{-1}$) [12]. In another study [11] deposited CNT on ACF filter covered some of the adsorptive micropores of ACF and reduced the filter specific surface area more than 90% (CNT/ACF: 128.06 $m^2.g^{-1}$, ACF: 1583.63 $m^2.g^{-1}$), but the ozone removal efficiency decreased less than 0.5%.

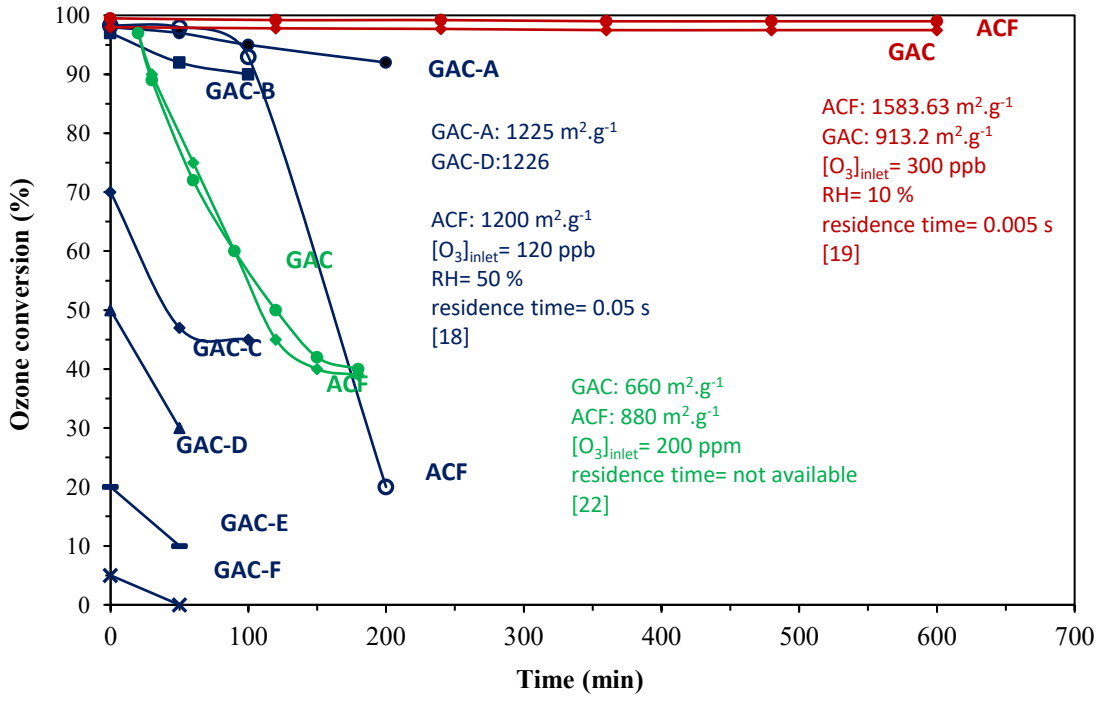

Figure 2.1. AC ozone conversion versus time in four different studies [9], [10], [12]. AC-based filters lose their activity over time. The rate of reduction depends on the AC grade, the ozone concentration, the relative humidity, and the residence time.

Generally, Figure 2.1 shows that AC-based filters have initial high efficiency, but their efficacy declines after a short time; due to carbon consumption by ozone, which produces oxygen, carbon dioxide and carbon monoxide (Equation 2.1) [9], [52]. Multiple studies report composition changes and pore enlargements after AC exposure to ozone [10], [51], [52]. The deactivation rate depends on the AC grade and its intrinsic properties—in Figure 2.1, the deactivation rate of GAC-A and GAC-B (tested under the same condition [10]) is 3% and 7%, respectively in 100 min. Also, the deactivation rate depends on ozone concentration. The experimental data shows lower ozone concentration could consume carbon more slowly.

Relative humidity can have a dual effect on the removal efficiency. It may improve the efficiency because water vapor could decompose ozone (Equation 2.3 to 2.6 [10], [53]), and it may decrease the efficiency because water vapor could cover the surface or block the filter's pores [9], [10], [54]. When RH<20%, it has no considerable effects; for 20%<RH<80%, the chance of positive effect is higher; and in the case of RH>80%, the chance of adverse effect is higher.

$$M + O_3 \leftrightarrow M + O_2 + O \quad (2.3)$$

$$O + H_2O \rightarrow 2OH^{\bullet} \quad (2.4)$$

$$OH^{\bullet} + O_3 \rightarrow HO_2 + O_2 \quad (2.5)$$

$$HO_2 + O_3 \rightarrow OH^{\bullet} + 2O_2 \quad (2.6)$$

where, M—third body—represents the AC surface.

According to the literature and the experimental results, although AC is a cheap and common adsorbent, multiple factors have limited its applications. In addition to its low durability and short-term protection for workers' and occupants' health, ozone reaction with organic compounds (deposited dust and soot on the filters) could produce harmful secondary organic pollutants such as formaldehyde and acetaldehyde [14], [15], [55], [56]. Besides, AC is flammable, and ozone is a strong oxidizer with an exothermic decomposition reaction (ΔH=-143 KJ.mol^{-1}). Thus, it is more appropriate to use AC when the ozone concentration is low—indoor air applications. Therefore, researchers investigated other active technologies such as photocatalytic and catalytic decomposition with more durability.

2.4. Photocatalysts

Photocatalytic decomposition is a technology that removes ozone through a reaction on semiconductor materials such as titanium dioxide (TiO_2). Once semiconductor materials absorb light—usually ultraviolet (UV) radiation with wavelengths less than 400 nm [13], [16], [20]–[23],

[57]–[59]- they generate holes and electrons (Equation 2.7). Subsequent interaction of holes with water forms hydroxyl radicals (Equation 2.11 and 2.12), which can initiate the ozone decomposition process (Equation 2.14). Water molecules are essential to generate hydroxyl radicals (Equation 2.11 and 2.12) that decompose ozone and by-products (Equations 2.11, 2.14 and 2.16). Besides, hydroxyl groups could catch the photoexcited holes and prevent the electron-hole recombination (Equation 2.12) [21], [22], [59], [60]. But, water molecules at elevated levels compete with ozone for adsorption on the photocatalyst's surface and inhibit the ozone reaction with photo-generated electrons, leading to reducing the ozone conversion [20]–[22], [59]. Therefore, an optimum level of humidity should be maintained to maximize ozone decomposition efficiency. The following reactions happen during the photocatalytic decomposition of ozone over TiO_2 [16], [59], [61].

$$TiO_2 \xrightarrow{h\vartheta \geq 3.2ev} h^+ + e^- \quad (2.7)$$

$$e^- + Ti^{4+} \rightarrow Ti^{3+} \quad (2.8)$$

$$O_3 + Ti^{3+} \rightarrow O_3^- + Ti^{4+} \quad (2.9)$$

$$e^- + O_3 \rightarrow O_3^- \quad (2.10)$$

$$O_3^- + H_2O \rightarrow OH^\bullet + OH^- + O_2 \quad (2.11)$$

$$h^+ + OH^- \rightarrow OH^\bullet \quad (2.12)$$

$$O_3^- + O_3 \rightarrow O_4^- + O_2 \quad (2.13)$$

$$OH^\bullet + O_3 \rightarrow O_4^- + H^+ \quad (2.14)$$

$$O_4^- + O_3 \rightarrow 2O_2 + O_3^- \quad (2.15)$$

$$H^+ + O_3^- + O_4^- \rightarrow 3O_2 + OH^- \quad (2.16)$$

The maximum reported efficiency of pure TiO_2 is 59% for P25-TiO_2 (Table 2.2). The low efficiency of TiO_2 attributes to the generated intermediates that cover the surface or occupy the active sites [21], [22]. Adding noble metals (such as Pt[21], Pd[23], [58], and Ag[22]), transition metals (such as Cu, Mn, Fe)[61] (Table 2.2) or using a support[13], [16] could prevent the deactivation and improve the efficiency of the TiO_2.

Table 2.2. Ozone decomposition efficiency of metal-TiO_2 photocatalysts

Ref	Photo-catalyst	Explanation	Source of light	S[a] ($m^2.g^{-1}$)	$[O_3]$[b] (ppm)	WSV[c*] ($L.g^{-1}.min^{-1}$)	T[d] (°C)	RH[e] (%)	η[f]
[21]	Pt-TiO_2	1 % Pt loaded TiO_2 photocatalyst	Three low black light lamps (300-400 nm)	-	1	-	25	0	62%
	TiO_2	Pure P25 TiO_2 photocatalyst		50					59%
[22]	Ag-TiO_2	Ag nanoparticles deposited on TiO_2 photocatalyst	UVA light (0.2 W)	11.7	1000	-	25	70	>95% after 6 h
	TiO_2	Anatase TiO_2 photocatalyst		12.1					<5% after 2 h
[58]	Pd-TiO_2	Pd nanoparticles dispersed in TiO_2 photocatalyst film	low pressure mercury lamp (VUV, 185-254 nm, 58.6 $W.m^{-2}$)	-	21.85	-	25	45	>88%
[61]	P25	Commercial P25 TiO_2 photocatalyst grafted with Cu, Mn, and Fe	UVA-LED-array (365 nm, 10 $W.m^{-2}$)	50	1	1.07	-	50	-
	Cu-P25			-					>35%
	Mn-P25			-					>40%
	Fe-P25			-					>50%

[a] specific surface area
[b] ozone concentration
[c] weight space velocity
[d] temperature
[e] relative humidity
[f] decomposition efficiency
[*] lower wsv means higher residence time

Noble metals and transition metals enhance the photocatalytic activity by facilitating light absorption and electron trapping and preventing the electron-hole recombination [21]–[23], [58], [61]. Noble metals (like Pt, Pd, and Ag) have catalytic activity; they could reduce the deactivation rate over time and ensure a stable ozone conversion in the long-term. For instance, pure anatase-TiO_2 has less than 5% efficiency after 2 h, while the deposition of Ag on its surface increases the photocatalytic decomposition efficiency to more than 95% after 6 h under the same condition.

Among different supports' material include glass pad [13], glass tube [16], nickel foam, aluminum honeycomb, and activated carbon fiber [13]; the highest efficiency attributes to activated carbon support (>95%) due to the high adsorption capacity of AC [13]. TiO_2 supported on the glass pad, aluminum honeycomb, and nickel foam had negligible ozone removal efficiency (less than 10%). But the TiO_2/glass tube was efficient for ozone degradation and kept its activity after repeating the process [16]. Mills et al. [16] proposed that during the ozone decomposition by TiO_2/glass tube, the temperature is increased on the surface of TiO_2—since the reaction is exothermic ΔH=-143 KJ.mol^{-1}—thus, continuous irradiation benefits thermal oxidation and photocatalytic reaction [16].

The overall photocatalysts' ozone removal efficiency is higher and more stable than the AC-based filters, and it improves by adding metals, especially Ag; however, continuous UV irradiation is energy-consuming and is impractical for some applications (e.g. respirator filter). Also, photocatalytic ozone decomposition suffers from inferior efficiency and low durability compared to catalytic decomposition.

2.5. Catalysts

Catalytic decomposition is another major technology for ozone removal. The whole process of catalytic decomposition consists of three main steps: adsorption, reaction, and finally, desorption. Figure 2.2 shows that the dissociative adsorption of ozone on the catalyst's active sites (oxygen vacancies) produces an oxygen molecule and an atomic oxygen (O^{2-}). The activation energy of this reaction is deficient, 6.2 kJ.mol^{-1}; thus, when ozone reaches the catalyst, a layer of atomic oxygen covers its surface. In the next step, the gaseous ozone reacts with the atomic species and generates an oxygen molecule in the gas phase and a peroxide species (O_2^{2-}), which occupies the oxygen vacancy. The last step is desorption of the peroxide species from the oxygen vacancy in the form of a gaseous oxygen molecule. This is the rate-limiting step due to its high activation energy (69.0 kJ.mol^{-1}). If the peroxide does not decompose in time, it will transform into lattice oxygen; thus, the oxygen vacancy cannot be recovered, and the catalyst becomes deactivated [24], [29], [62]–[66]. Desorption of the intermediates (peroxide species) depends on the strength of the chemical/physical bond between the peroxide and the oxygen vacancies—a weak bond means the oxygen vacancy is stable [40]. At the steady state, the peroxide species permanently occupy the weak oxygen vacancies, and only the stable and accessible active sites are left [18]. Therefore, a high density of stable oxygen vacancies results in durable ozone decomposition. However, if the

density of oxygen vacancies increases beyond a certain level (formation of bulk oxygen vacancy), it changes the crystal structure and charges' distribution significantly, which is detrimental for ozone decomposition [30], [31]. Therefore, the density of oxygen vacancies for each catalyst should be optimized. The density of stable oxygen vacancies depends on the intrinsic properties of the catalyst [40]

Various catalytic materials decompose ozone at a near-ambient temperature (Tables 2.3 to 2.7) including metals (platinum (Pt), palladium (Pd), silver (Ag), and copper (Cu)), metal oxides (manganese (Mn), cobalt (Co), copper (Cu), iron (Fe), nickel (Ni), silver (Ag), and aluminum (Al), zeolite and perlite. Besides, transition metal oxides supported on Al_2O_3, SiO_2, TiO_2, and AC were used for catalytic decomposition of ozone [18], [19], [21], [24], [67]–[72]. We review the performance of the common catalysts in the following.

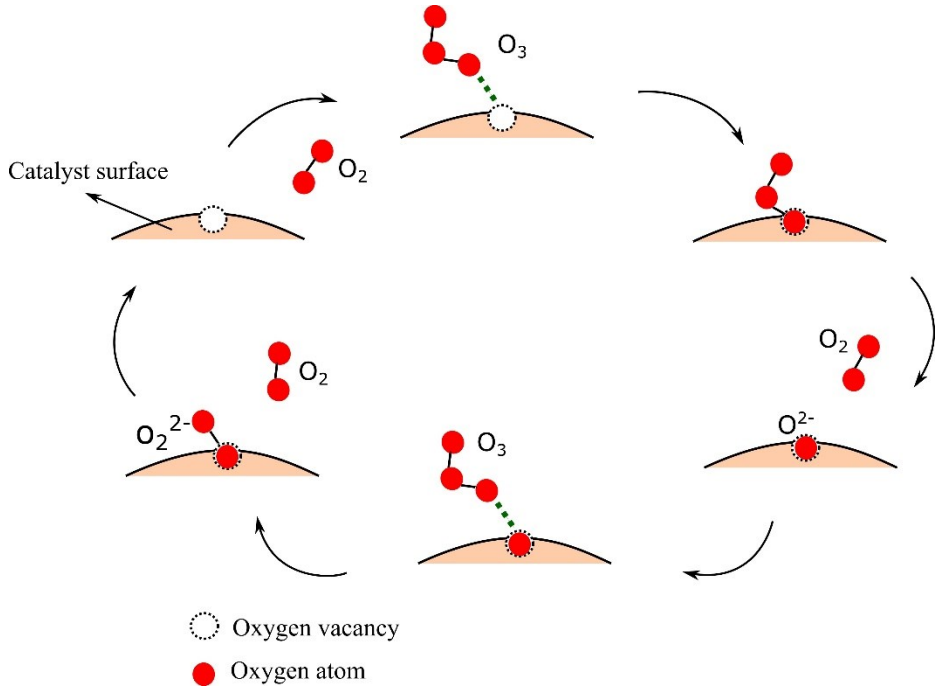

Figure 2.2. Ozone decomposition mechanism in dry air: First, the oxygen vacancy adsorbs ozone and generates an oxygen molecule and a peroxide species; Then another ozone reacts with the peroxide and generates the second oxygen molecule and another peroxide species; Finally, the oxygen vacancy desorbs the peroxide species in the form of an oxygen molecule (the third one). The last step, peroxide species desorption, is the limiting step and causes catalyst deactivation.

- ***Cuprous oxide-based****:* Cu_2O, a typical p-type transition metal oxide, has many applications as a catalyst. Researchers showed that the morphology and particle size of the Cu_2O catalyst substantially affects its ozone decomposition performance [68]–[70]. The cubic particles (<50 nm) are more active, more stable in the long-term, and more resistant to high humidity—100%

efficiency after 8 h at 80% relative humidity (Table 2.3). These particles have {100} plane in their crystal structure that desorb intermediates easier than {111} and {110} planes [68], [70].

Synthesizing the cuprous oxide as a composite, Cu_2O/reduced graphene oxide improves its efficiency more than 3 times—Cu_2O microparticles have 30% efficiency after 2 h under dry condition, while Cu_2O/reduced graphene oxide has 100% efficiency after 72 h under the same condition [69]. The synergistic effect between the Cu_2O and reduced graphene oxide facilitates the electron transfer between them which could improve the electron transfer from O_2^{2-} to the catalyst surface; therefore, it enhances the intermediates desorption, which is beneficial for ozone decomposition.

- ***Iron oxide-based:*** Mesoporous 2-line ferrihydrite (an oxyhydroxide of iron) and mesostructured semi-crystalline iron oxide (a mixture of amorphous ferrihydrite nanoparticles and crystalline γ-Fe_2O_3) showed good performance due to their mesoporous structure that exposes more iron active sites [71], [72] (mesoporous M2LFh and MSIO have 95% and 87% efficiency, respectively; non-mesoporous CIO and 2LFh showed 71% efficiency). Ferrihydrite has a higher amount of iron active sites at or near its surface than in bulk. These iron sites are unsaturated with less oxygen packing around them, making them more available for ozone adsorption [71].

Iron oxide was also investigated in the form of a metal-organic framework (MOF) [72]. MOFs have a high specific surface area, and their active sites are spatially arranged, uniformly distributed, and accessible. The iron (III) based MOF (MIL-100 Fe) with 1726 $m^2.g^{-1}$ surface area showed 100% ozone conversion after 100 h of exposure to 45 ppm ozone. Contrary to the typical decrease in the activity of other catalysts in humid conditions, this catalyst has better performance in the presence of water—100% efficiency at >90% RH. Wang et al. [72] proposed that water could facilitate the formation and decomposition of the intermediates on the surface sites of the MOF. However, MOFs have not been commercialized yet (researchers are investigating the large-scale synthesis and the industrial application of MOFs) [73]. Wang and colleagues [72] fabricated this catalyst as a film as well and placed it in a face mask. The mask could completely decompose a low concentration of ozone (200 ppb) for 12 h [72]. This reveals new use-cases for catalysts to protect workers' and occupants' health when their exposure to ozone is inevitable. This report shows promising results on the use of MOF catalysts for future investigations.

Table 2.3. Catalysts, except the MnO_x-based ones, that are investigated for ozone decomposition

Ref	Catalyst's name	Morphology	S[a] ($m^2.g^{-1}$)	$[O_3]$[b] (ppm)	WSV[c*] ($L.g^{-1}.min^{-1}$)	T[d] (°C)	RH[e] (%)	η[f]
[68]	Cu_2O	Cubic	-	20	1	25	Dry	31% after 2 h
		Truncated octahedral						21% after 2 h
		Octahedral						7% after 2 h
		Cubic 40 nm		770		25	Dry	100% after 6 h
								100% after 66 h
							80	100% after 8 h
				200		0	Dry	100% after 2.5 h
								95 % after 6 h
		Cubic 205 nm				25	Dry	0% after 8 h
		Cubic 447 nm		200				10% after 8 h
		Cubic 968 nm						<5% after 8 h
[69]	Cu_2O	Cubic (~ 2 µm)	5.7	20	1	25	Dry	30% after 2 h
								100% after 72 h
	Cu_2O/rGO	cubic microparticles and ultrafine nanoparticles (~3 nm) on the surface of reduced graphene oxide	5.1				90	>96% after 10 h
[70]	Cu_2O	Nanoparticles (<50 nm)	26.5	3000	4	25	Dry	99.2% after 8 h
							90	>95% after 8 h
	Cu_2O-Al Honeycomb	monolithic	-	10	1	25	Dry	100% after 24 h
							90	
				3000	4		Dry	99.4% after 12 h
[67]	Ni/NiO	Slice structure	7.7	1000	4	25	Dry	100% after 8 h
							90	98% after 8 h
				3000			Dry	80.4% after 8 h
							90	47.8% after 8 h
	NiO	Spherical nanoparticles	-	1000	4	25	Dry	100% after 8 h
							90	54% after 8 h

Table 2.3. *Continued*

Ref	Catalyst's name	Morphology	S[a] ($m^2.g^{-1}$)	$[O_3]$[b] (ppm)	WSV[c*] ($L.g^{-1}.min^{-1}$)	T[d] (°C)	RH[e] (%)	η[f]
[71]	M2LFh	Irregular	180	600	25	25	12	95% initially
	MSIO	Spherical and fibrous	140					87% initially
	CIO	Tubular (non-mesoporous)	82					71% initially
	2LFh	Non-mesoporous	223					71% initially
[72]	MIL-100 (Fe)	Irregular (nanosize)	1726	45	33.33	25	<5	10% after 12 h
							30	90% after 12 h
							45	100% after 100 h
							>90	100% after 12 h
	MOFilter	-	-	0.2			45	100% after 12 h
[74]	CoO_x-350		67.038	1000	2	25	-	88.1% after 4h
[75]	Aluminum reduced anatase-TiO_2	core-shell structured nanoparticles	-	8600	0.1	25	100	95.6% after 12 h
	Anatase-TiO_2	Nanoparticle	102					4.8% after 1 h
[76]	Ag/Al_2O_3	-	0.14	20000	0.1	25	-	>90% after 3 h
	Ag/Cl		-					>80% after 3 h
	Ag/Perlite		-					>70% after 3 h
	Ag/ZSM-5		-					<20% after 3 h
[77]	Ag/SiO_2	-	-	4390	-	23	Dry	90% after 2 h
	Ag/Clinoptilolite		-					85% after 2 h
[78]	Ag/SiO_2	-	342					90% after 6.5 h
	Ag-H-MCM-41		723					94% after 6.5 h
	Ag-Ce-MCM-41		823					65% after 6.5 h
	Ag-H-Beta-11		574					42.5% initially

[a] specific surface area
[b] ozone concentration
[c] weight space velocity
[d] temperature
[e] relative humidity
[f] decomposition efficiency
[*] lower wsv means higher residence time

- ***Silver containing:*** Silver (Ag), a precious noble metal, known as a highly active metal; but the Ag containing catalysts such as Ag/SiO_2 [77], [78], Ag-clinoptilolite [77], Ag/MCM-41, Ag/Beta zeolite [78], [79], $Ag/\alpha\text{-}Al_2O_3$ [76], and Ag/perlite [80] did not show significantly better performance than cuprous oxide, nickel oxide and iron-containing catalysts (Table 2.3). Among these, Ag/MCM-41 has the highest initial ozone decomposition efficiency (98%)[78], [79] –its efficiency declines after 390 min to <95%. The Ag-clinoptilolite shows more durability keeping 85% ozone conversion for 5 days [77]. However, the high price of Ag limits its application compared with transition metal oxide-based catalysts.
- ***Zeolite:*** Natural and commercial zeolites have a porous structure with uniform pores, high internal surface area, ion-exchange ability, selective adsorption, strong and weak Lewis acid sites, and thermal and chemical stability [81]–[83]. They, however, show a low ozone conversion rate compared with other transition metal oxides. For instance, ZSM-5, which is a commercial zeolite, has an ozone conversion efficiency of 40% initially. Although by adding Cu and Fe, its efficiency increased to 70% and 90%, respectively [81]; its efficiencies are still lower than transition metal oxides efficiencies.

In all the above studies, catalysts were investigated separately, under different experimental conditions, which make it difficult to compare their performance. Dhandapani and Oyama [18] tested the ozone decomposition efficiency of several transition metal oxides (supported on $\gamma\text{-}Al_2O_3$ on a cordierite foam) under the same conditions (40 °C, 2 ppm inlet ozone concentration, and 40% RH). They reported that the catalytic activity of the oxides for ozone decomposition was in the order of MnO_2 (42%)> Co_3O_4 (39%)> NiO (35%)> Fe_2O_3 (24%)> Ag_2O (21%)> Cr_2O_3 (18%)> CeO_2 (11%)> MgO (8%)> V_2O_5 (8%)> CuO (5%), which shows the higher activity of p-type transition metal oxides [18]. The p-type transition metal oxides, such as MnO_x, and Fe_2O_3, have more positively charged holes to receive the electrons from the O_2^{2-} than the n-type ones, such as V_2O_5, and Cr_2O_3. Hence, the oxygen desorbs from the catalyst faster and releases the oxygen vacancy easier [18], [19], [67], [84]. Because of their superior performance, the MnO_x-based catalysts have gained more interest than the other transition metal oxide; therefore, they are reviewed in more detail below.

2.5.1. MnO_x-based catalysts

MnO_x-based catalyst has wide applications in ozone decomposition due to its high activity, resulting from its ability to form oxides with different oxidation states, as well as its low price

(compared with noble metals), being environmentally friendly, and good stability [17], [24]–[29], [85]. The presence of multiple oxidation states in the catalyst benefits the ozone decomposition that consists of redox steps (Equation 2.17). If the reduction reaction does not happen, it means that Mn^{n+} is permanently oxidized to Mn^{n+1+} and the catalyst becomes deactivated [17], [24], [29], [62].

$$\begin{cases} O_3 + [Mn^{n+}] \rightarrow O_2 + O^-[Mn^{n+1}] \\ O_3 + O^-[Mn^{n+1}] \rightarrow 2O_2 + [Mn^{n+}] \end{cases} \quad (2.17)$$

Besides, a mixture of high and low Mn valences in the catalyst structure that results in the formation of an oxygen vacancy (Equation 2.18) enhances catalytic activity [24], [40], [86].

$$\begin{cases} 4Mn^{4+} + O^{2-} \rightarrow 4Mn^{4+} + \boxed{2e^-} + {}^1\!/_2\, O_2 \rightarrow 2Mn^{4+} + 2Mn^{3+} + \square + {}^1\!/_2\, O_2 \\ -Mn^{4+} - O^{2-} - Mn^{4+} \rightarrow -Mn^{3+} - \square - Mn^{3+} - + {}^1\!/_2\, O_2 \end{cases} \quad (2.18)$$

where, $\square$ is the oxygen vacancy.

The crystal structure of the catalyst could affect the density of the oxygen vacancy and the reducibility (i.e., the ability to form oxygen vacancies) [87], [88]. The crystal structure can determine the Mn-O bond length affecting the catalytic activity of MnO_x; a weaker bond (longer length) means more active oxygen and thus easier formation of strong oxygen vacancy [30], [86]. The impact of different crystal structures, including α-, β-, γ-, and δ- MnO_x and Todorokite structure (Figure 2.3) were investigated in the literature [24], [25], [29], [32]. Among them, the α type showed better results—α-MnO_2 100%> γ-MnO_2 90%> β-MnO_2 50% [24] (Table 2.4). An example of an α type catalyst with very good performance is octahedral molecular sieve (OMS-2), which belongs to the hollandite group (Figure 2.3), with 92% efficiency after 7 h at 90% relative humidity [89]. Additionally, The presence of impurities in the catalyst's structure leads to the substitution of some of the Mn(IV) cations with Mn(III) or Mn(II) to balance the charge, which results in the formation of oxygen vacancies (Equation 2.17) and decreasing the average oxidation state of Mn [24], [40], [86].

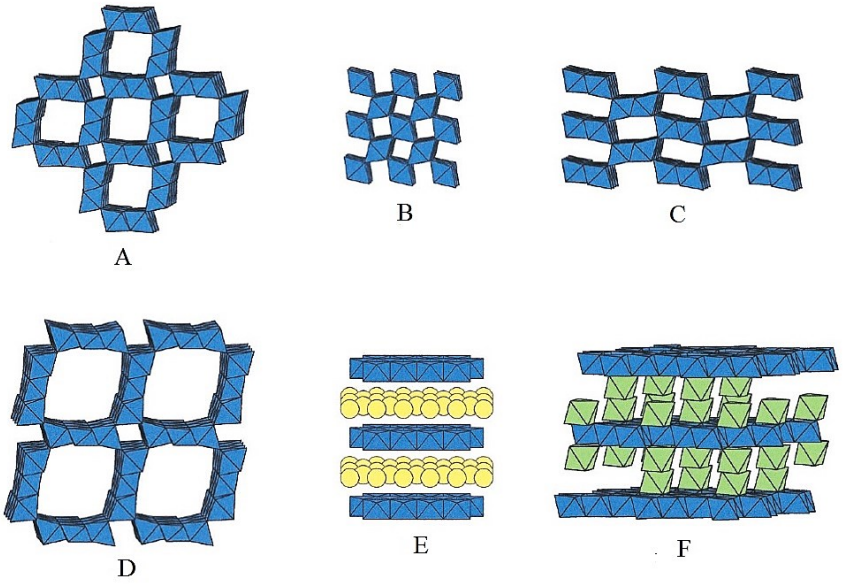

Figure 2.3. Different structures of MnO_x catalyst: (A) α-MnO_x 2*2 tunnels, (B) β-MnO_x 1*1 tunnels, (C) γ-MnO_x 2*1 tunnels, (D) todorokite-MnO_x 3*3 tunnels, (E) δ-MnOx layered structure, (F) λ-MnO_x spinal structure [86]. A, B, C, and D types have a tunnel structure. Each side of the tunnel is constructed of a chain of edge-sharing MnO_6 octahedra. The sides are connected from the corners. In the sides of the octahedral Mn(II), Mn(III), and Mn(IV) are located. Different cations can reside within the tunnels, such as barium and potassium[32], [35], [62].

Moreover, catalyst morphology is also a key factor affecting catalyst efficiency. It can affect the specific surface area, the average Mn oxidation state, the dispersion of the oxygen vacancies, and the exposed crystal facet of the catalyst [28], [90]. The active sites, situated on different crystal facets, have various activities. Therefore, the morphology of the particles and their aspect ratio determine which facet is more exposed [90]–[93]. It is noteworthy that the crystal facets play a crucial role in the formation of oxygen vacancies since each facet has a different energy level [90].

To understand the most effective crystal structure or morphology, one should keep the other properties (e.g., specific surface area) constant and vary the morphology or the crystal structure by controlling the synthesis factors. The critical synthesis factors include the MnO_x precursor, the composition of the reactants, the reaction temperature, the pH of the media, and the reaction duration [25], [37], [88], [91], [94]–[100]. Synthetic methods used are co-precipitation, hydrothermal, solid interface reaction (SIR), sol-gel, emulsion, and chemical vapor deposition. Co-precipitation and hydrothermal methods garnered more attention than the others (Tables 2.4 to 2.7).

Table 2.4. Pure MnOx-based catalysts with different crystal structures and morphologies which were synthesized with different procedures

Ref	Catalyst's name	Morphology	Explanation		S^a ($m^2.g^{-1}$)	$[O_3]^b$ (ppm)	WSV^c ($L.g^{-1}.min^{-1}$)	T^d (°C)	RH^e (%)	η^f
[101], [102]	MnO_2	Bamboo-leaf like rod/sheet	Amorphous MnO_x is synthesized via co-precipitation method using $Mn(Ac)_2$ as the precursor and $KMnO_4$ as the reducing agent calcined at different temperatures	Without calcination	299.7	20	10	25	50	100% after 12 h
							50			<80% after 2 h
									70	<60% after 2 h
[102]	MnO_2-300			Calcined at 300 °C	150.8		10		50	100% after 12 h
	MnO_2-500	Rod-shaped		Calcined at 500 °C	40.6					60% after 12 h
[24]	α-MnO_2	Nanofiber	Synthesized by hydrothermal reaction between $Mn(Ac)_2$ and $KMnO_4$ at 140 °C for 2h		80.7	14	11	25	1	100% after 2 h
	γ-MnO_2		Synthesized via a hydrothermal reaction between $MnSO_4.H_2O$ and $(NH_4)_2S_2O_8$ at 90 °C for 24h		74.6					>90% after 2 h
	β-MnO_2		Synthesized via a hydrothermal reaction between $MnSO_4.H_2O$ and $(NH_4)_2S_2O_8$ at 140 °C for 12h		13.8					>50% after 2 h
[28]	α-MnO_2	Nanofiber	Synthesized by hydrothermal reaction between $Mn(Ac)_2$ and $KMnO_4$ at 140 °C for 2h		80.7	23	14.7	25	45	80% after 2 h
		Nanorods	Synthesized via a hydrothermal reaction between $KMnO_4$ and HCl at 120 °C for 12h		33.8					<60% after 2 h
		Nanotube	Synthesized by hydrothermal reaction between $KMnO_4$ and HCl at 140 °C for 12h		39.2					<50% after 2 h

Table 2.4. *Continued*

Ref	Catalyst's name	Morphology	Explanation	S[a] ($m^2.g^{-1}$)	$[O_3]$[b] (ppm)	WSV[c*] ($L.g^{-1}.min^{-1}$)	T[d] (°C)	RH[e] (%)	η[f]
[30]	α-MnO_2	Nanofiber	Synthesized via a hydrothermal reaction between $MnSO_4.H_2O$ and $KMnO_4$ at 150 °C for 12h. the obtained catalyst was treated by vacuum de-oxidation method to introduce more surface oxygen vacancies	-	20±1	9	25	<5	>95% after 24 h
								90	<40% after 12 h
[91]	α-MnO_2	Sheet	Synthesized by the solid interface reaction between $MnCl_2$ and $KMnO_4$ grounded for 20 min at room temperature	76	60	8.5	-	dry	100% initially
	α-MnO_2	Rod	Synthesized via a hydrothermal reaction between $MnSO_4.H_2O$ and $KMnO_4$ at 160 °C for 24h	59					100% initially
[32]	OMS-2-Ac	Nanofiber	Cryptomelane type MnO_2 (OMS-2)[**] catalyst synthesized via hydrothermal reaction between different Mn^{2+} precursors ($MnAc_2$, $Mn(NO_3)_2$, $MnCl_2$) and $KMnO_4$ at 100 °C for 24h	137	40±2	10	30	90	75% after 6 h
	OMS-2-NO_3			83					>60% after 6 h
	OMS-2-Cl			78					>60% after 6 h
[89]	OMS-2-0.7	Nanorod	Synthesized with $MnAc_2$ as the precursor and $KMnO_4$ as the reducing agent via the hydrothermal method at 100 °C for 24h, the best efficiency obtained with the molar ratio of $KMnO_4/MnAc_2$=0.7	154	500	-	25	Dry	100% after 7 h
								90	92% after 7 h

Table 2.4. *Continued*

Ref	Catalyst's name	Morphology	Explanation	S[a] ($m^2.g^{-1}$)	$[O_3]$[b] (ppm)	WSV[c*] ($L.g^{-1}.min^{-1}$)	T[d] (°C)	RH[e] (%)	η[f]
[74]	MnO_x-350	-	Synthesized via co-precipitation method using $Mn(NO_3)_2$ and NH_4HCO_3 stirred at room temperature for 4 h. The obtained MnO_x catalyst calcined at different temperatures, the best results obtained at 350 °C	116.159	1000	2	25	-	98.5% after 4h
[103]	$MnCO_3$	Spherical	Synthesized via co-precipitation method using $Mn(NO_3)_2$ and NH_4HCO_3 stirred at room temperature for 4 h.	40.5	14	11	25	1	>85% after 24 h

[a] specific surface area
[b] ozone concentration
[c] weight space velocity
[d] temperature
[e] relative humidity
[f] decomposition efficiency
[*] lower wsv means higher residence time
[**] octahedral molecular sieve (OMS-2) belongs to the hollandite group (α-type). OMS-2 MnOx with potassium ions inside the tunnels is named cryptomelane

2.5.1.1. Catalyst modification techniques

After the catalyst synthesis, several modification procedures can be applied to improve the catalytic performance of the MnO_x catalyst. The most important modification techniques are as follows:

2.5.1.1.1. Metal mixing/doping

Doping—a common technique to modify the catalyst properties—would increase the surface oxygen vacancies, the surface acid sites, and decrease the crystallinity. Low crystallinity means more surface defects and a higher specific surface area, improving catalytic activity. Doping can create a mixture of different crystals [17], [25], [40], [87], [93], [104], and alter the morphology of the catalyst particles [25], [40], [93], [104]; changing the morphology is more probable when the dopant has a high valence, such as Mo^{6+} and W^{6+} dopants [105].

The interactions in the interface of two different metal ions and two different crystals can facilitate the formation of more oxygen vacancies. Based on density functional theory (DFT) calculations, the formation energy of the oxygen vacancies is lower in the interface of two different metal ions and two distinct crystal phases [25], [34], [40], [106]. Besides, the metal ions as dopants can substitute the Mn in the framework or the impurities in the crystal structure of the MnO_x catalyst; thus, the average oxidation state (AOS) would change. If the dopant substitutes the Mn^{4+} in the framework, then the AOS of Mn will be reduced, which in turn benefits the ozone decomposition. The physical and chemical properties of the dopant are critical as they determine the type of substitution [35], [106], [107].

Several transition metals, including Fe, Co, Ce, W, and V and noble metals such as Ag, were used as a dopant (Table 2.5). Among these elements, Ce enhanced the catalyst activity further than the other dopants. For instance, in one study, the ozone decomposition efficiency of Ce-γ-MnO_2 was 1.75 times higher than the Co-γ-MnO_2 (at the same experimental condition) [40]. In another study, the ozone conversion of Ce-OMS-2 was 9 times higher than the Co-OMS-2 and Fe-OMS-2 [35]. The improving effects of Ce doping may be caused by the contact boundaries of Mn and Ce that enrich the oxygen vacancies. Besides, Fe^{3+} and Co^{3+} tend to substitute the Mn^{3+} while Ce^{4+} substitutes both the impurities and the Mn^{4+} in the framework, which leads to a higher content of Mn in the catalyst than the other M-MnO_x, a lower AOS and consequently a higher oxygen vacancies formation [35], [106].

2.5.1.1.2. Acid/base treatment

The effects of acid/base treatment on the performance of the MnO_x-based catalysts are presented in Table 2.6. Acid treatment improves the reducibility of the catalyst; therefore, the catalytic activity increases. However, it does not affect the morphology or the crystal structure of the catalyst [29], [37], [108]. Meanwhile, it can increase the surface area by decreasing the size of the particles [108]. Acid treatment could enhance the ozone adsorption, improve the diffusion of ozone into the catalyst pores, increase oxygen vacancies, acid sites, and hydrophobicity of the surface, subsequently increasing the ozone decomposition efficiency [29], [95]. It must be noted that hydrophobic acid sites could be beneficial for stable ozone decomposition under humid conditions (as will be discussed below) [95], [104].

By base treatment, the basic cations would be introduced to the crystal structure of the catalyst, which leads to breaking the charge balance. As mentioned in the previous sections, by breaking the charge balance, more oxygen vacancies form (Equation 2.17), and this is beneficial for ozone decomposition [65].

2.5.1.1.3. Coating/impregnating the catalyst on/into a support

Researchers used in-situ reduction method [26], [38], impregnation method [33], [109]–[111], and chemical vapor deposition method [112] to prepare a supported catalyst. The support affects the morphology, oxidation state of the Mn, and the catalytic activity of the MnO_x catalyst [109], [113]. Different types of support were used, such as AC, CNT, Al_2O_3, and diatomite (DE) (Table 2.7). Among these, the MnO/AC[111] has the highest specific surface area (1156.6 $m^2.g^{-1}$). Coating the MnO_x on CNTs support resulted in increasing the specific surface area, and improving the electron transfer from CNTs to MnO_x, which positively affect the catalytic performance [113]. The loading of the catalyst particles and their dispersion are the parameters that can influence the performance of the catalyst [26], [111]. Besides, for practical applications, using a supported catalyst is more feasible.

Table 2.5. Metal doped MnO_x-based catalysts for ozone decomposition

Ref	Catalyst's name	Morphology	Explanation	S[a] ($m^2.g^{-1}$)	$[O_3]$[b] (ppm)	WSV[c*] ($L.g^{-1}.min^{-1}$)	T[d] (°C)	RH[e] (%)	η[f]
[17]	$MnFe_{0.5}O_x$	Nano sphere	Synthesized via a hydrothermal reaction between $MnSO_4.H_2O$, $Fe(NO_3)_3$ and $KMnO_4$ at 100 °C for 24 h.	262	10000	0.2	25	90	>90% after 8 h
	MnO_x	Nanowire	Molar ratio Fe/Mn= 0.5	71.7					<40% after 30 min
[34]	Fe-MnO_x	Nanoparticle	Synthesized via a hydrothermal reaction between $MnAc_2$, $Fe(NO_3)_3$ and $KMnO_4$ at 140 °C for 2 h.	190	100	22	25	60	73% after 6 h
	α-MnO_2	Nanofiber	Molar ratio Fe/Mn=0.5	92.9					50% after 1 h
[104]	W-MnO_2	Nanoparticle	Synthesized via a hydrothermal reaction between $MnAc_2$, $Na_2WO_4.2H_2O$ and $KMnO_4$ at 100 °C for 12 h.	297	120	11	25	65	>50% after 4 h
	α-MnO_2	Nanorod	Molar ratio W/Mn=0.06	91.3					20% after 4 h
[93]	V-MnO_2	Nanoparticle	Synthesized via a hydrothermal reaction between $MnAc_2$, NH_4VO_3 and $KMnO_4$ at 100 °C for 12 h.	309.8	110	10	25	80	38% after 2.5 h
			Molar ratio V/Mn=0.15						>50% after 5 h
	α-MnO_2	Nanorod		91.3				55	<25% after 5 h
[40]	Ce-γ-MnO_2	Microparticle	Synthesized via a hydrothermal reaction between $MnSO_4.H_2O$, $M(NO_3)_3$ and $(NH_4)_2S_2O_8$ at 90 °C for 24 h followed by calcination at 300 °C for 2 h	120	40±2	14	30	65	96% after 6 h
	Co-γ-MnO_2		M: transition metal (Ce, Co)	87					55 % after 6 h
	γ-MnO_2		Weight ratio M/Mn=0.25	74					38% after 6 h

Table 2.5. *Continued*

Ref	Catalyst's name	Morphology	Explanation		S[a] ($m^2.g^{-1}$)	$[O_3]$ [b] (ppm)	WSV[c*] ($L.g^{-1}.min^{-1}$)	T[d] (°C)	RH[e] (%)	η[f]
[114]	Ce-γ-MnO_2	Globule like microparticles with nanorods on the surface	Synthesized via a hydrothermal reaction between $MnSO_4$, $Ce(NO_3)_3$, and $(NH_4)_2S_2O_8$ at 90 °C for 24 h followed by calcination at 300 °C	The pH of the supernatant was 7	118	40±2	14	30	Dry	100% after 6 h
									65	98% after 6 h
							93.33		Dry	99% after 6 h
										75% after 160h
				The pH of the supernatant was 4	113		14		Dry	100% after 6 h
									65	45% after 6 h
							93.33		Dry	70% after 6 h
[115]	Ce-OMS-2**	Honeycomb and rod	Synthesized via a hydrothermal reaction between $MnAc_2$ and $KMnO_4$ at different temperatures and reaction durations	70 °C, 24 h	364	40±2	10	30	90	57% after 6 h
				95 °C, 24 h	171					90% after 6 h
				120 °C, 24 h	125					11% after 6 h
				95 °C, 2 h	411					61% after 6 h
				95 °C, 14 h	186					93% after 6 h
				95 °C, 36 h	119					74% after 6 h
[35], [116]	Ce-OMS-2	Honeycomb	Synthesized via a hydrothermal reaction between $MnAc_2$, $Ce(NO_3)_3$ and $KMnO_4$ at 100 °C for 24 h, the best result obtained when 80% of the autoclave was filled for the synthesis		216				45	91% after 22 days
[35]	Co-OMS-2	Fiber	Synthesized via a hydrothermal reaction between $MnAc_2$, $M(NO_3)_3$ and $KMnO_4$ at 100 °C for 24 h. The weight ratio of M/Mn=0.125 M: transition metal (Ce, Co, Fe)		200	40±2	10	30	90	90 % after 6 h
	Fe-OMS-2	Microparticle			115					<10 % after 6 h
	OMS-2	Fiber			52					<10 % after 6 h
					137					>70 % after 6 h

Table 2.5. *Continued*

Ref	Catalyst's name	Morphology	Explanation		S^a ($m^2.g^{-1}$)	$[O_3]^b$ (ppm)	WSV^{c*} ($L.g^{-1}.min^{-1}$)	T^d (°C)	RH^e (%)	η^f
[117]	Na-OMS-2	Urchin-like cluster, nanofibers on the surface	Synthesized via SIR method between MnO_2 and $NaNO_3$ using different molar ratios of Na/Mn (The MnO_2 was synthesized via hydrothermal method using $MnSO_4.H_2O$ and $KMnO_4$)	Na/Mn=0	40.73	45±2	11	25±1	30	12.3% after 6 h
									Dry	100% after 6 h
				Na/Mn=1/4	68.58				30	92.5% after 6 h
									60	70% after 6 h
									90	45% after 6 h
				Na/Mn=1.25/4	58.17				30	81.3% after 6 h
[118]	$CeMn_{10}O_x$	Irregular	Cerium-manganese complex oxide catalyst synthesized via a co-precipitation reaction between $MnAc_2$, $Ce(NO_3)_3$ and urea stirring at 90 °C for 12 h. the obtained precipitate is calcined at 600 °C for 3 h molar ratio of Ce/Mn=0.1		75	40	9.33	30	65	99.5% after 6 h
							14			96% after 6 h
[119]	Ce-MnO_x	Microparticles with macropores and mesopores	Hierarchical porous cerium doped MnO_x synthesized via a co-precipitation reaction between dopamine, $Ce(NO_3)_3$ and $KMnO_4$ stirring at room temperature for 1 h		294.4	100	9	25	50	100% after 10 h
							20		50	90% after 2 h
									90	55% after 2 h
						20000	0.2		85	100% after 8 h
[66]	Ce-MnO_2 (300)	Irregular	Calcination the Ce-MnO_2, that is synthesized via the method described in reference 64, at 300 °C for 3 h		103	20000	0.2	25	85	100% after 8 h
[25]	Ce-MnO_2	Sheet	Synthesized in 4 steps: 1. Co-precipitation reaction between $MnCl_2$, $Ce(NO_3)_3$ and $KMnO_4$ at room temperature for 2 days. 2. Ageing the obtained precipitate in the first step for more 2 days in deionized water under continuous stirring which produces Na-birnessite 3. Stirring the Na-birnessite in a 1 M $Mg(CH_3COO)_2$ solution at room temperature for 12 h to ion exchange of Na ions with Mg ions 4. Autoclave the ion-exchanged sample at 125 °C for 2 days to form the tunnel structure		108	50-60				>75% after 3 h
	T-MnO_2	Irregular			26					<30% after 30 min

Table 2.5. *Continued*

Ref	Catalyst's name	Morphology	Explanation	S[a] ($m^2.g^{-1}$)	$[O_3]$ [b] (ppm)	WSV[c*] ($L.g^{-1}.min^{-1}$)	T[d] (°C)	RH[e] (%)	η[f]
[107]	$C_{0.04}(FM)_{0.96}$	-	Cerium modified Mn-Fe mixed oxide catalyst. The molar ratio of Ce/(FM)=0.04	146	21	8	25	Dry	98% after 24 h
								65	63% after 6.5 h
							0	Dry	95% after 7 h
	FM		Mn-Fe mixed oxide catalyst synthesized via a sol-gel method followed by calcination at 400 °C. The ratio of Mn/Fe=2	103			25	Dry	90% after 16 h
								65	55% after 6.5 h
							0	Dry	70% after 7 h
[110]	Co-MnO_x-Al	Microfibrous	Co-MnO_x composite oxide catalyst structured onto Al-fiber felt	24.5	1000± 30	0.8	25	Dry	100% after 12 h
								50	60% after 12 h
								95	30% after 12 h
						1.6		Dry	>80% after 3 h
[120]	Ag-MnO_x	Nanoparticle and nanorod	Synthesized via a co-precipitation reaction between $MnSO_4$, $AgNO_3$ and Na_2CO_3 at room temperature followed by calcination, the best result obtained at 600 °C calcination and 8 wt.% Ag doping	32	40±2	14	30	65	81% after 6 h
	MnO_x	Nanoparticle	Synthesized via a co-precipitation reaction between $MnSO_4$ and Na_2CO_3 at room temperature followed by calcination; the best result obtained at 400 °C calcination	21					70% after 6h

[a] specific surface area
[b] ozone concentration
[c] weight space velocity
[d] temperature
[e] relative humidity
[f] decomposition efficiency
[*] lower wsv means higher residence time
[**] octahedral molecular sieve (OMS-2) belongs to the hollandite group (α-type). OMS-2 MnOx with potassium ions inside the tunnels is named cryptomelane

2.5.1.1.4. Heat treatment

Heat treatment could be an effective way to desorb the water and hydroxyl groups from the surface of the catalyst. Hydroxyl groups are known as a cause of catalyst deactivation because they can react with ozone and produce water, which in turn occupies the oxygen vacancy. Hydroxyl desorption from the surface helps to make the oxygen vacancies more stable. Up to 180 °C, the physically adsorbed H_2O is desorbed, above 180 °C desorption of chemically adsorbed H_2O occurs, and around 300 °C the hydroxyl groups are dehydrated.

More surface oxygen vacancies can be formed by vacuuming the catalyst under high temperatures. At high temperatures, the oxygen escapes from the lattice easier, and the oxygen vacancy is formed at the surface of the catalyst [30].

Heat treatment could also have adverse impacts as it affects the crystal structure and the specific surface area [66], [102]. For instance, it can change the crystal structure from an active phase, like α-MnO_2, to a less active phase, like α-Mn_2O_3. The temperature, thus, should be optimized based on the crystal phase and the oxidation state of the catalyst to obtain desirable results [120].

Table 2.6. Acid/base treated MnO_x-based catalysts for ozone decomposition

Ref	Catalyst's name	Morphology	Explanation		S^a ($m^2.g^{-1}$)	$[O_3]^b$ (ppm)	WSV^{c*} ($L.g^{-1}.min^{-1}$)	T^d (°C)	RH^e (%)	η^f
[95]	H-δ-MnO_2	Micro particles	Birnessite-type MnO_2 (δ-MnO_2) synthesized via a co-precipitation method using $KMnO_4$ and CH_3OH stirred at room temperature for 12 h.	δ-MnO_2 treated by a 0.2 M HNO_3 solution at 50 °C stirred for 6 h	228	115	10	25	50	50% after 24 h
	MnO_2			Pristine δ-MnO_2	40					10% after 30 min
[108]	50-1-N-MnO_2	Irregular nanoparticles	Birnessite-type MnO_2 (δ-MnO_2) synthesized via a co-precipitation method using $KMnO_4$ and C_2H_5OH stirred at 80 °C for 8 h. The obtained catalyst is treated by a 1 M NH_4Cl solution at 50 °C under continuous stirring for 6 h. The N-MnO_2 catalyst is coated on the PET by dip-coating method	-	221	115	10	25	50	80% after 6 h 60% after 60 h
	N-MnO_2/PET	-		The ammonium treated catalyst is coated on polyethylene terephthalate	-	15±1	-			60-80% in 7 days
[65]	K-α-MnO_2	nanowire	Synthesized via a hydrothermal reaction between $MnSO_4.H_2O$ and KMnO4 at 150 °C for 12 h	α-MnO_2 treated by potassium hydroxide in an autoclave at 150 °C	52.43	50±1	9	25	22	100% after 15 h <25% after 25 h
									70	<30% after 10 h
	α-MnO_2			-	61					25% after 12 h

Table 2.6. *Continued*

Ref	Catalyst's name	Morphology	Explanation		S^{a} ($m^2.g^{-1}$)	$[O_3]^{b}$ (ppm)	WSV^{c*} ($L.g^{-1}.min^{-1}$)	T^{d} (°C)	RH^{e} (%)	η^{f}
[29]	H-δ-MnO_2	Nano sphere	Synthesized via a hydrothermal reaction between $MnSO_4.H_2O$ and KMnO4 at 240 °C for 24 h followed by calcination at 300 °C	The catalyst is treated by a 1 M HNO_3 solution at 70 °C for 6 h	206	2000	10	30	Dry	100% after 8 h
	K-δ-MnO_2			Potassium containing δ-MnO_2 catalyst	164					35% after 8 h

[a] specific surface area
[b] ozone concentration
[c] weight space velocity
[d] temperature
[e] relative humidity
[f] decomposition efficiency
[*] lower wsv means higher residence time

Table 2.7. Supported MnOx-based catalysts for ozone decomposition

Ref	Catalyst's name	Morphology	Explanation	S[a] ($m^2.g^{-1}$)	$[O_3]$[b] (ppm)	WSV[c*] ($L.g^{-1}.min^{-1}$)	T[d] (°C)	RH[e] (%)	η[f]
[26]	MnO_x/AC	Curled nanobelt	MnO_x catalyst supported on coal-based granular AC (1.1 % Mn loading) synthesized by *in situ* reductions of $KMnO_4$ with AC	-	21.5-24	3	25	60	>80 % after 24 h
[111]	MnO/AC	Nanoparticle	Synthesized via wet incipient wetness impregnation method using a coal-based AC as the support and $MnAc_2$ as the precursor followed by calcination at 700 °C for 3 h (5 wt% MnO loading)	1156.6	30	20	25	45	85.9% after 10 h
[113]	Mn_3O_4/CNT	MnO_x nanosheets on CNT	Synthesized via an in-situ redox reaction between $KMnO_4$ and CNT. The obtained precipitate: Without calcination: MnO_2/CNT After calcination at 300 °C: Mn_3O_4/CNT	114.1	50	20	25	50	70.4% after 12 h
	MnO_2/CNT	MnO_x nanoparticles on CNT		93.9					60.3% after 12 h
	CNT	Tubular	-	148.6					<40% after 5 h
[36]	Mn/Al_2O_3	-	Synthesized by in situ precipitation of the precursor on γ-Al_2O_3 Precursors: $Mn(OH)_2$, $Cu(OH)_2$, and a mixture of $Mn(OH)_2$ and $Cu(OH)_2$	239	27	-	23	-	35% after 3 h
	Cu/Al_2O_3			299					0 % after 3 h
	$Mn-Cu/Al_2O_3$			273					>95% after 3 h
[39]	$Mn-Pd/Al_2O_3$	-	Synthesized via a sol-gel method, followed by calcination at 500 °C Preparing a sol from AlOOH, then adding Pluronic F127 to the sol, after 1 day adding a mixture of $Mn(NO_3)_2$ and $Pd(NO_3)_2$ to the sol, drying the whole mixture to obtain a gel and then calcining it	292	13	200	40	Dry	90% after 4 h
								10	<80% after 4 h
[87]	$Ni-MnO_x$/DE	Irregular shape	Synthesized via an impregnation method using diatomite as the support, $MnAc_2$ as the precursor and $Ni(NO_3)_2$ as the dopant(5 wt.% nickel doped)	31.25	16	0.33	25	1	80.1% initially
	MnO_x/DE			36.52					<65% initially

Table 2.7. *Continued*

Ref	Catalyst's name	Morphology	Explanation	S[a] ($m^2.g^{-1}$)	$[O_3]$[b] (ppm)	WSV[c*] ($L.g^{-1}.min^{-1}$)	T[d] (°C)	RH[e] (%)	η[f]
[33]	Pd-Mn/SiO_2-Al_2O_3	-	Synthesized via an impregnation method using SiO_2-Al_2O_3 as the support, $MnCO_3$ as the precursor and $Pd(NO_3)_2$ as the dopant followed by calcination at 300-400 °C	97.7	0.6	-	27 32 40	55-65	88.3% initially 100% initially >90% after 80 h

[a] specific surface area
[b] ozone concentration
[c] weight space velocity
[d] temperature
[e] relative humidity
[f] decomposition efficiency
[*] lower wsv means higher residence time

2.5.2. Humidity-a major culprit in reducing the performance

Water vapor has a strong but reversible adverse effect on catalyst performance. Water molecules' competition with ozone for adsorption on the active sites of the catalyst leads to blockage of the active sites, rendering them inaccessible to ozone (Figure 2.4) [17], [30], [32], [33], [35], [39], [40], [75]. The employment of *in situ* Raman spectroscopy [34] and scanning tunnelling microscopy (STM) [95], proved the blockage of oxygen vacancies by water molecules. It shows that the oxygen vacancies are filled with water molecules and the hydroxyl species that are produced through H_2O dissociative adsorption on the oxygen vacancies (Figure 2.4) [30], [34], [95]. The adsorbed water molecules desorb from the surface slowly, and in the long-term, it can cause the catalyst deactivation [30]. Some modification techniques, such as doping and acid treatment, were applied to overcome this issue. The purpose of these modifications is to make the active sites more hydrophobic and make the adsorption of ozone stronger than the water molecules (Figure 2.5 and Tables 2.3 to 2.7). Acid treatment enhanced the efficiency of 400% and increasing the content of Na in the OMS-2 catalyst structure enhanced the efficiency of more than 650%.

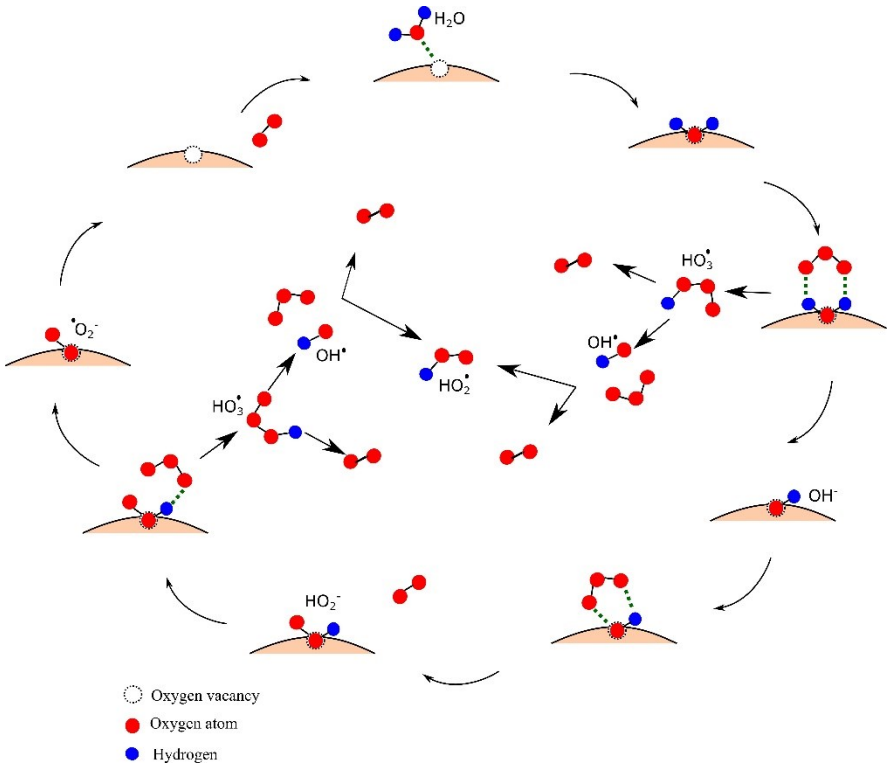

Figure 2.4. The ozone decomposition mechanism in the presence of humidity. Water molecules create an additional ozone decomposition pathway; however, the water molecule hardly desorbs from the oxygen vacancy and at high humidity levels water molecules can occupy all the oxygen vacancies.

2.6. Research prospects

Despite the advancements in the field of ozone removal, there are still areas where further research can be carried out to increase our understanding of the current technologies and find new ways to improve their performance. While past studies focused on the effect of different parameters individually, to the best of our knowledge, there is no conclusive study on the simultaneous effect of inlet ozone concentration, residence time, air flow rate through the reactor, media loading, temperature, and the humidity level on the ozone removal efficiency and the durability of the technology. The lack of such studies makes it difficult to understand the interaction of various environmental factors and learn the relative importance of each in a benchmark system. Specifically, the current data reveal the key effect of humidity on deactivating the catalyst. Novel catalyst synthesis techniques should be explored to circumvent this issue.

Another important subject to explore is the ozone removal performance in the presence of other gaseous pollutants such as VOCs, which reflects the real-life scenario for ozone removal. VOCs can potentially deactivate the catalyst, and their reaction with ozone can form hazardous pollutants; therefore, gaining a mechanistic understanding of ozone-VOC mixture reactions is essential. Another valuable subject of study is designing *in situ* ozone removal technologies such as portable devices or respirators to protect the workers' and occupants' health (e.g., in water treatment plants using ozone). The development of these removal technologies requires improving and testing the catalysts for different use-case conditions. These removal technologies can increase the workers' safety by eliminating the ozone as soon as it is generated, particularly in settings where the implementation of a central HVAC system is not possible.

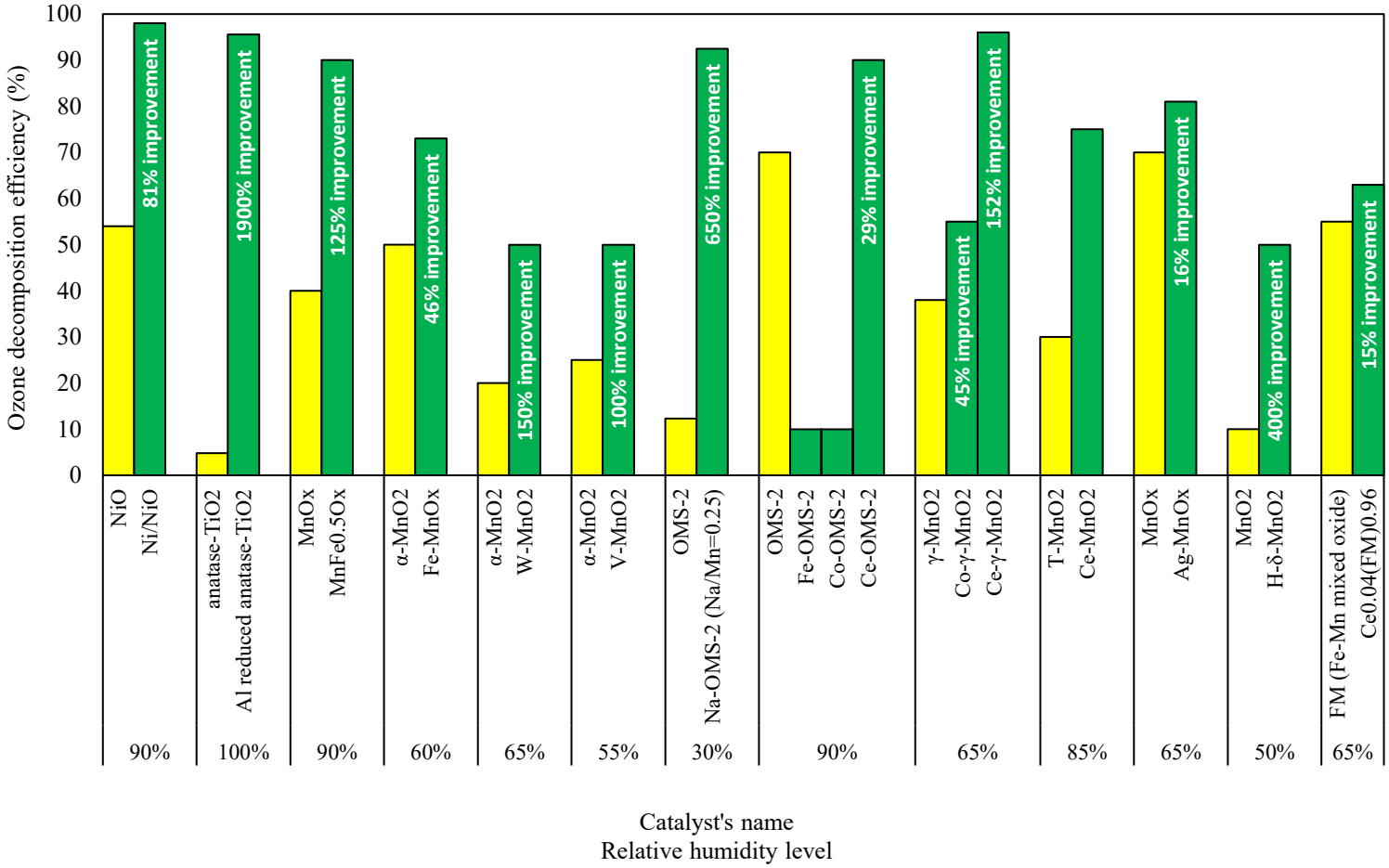

Figure 2.5. Catalyst's performance improves after modification. Yellow columns and green columns show the efficiency before and after the modification, respectively [17], [25], [34], [35], [40], [67], [75], [93], [95], [104], [107], [117], [120].

2.7. Conclusion

Ozone is one of the most critical gaseous pollutants due to its toxicity and wide industrial applications. Many occupants in industrial and non-industrial buildings are at risk of exposure to ozone. Dilution by ventilation may not be sufficient as tropospheric ozone can exceed exposure limits. Therefore, ozone removal by air cleaning is often necessary for exposure control. We reviewed different ozone removal technologies, including AC-based filters, photocatalytic decomposition, and catalytic decomposition.

AC shows low durability because of the saturation and destruction by ozone. Among the photocatalysts, silver doped TiO_2 showed the best results, but its application is limited to where UV-light is present. Catalysts are the most promising. Among different catalysts, Cu_2O and MIL-100 (Fe) (iron (III) base metal-organic framework (MOF)) showed the highest efficiency (100% at 80% RH and 100% efficiency at 90% RH, respectively), but the majority of research focused on MnO_x.

Various parameters can be controlled to increase the efficiency of MnO_2 catalysts. The density of the oxygen vacancy on the surface of the catalyst is the most influential factor that affects its catalytic activity toward ozone. Increasing the specific surface area, increasing the ratio of Mn^{3+}/Mn^{4+}, enhancing the length of the Mn-O bond, improving the reducibility, and decreasing the average oxidation state leads to enhancing the density of surface oxygen vacancy. Lack of durability, particularly under high humidity levels, is the main drawback of MnOx-based catalysts. Future technologies must address this issue. Besides, improving MnOx-based filters may be necessary for industrial applications to protect the workers' health.

Chapter 3. A systematic comparative study of granular activated carbons and catalysts for ozone removal

3.1. Abstract

Ozone is one of the critical air pollutants having direct and indirect adverse health effects. The occupational safety and health administration (OSHA) set 100 ppb as the ozone's permissible exposure limit, highlighting the need for an ozone removal mechanism in many indoor settings. Activated carbon (AC) and metal oxide catalyst-based ozone removal are two widely used technologies for ozone mitigation; however, currently, little insight exists for choosing the best technology based on the application requirements. AC tests were typically limited to low ozone concentration (e.g., ppb level) making it difficult to obtain a broad picture of the link between their performance and properties. Additionally, the ozone removal by ACs and catalysts lacked a complete assessment of performance degradation over time. To fill this gap, this study involves a systematic evaluation of the ozone removal by various granular ACs and granular manganese oxide-cuprous oxide catalysts. The testing methodology was initially based on ASHRAE 145.1 standard; however, test conditions were later made more challenging to better capture the performance decline. It was surprisingly found that, among ACs, the coconut shell-based one have a substantial capacity to remove ozone at moderate and mild concentration levels (<200 ppm), even higher than catalyst, although all ACs get considerably deactivated at high concentration (>99% efficiency at 1 ppm down to <40% efficiency at 900 ppm). By contrast, catalysts feature a slow steady decrease of active sites over time (99% efficiency at 1 ppm down to >70% efficiency at 900 ppm). Subsequent analysis of the material properties demonstrated a strong link between material's type and its physical and chemical characteristics with its ozone removal capacity. The knowledge is envisioned to be of significant utility for numerous applications where ozone contamination is a challenging problem.

3.2. Introduction

Ozone, one of the strongest oxidizers among the chemical compounds, is a hazardous air pollutant due to its direct or indirect adverse health effects. It can directly react with human respiratory tissue causing respiratory irritation, lung damage, and exacerbation of asthma and cardiovascular problems [121]–[124]. Ozone, alternatively, forms secondary organic pollutants through reaction with organic compounds, indirectly producing carcinogens like formaldehyde and acetaldehyde [50], [55], [123], [125]. It also indirectly generates hydroxyl and nitrate radicals

which fuel the production of a variety of toxic free radicals [55], [56], [122]. To mitigate the ozone's harmful effects, OSHA has determined a permissible exposure limit of 100 ppb for workplaces [126], and health organizations suggest keeping the ozone level below a limit—depending on the type of the indoor environment and duration of exposure [127]. Since in many industrial and commercial indoor environments the ozone concentration could be higher than the permissible limits, the use of ozone removal technologies is essential. These technologies are commonly required to eliminate the ozone that may get accidentally released from ozone-handling facilities or are routinely discharged from ozone generators in water treatment units, pulp and paper plants, and hospitals; and, to clean the air intake of aircraft cabins in aviation systems [5], [128]–[134].

Activated carbon (AC) based filtration and catalytic decomposition are two main technologies that have garnered the greatest attention for ozone removal. These technologies function based on different mechanisms. AC primarily relies on the use of chemisorption to convert ozone to benign gases; catalytic decomposition, in contrast, capitalizes on the catalytic conversion of ozone to oxygen. These technologies have unique advantages; they are cheap, readily-available, and rely on easy-to-handle materials [10]–[12], [18]. Motivated by the unique properties of AC and catalysts, a multitude of studies have previously set out to investigate their ozone removal efficacy. A number of works have reported that granular AC and AC fibers, two common industrial form of ACs, can efficiently remove ozone when subjected to a concentration range below 1 ppm [10]–[12]. Other works have identified catalytic media as promising candidates for ozone removal, especially in form of metal oxides [127]. For instance, manganese oxides and cuprous oxides have shown the potential to decompose ozone with >95% efficiency [127]. The outstanding performance of catalysts made them an important research topic with attempts being made at improving traditional catalysts' performance via metal doping, coating, heat treatment, and acid/base treatment [127].

Although earlier works have provided valuable insights into removal mechanisms underlying these two technologies, there is still a lack of comprehensive study that compares various commercially available catalyst and AC media at similar operating conditions. Particularly, not only most past studies differ in the operating testing conditions (airflow rate, temperature, and humidity) but also, they vary widely in terms of tested ozone concentrations, which could significantly impact surface properties and catalytic reactions [127]. ACs for instance were generally studied at low concentrations and there is little information about how they compare

with catalysts at moderate and high ozone levels [10], [135], [136]. By extension, little knowledge is available about how material properties change as a function of operating conditions and how any such alteration may be linked to the medium's performance. Overall, the lack of a comparative broad assessment of ozone removal media have caused significant difficulties in the selection of appropriate technology for each application.

This study was aimed to address the current gaps in literature by systematically investigating the ozone removal performance of representative commercially available materials at identical operating conditions. This assessment involved three widely used AC media including coal-based, impregnated coal-based, and coconut shell-based as well as manganese oxide-cuprous oxide catalyst. ASHRAE 145.1 test method [137], a relevant laboratory technique to examine the performance of loose granular media for ozone removal based on their short-term performance, was used as the basis of initial evaluation even though it was further modified by altering the ozone concentration, airflow rate, and media loading to identify each material's response across wide range of operating conditions. These experiments were complemented with various surface characterization analysis to gain mechanistic insights into catalyst and AC ozone removal behavior.

3.3. Materials and methods

3.3.1. Materials

In total, the ozone removal performance of 11 different granular materials including three different coal-based activated carbon (CL), two different impregnated coal-based activated carbon (IM), three coconut shell-based activated carbon (CS), one palm shell-based activated carbon (PS), one mixture media (activated carbon and permanganate) (MIX), and one catalyst (CAT) with two different sizes were investigated (Table 3.1).

3.3.2. Methods

The bench-scale experimental set-up is portrayed in Figure 3.1. The compressed air was the carrier gas, and a mass flow controller controlled its flow rate (the airflow rate was measured at the outlet of the reactor). A humidifier was used to adjust the humidity at 50%--the humidity was measured at the outlet of the reactor. At 1 ppm and 50 ppm level, ozone was generated by a vacuum UV lamp in a pressure vessel with compressed air as the feed gas. Higher ozone levels (100, 200, 400, 650, and 900 ppm) were produced by an ozone generator (BMT 203, Germany) with oxygen as the feed gas. The ozone decomposition reactor is made of glass and polytetrafluoroethylene

(PTFE). In the reactor, the media holder is a PTFE tube with a specific volume (diameter of 4.8 cm, height of 2.75 cm or 1.38 cm). Inside the PTFE tube the media was sandwiched between two meshes made of perfluoroalkoxy (PFA). The ozone concentration was measured before and after the reactor by an ozone monitor (6-channel Teledyne ozone monitor, 3-channel 2B Technologies 106M). Before testing the media, the ozone concentration before and after the empty reactor was measured, ensuring that the reactor itself did not remove any ozone.

Table 3.1. Materials that are tested in this paper and the operating conditions for each of them

Label	Manufacturer	Type of the media	Experimental conditions			Media weight (g)
			Airflow rate (L/min)	Media volume (mL)	Ozone level (ppm)	
CL-A	A	Coal-based	28.2	50	1, 50, 100, 200	22.16
			14.1	25	200, 400, 650, 900	11.17
CS-A	A	Coconut shell-based	28.2	50	1, 50	23.47
IM-l-A	A	Low KOH impregnated coal based	28.2	50	1, 50, 100, 200	24.29
			14.1	25	200, 400, 650, 900	12.08
IM-A	A	Regular KOH impregnated coal based	28.2	50	1, 50	23.16
CL-B	B	Coal-based	28.2	50	1, 50	24.24
CS-B	B	Coconut shell-based	28.2	50	1, 50, 100, 200	28.05
			14.1	25	200, 400, 650, 900	13.41
MIX-B	B	A mixture of coconut shell-based AC and potassium permanganate	28.2	50	1, 50	41.18
CL-C	C	Coal-based	28.2	50	1, 50	30.82
CS-C	C	Coconut shell-based	28.2	50	1, 50	25.26
			14.1	25	200, 400, 650, 900	12.37
PS-D	D	Palm shell-based	28.2	50	1, 50	25.43
CAT-E	E	A mixture of manganese oxide and cuprous oxide (size: 4.8*2.4 mm)	28.2	50	1, 50	39.29
			14.1	25	200, 400, 650, 900	19.57
CAT-s-E	E	A mixture of manganese oxide and cuprous oxide (size: 2.4*1.4 mm)	28.2	50	1, 50, 100, 200	39.54
			14.1	25	200, 400, 650, 900	19.97

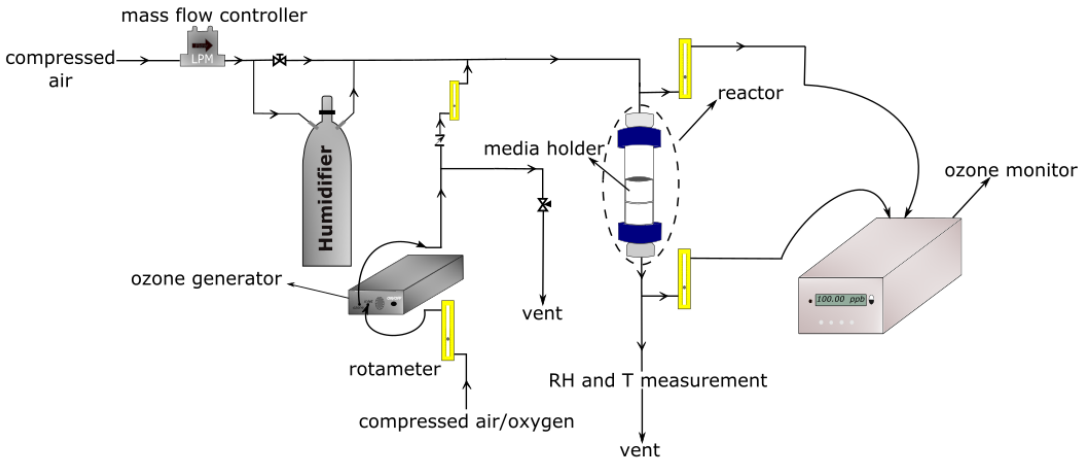

Figure 3.1. The bench scale experimental set-up layout. All the tubes are made of PTFE. The tube size is ¼ inch. The rotameters, valves, and fittings exposed to ozone are made of ozone compatible materials like stainless steel, PTFE, and polyvinylidene fluoride (PVDF).

First, all the media were tested according to the ASHRAE 145.1 standard test method, where the ozone concentration is 1 ppm. Then the ozone concentration was increased to 50 ppm to identify the performance difference between media. After that, CL-A, IM-l-A, CS-B, and CAT-s-E (Table 3.1) were selected as representative material from each media category to test their performance at two elevated concentrations, 100 ppm and 200 ppm. To study the full profile of the media performance, which was necessary for removal mechanism analysis, the ozone concentration was further increased to 400 ppm, 650 ppm, and 900 ppm. However, to ensure safe operation condition the airflow rate and the volume of media had to be decreased by half, while the residence time was kept the same as the ASHRAE standard. At this modified condition CL-A, IM-l-A, CS-B, CS-C, CAT-E, and CAT-s-E were selected as the representative materials—CL-A and CS-B showed the worst and the best performance, respectively, among AC-based media at 50 ppm level; to study the effect of impregnation, IM-l-A was selected to compare its performance with the virgin CL-A; CAT-s-E was selected from the catalyst group; CS-C was selected to compare its efficiency with CS-B; CAT-E was selected to study the effect of catalyst granules' size on the performance. Table 3.1 represents the operating conditions for each material.

The ozone removal performance of the media is reported in terms of conversion (Equation 3.1) and capacity (Equation 3.2).

$$\eta = \frac{C_{inlet} - C_{outlet}}{C_{inlet}} \tag{3.1}$$

$$capacity = \frac{cumulative\ mass\ of\ removed\ ozone}{mass\ of\ the\ media} \tag{3.2}$$

$$cumulative\ mass\ of\ removed\ ozone = \int_0^t \rho\ (C_{inlet} - C_{outlet}) Q\ dt \quad (3.3)$$

where C_{inlet} and C_{outlet} are the ozone concentration before and after the reactor, respectively; ρ is the ozone density determined using the ideal gas law, and Q is the airflow rate.

3.3.3. Characterization

3.3.3.1. Scanning electron microscopy (SEM)

The morphology and porous structure of the samples before and after ozone exposure were observed using SEM (FEI ESEM Quanta 450 FEG, FEI Company, USA) at different magnifications (10000 and 20000). The samples were mounted on a plate using carbon tape, and the SEM images were taken without any coating on the sample.

3.3.3.2. Surface area, pore volume, and pore size distribution

Nitrogen adsorption-desorption isotherms were obtained by the MicroActive TriStar II Plus instrument (Micromeritics Instrument Co.). The specific surface area of the sample was calculated according to the Brunauer-Emmet-Teller theory (S_{BET}) using the adsorption data in a relative pressure (p/p^0) range that gives a linear relationship between the p/p^0 and $1/[Q(p^0/p-1)]$, where Q is the amount of adsorbed nitrogen (mmol/g) [138]. The micropore surface area (S_{mic}), the micropore volume (V_{mic}) and the total volume (V_{tot}) were calculated using the t-plot method, where the thickness of the adsorbed layer was calculated by Harkins and Jura equation [139]. The pore size distribution was determined based on nonlocal density functional theory (NLDFT) using the nitrogen adsorption-desorption isotherm. Before the nitrogen adsorption analysis, samples were dried at 50 ˚C for one week.

3.3.3.3. Surface chemistry

X-ray photoelectron spectroscopy (XPS) was used to analyze the surface chemistry of the samples. The samples were completely dried before running the test, and they were characterized by a K-α instrument (Thermo Scientific) using an Al-kα radiation source (spot size 400 μm). Three points were analyzed for each sample; the survey scan was performed by a 200-eV pass energy with 1 eV step size to study the surface elemental composition. The high-resolution scans were recorded by a 50-eV pass energy with 0.1 eV step size. The high-resolution scans were deconvoluted to their constituent peaks.

The presence of basic groups on the surface was detected by soaking a specific amount of the sample into an acidic solution and measuring the pH. In this method 40 mL of a 0.02 N HCl solution was prepared, 20 mL of this solution was put aside as the blank solution. In the rest 20

mL of the solution, 200 mg of the sample was soaked and mixed using a shaker for 2 days. After the mixture reached equilibrium, the pH of the blank solution and the pH of the mixture were measured and the difference between the blank pH and the mixture pH shows the presence of basic groups—the surface OH^- ions neutralized some of the existing H^+ ions in the acidic solution resulting in an increase in the pH. The increase in the pH can determine the concentration of basic groups in the sample. The concentration of OH^- ions were calculated by subtracting the $[H^+]_{sample}$ from the $[H^+]_{blank}$, where the concentration of H^+ ions were obtained from the pH equation ($[H^+]_{sample} = 10^{-pH}$).

3.4. Results and discussion

3.4.1. Ozone removal performance as a function of concentration

Granular AC and catalyst samples were assessed according to ASHRAE 145.1 test method [137] (Figure 3.2 A). At 1 ppm ozone level, all the materials showed more than 93% efficiency during 6 h exposure to ozone; none of the materials reached the 50% breakthrough—the standard's requirement to end testing. The removal efficiency was in fact so high that the performances of different materials were indistinguishable; for instance, various AC media including KOH impregnated coal-based ones, coconut shell-based ones and the palm shell-based one, all surpassed 99% efficiency. Han et al. [140] also did not achieve the 50% breakthrough for coal based-AC until after 100 h exposure and reported an efficiency of 95% after 80 h ozone exposure for coconut shell-based one and a KOH impregnated coal-based one. Therefore, the ASHRAE 145.1 test method could not fulfil its requirement in a one-day test run.

Based on these preliminary results, testing conditions were modified by increasing the ozone concentration for two reasons: (i) to accelerate the testing; and (ii) to enable differentiating among materials. At 50 ppm ozone and the same airflow rate as previous tests, coal-based-ACs' efficiency started to deteriorate (Figure 3.2 B), yet, none of the materials still reached the 50% breakthrough within 6 hours. At 100 ppm and 200 ppm, CL-A among 4 tested media of CL-A, IM-l-A, CS-B, and CAT-s-E—chosen hereafter as the representative for each media category—was the only material that reached the 50% breakthrough (Figure 3.2 C and D). All the other materials still maintained a high performance (>87% efficiency) revealing the following trend: CS-B>CAT-s-E>IM-l-A. At 100 ppm CS-B had higher efficiency (98%) than the CAT-s-E (96%), but at 200 ppm the gap between their efficiency shrank after 5 h ozone exposure and vanished after 6 h (94% efficiency for both) (Figure 3.2 D).

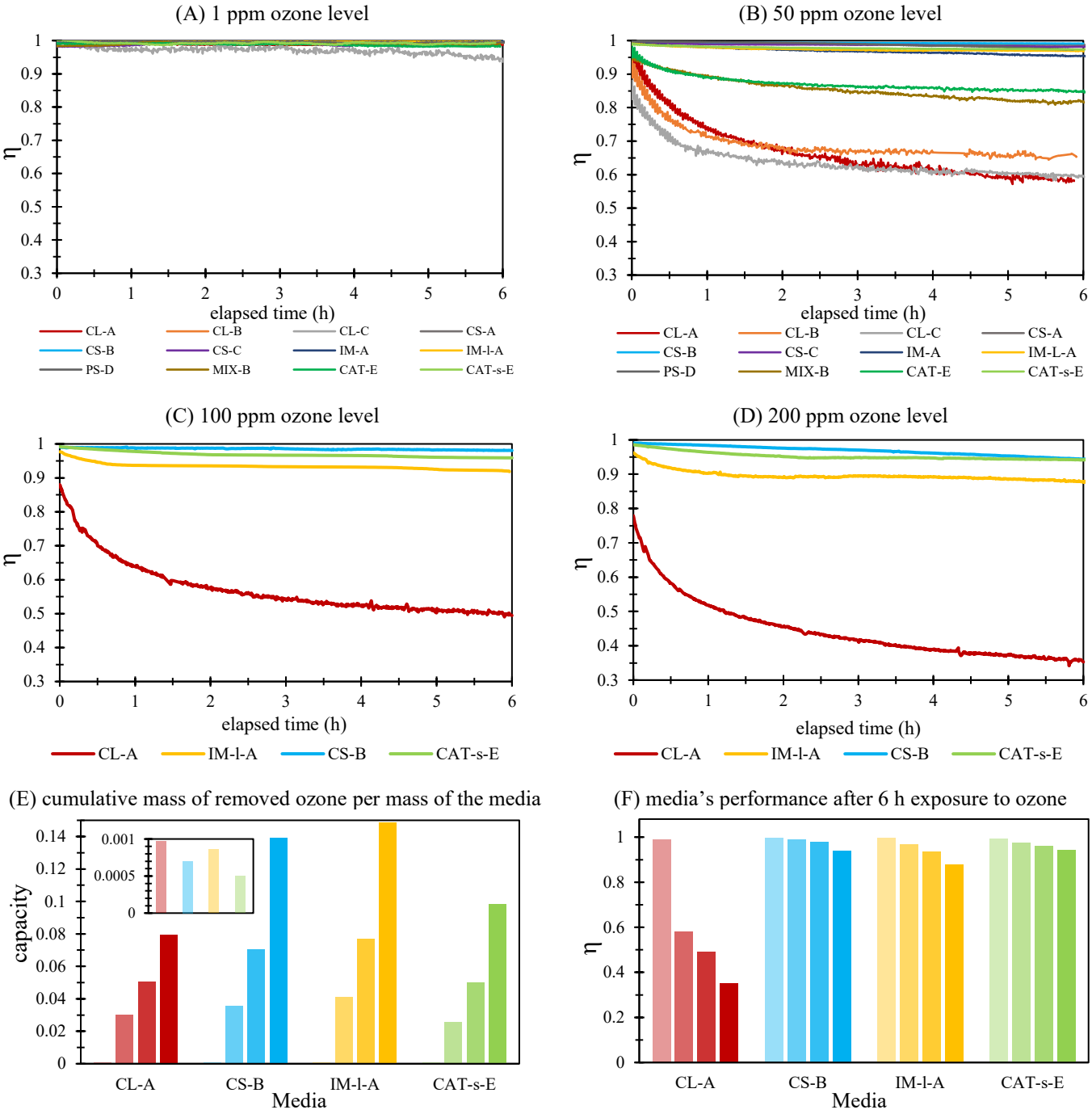

Figure 3.2. The ozone removal performance of 11 different media at ASHRAE 145.1 standard test condition (28.2 L/min airflow rate, 50 mL media, 48.9±2.6% relative humidity, 20.9±0.8 °C temperature). (A) 1 ppm, (B): 50 ppm, (C) 100 ppm, (D) 200 ppm, (E) cumulative mass of removed ozone per mass of the media after 6 h exposure to ozone; the subset shows the capacity at 1 ppm, (F) media's performance after 6 h exposure (in (E) and (F), the ozone level from light to dark shade of color is 1, 50, 100, and 200 ppm respectively). Up to 100 ppm reaching 50% breakthrough in a one-day test run is not feasible, and at 200 ppm, one of the media has reached 50% breakthrough.

* CL: coal, CS: coconut shell, IM: coal impregnated with KOH, PS: palm shell, MIX: coconut shell + potassium permanganate, CAT: catalyst

Figure 3.3 shows the ozone removal performance of six media at 200 ppm, 400 ppm, 650 ppm, and 900 ppm, and the modified test condition (lower airflow rate, lower media loading, and the same residence time—refer to methods). Given the superior performance of the coconut shell-based AC and the catalyst, this figure also illustrates the performance of another coconut shell-based sample from different manufacturer, CS-C, and another catalyst with the same material as CAT-s-E with bigger granule size, CAT-E. It is seen that at higher concentrations the advantage of coconut-shell-based AC over catalyst reversed. At 200 ppm, the CAT-s-E outperformed all the media, and CAT-E, while in the beginning underperformed CS-B and CS-C, regained its advantage after 3.5 hours. At 400 ppm, where the performance of different materials was discernibly segregated, the efficiency of CS-B and CS-C fell further below CAT-E. At 650 and 900 ppm, where CS-B and CS-C became so inefficient that, following an abrupt decrease after 1 hr, they approached the least efficient material, CL-A. Interestingly, at high concentrations (>400 ppm), IM-l-A performed much better than CS-B and CS-C, while, at all concentrations, CAT-s-E showed the highest removal among all the media (compare the performance after 6 hours in Figure 3.3 F).

Calculating the ozone removal capacity after 6 h (Figure 3.2 E and 3.3 E) revealed that up to 650 ppm the capacity was the highest for IM-l-A, but above this level, the CAT-s-E gained advantage. Although CAT-s-E had an outstanding removal efficiency, it also had the highest density among all the tested media detracting from its removal capacity, nevertheless, it removed more ozone per gram than the other materials at concentrated streams (>650 ppm).

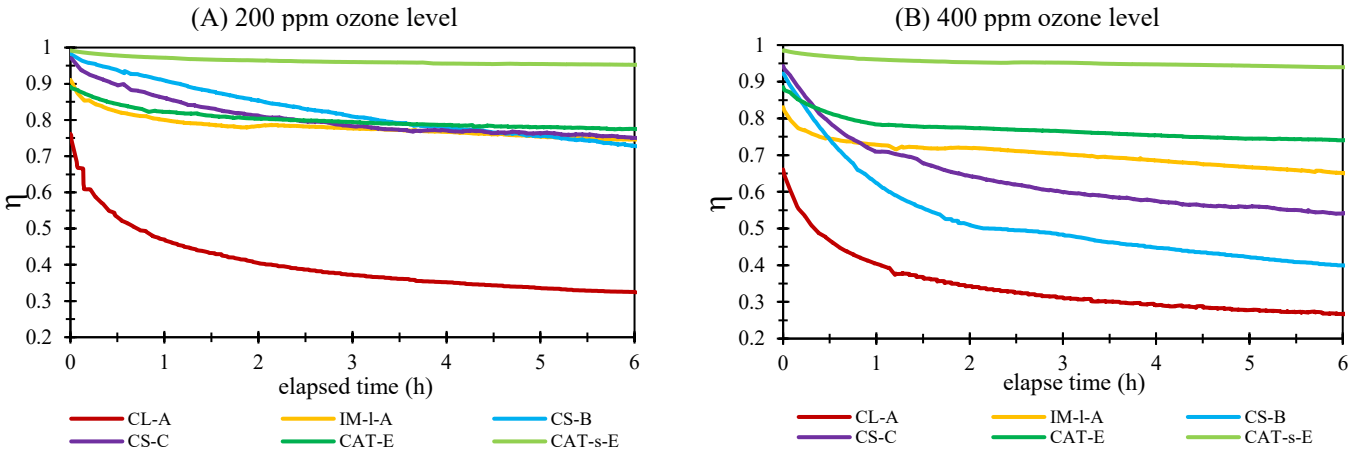

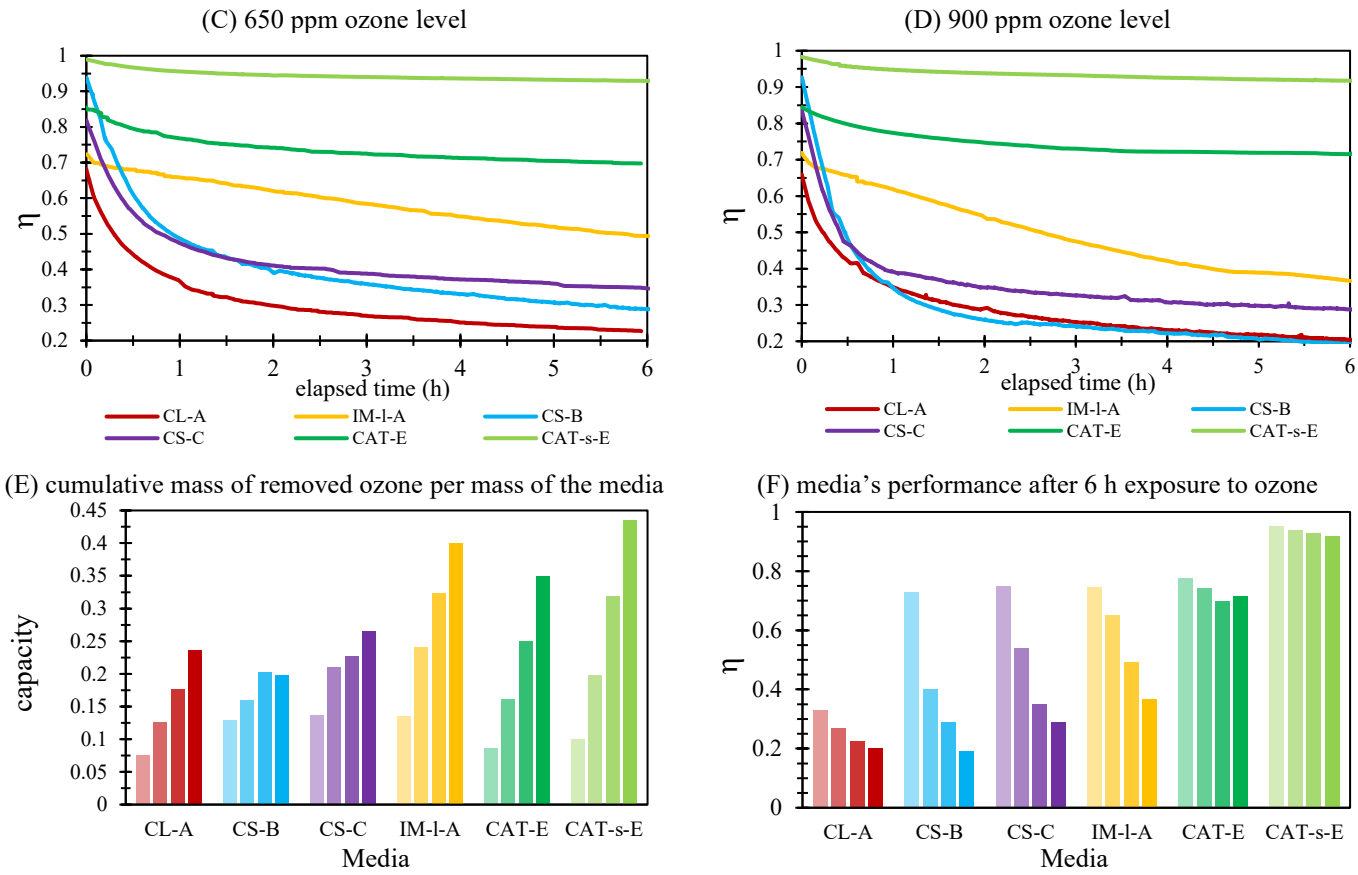

Figure 3.3. The ozone removal performance of five media at 14.1 L/min airflow rate, 25 mL media, 50.3±4.2% relative humidity, and 19.9±1.1 °C temperature—at accelerated ozone levels. (A) 200 ppm, (B) 400 ppm, (C) 650 ppm, (D) 900 ppm, (E) cumulative mass of removed ozone per mass of the media after 6 h exposure to ozone, (F) media's performance after 6 h exposure (in (E) and (F), the ozone level from light to dark shade of each color is 200, 400, 650, and 900 ppm respectively). Up to 400 ppm three media reach 50% breakthrough in a one-day test run, and ≥ 650 ppm all the materials reach 50% breakthrough except the catalyst.

* CL: coal, CS: coconut shell, IM: coal impregnated with KOH, PS: palm shell, CAT: catalyst

3.4.2. The ozone removal mechanism

To be able to interpret the ozone removal behavior of catalysts and AC media, a key starting step is to analyze the mechanism governing these processes. AC-based materials remove ozone through chemisorption and catalytic reaction (Equations 3.4 and 3.5) [9], [10], [51]. Through chemisorption, ozone reacts with the AC and forms oxygen containing functional groups. Further interaction with ozone produces oxygen, carbon monoxide, and carbon dioxide; thus, during chemisorption, ozone consumes carbon while through catalytic decomposition carbon remains unconsumed. Surface area, porous structure, pore volume, and the surface chemistry are the parameters that affect chemisorption. On the other hand, the number of active sites for catalytic reaction determines the catalytic decomposition performance.

$$C_n \xrightarrow{O_3} \underset{(-COOH,-COH,-C=O)}{surface\ functional\ groups} + O_2 \xrightarrow{O_3} CO_2, CO + O_2 \qquad chemisorption \quad (3.4)$$

$$2O_3 \xrightarrow{C_n} 3O_2 \qquad catalytic\ decomposition \quad (3.5)$$

Catalyst, however, removes ozone through its active sites only (Equation 3.6)—which means that ozone does not consume the catalyst. Therefore, the performance of the catalyst strongly depends on the density, dispersion, and durability of its active sites [18], [24], [30], [31], [62], [63].

$$\begin{cases} O_3 + V_O \rightarrow O_2 + O^{2-} \\ O_3 + O^{2-} \rightarrow O_2 + O_2^{2-} \\ O_2^{2-} \rightarrow O_2 + V_O \end{cases} \qquad (3.6)$$

where, V_O is the active site (i.e., oxygen vacancy).

These obvious mechanistic differences in chemistry of the two processes provide a reasonable basis for interpreting the decomposition curves, which feature generic differences between the two categories. A noticeable theme in Figure 3.2 and Figure 3.3 was that the AC-based media had high initial efficiency for all levels of ozone concentration, which lasted longer at low ozone concentrations. At high ozone concentration levels, however, the efficiency fell steeply before reaching a nearly steady efficiency. The catalyst, in contrast, always retained high efficiency across the entire tested concentration range. These observations demonstrated that the high initial efficacy of AC mostly resulted from a dominant chemisorption mechanism (Equation 3.4) while the following drop in the slope was caused by the saturation of the chemisorption sites. Thereat, the AC's limited number of active sites for catalytic reaction substantially restrained the catalytic decomposition rate. Contrary to ACs, catalysts, which are typically manufactured to have high density of active sites for catalytic reaction, always decompose ozone at a relatively faster rate.

Ozone removal rate variation through time (ozone removal rate is defined as cumulative gram of removed ozone per gram of the media per unit of time, s^{-1}) can more clearly illustrate the fundamental difference between ACs and catalysts mechanisms (Table 3.2, Figure S3.1 and S3.2).

For ACs, at low ozone concentration levels, a constant rate of ozone removal was observed, which suggested chemisorption mechanism was dominant (Table 3.2 and Figure S3.2). At high concentrations, a nonlinear decay of removal rate indicated a mechanistic shift (Table 3.2, Figure S3.1 and S3.2)—from chemisorption to catalytic reaction. Catalysts' removal rate, in contrast, remained always constant *versus* time displaying a removal rate proportional to the concentration (Table 3.2, Figure S3.1 and S3.2)—suggesting that the ozone decomposition reaction was first order. This obviously revealed the high density of the catalyst active sites and their durability.

Identifying ozone removal mechanisms facilitates the comparison of individual media. Firstly, the fact that CL-A, CS-B, and CS-C materials at 900 ppm exhibited a comparable final-point efficiency suggested that they consist of nearly equal number of catalytic active sites. It can be then hypothesized that the difference in ozone removal performance of various AC media merely stems from the variation of chemisorption capacity. To verify this hypothesis, the structure of materials was characterized with respect to their morphology, pore volume, specific surface area, and surface chemistry.

Figure 3.4 shows the morphology of the materials before and after exposure to ozone. It shows that coconut shell ACs have a porous structure compared to their coal-based counterparts, which could enhance their chemisorption ability. After reaction with ozone, it was clearly seen that ozone affected coconut shell's morphology more severely than other ACs—evident in increased surface roughness of the CS-B and CS-C compared to the CL-A and IM-l-A (the surface of CL-A and IM-l-A became flaky after exposure to ozone; IM-l-A more than CL-A) (Figure 3.4). In overall, the morphology of the ACs with higher initial efficiency (i.e., higher chemisorption capacity) underwent more significant changes. In contrast, the catalyst samples' morphology remained intact meaning that only the catalytic active sites are involved in ozone decomposition. Table 3.3 further reveals that ozone exposure significantly decreased the specific surface area (S_{BET}) and the pore volume (V_{tot} and V_{mic}) of the CS-B (Table 3.3). These morphological and surface effects together demonstrated a stronger chemisorption reaction between the coconut shell-based materials and ozone.

Table 3.3 also shows that the micropore volume of all the AC materials are decreased after ozone exposure, due to the pore destruction by ozone. The increase in the CL-A total pore volume, in contrast to other AC materials, further confirms its lower chemisorption capacity than other ACs—ozone destructs CL-A's micropores and made them larger resulting in increasing total pore volume and surface area while for the other ACs the pore destruction is more significant such that the total pore volume is decreased. The changes in specific surface area and total pore volume is minor for CAT-s-E sample.

Table 3.2. Calculated ozone removal rate (s^{-1}) in 6 h exposure to ozone for each media (the continuous calculated removal rate versus time is illustrated in Figure S3.2)

		Ozone removal rate (s^{-1})							
		28.2 L/min airflow rate, 50 mL media loading				14.1 L/min airflow rate, 25 mL media loading			
	elapsed time (h)	1 ppm	50 ppm	100 ppm	200 ppm	200 ppm	400 ppm	650 ppm	900 ppm
CL-A	0	0.00016	0.00672	0.01159	0.02363	0.02321	0.04317	0.05777	0.09324
	2	0.00017	0.00523	0.00854	0.01303	0.01267	0.02097	0.02900	0.03988
	4	0.00016	0.00466	0.00767	0.01160	0.01094	0.01794	0.02495	0.03155
	6	0.00016	0.00449	0.00733	0.01082	0.01022	0.01676	0.02221	0.02819
IM-I-A	0	0.00014	0.00664	0.01308	0.02634	0.02625	0.05031	0.06657	0.10011
	2	0.00015	0.00714	0.01287	0.02424	0.02254	0.04072	0.05663	0.07196
	4	0.00014	0.00672	0.01262	0.02462	0.02199	0.03908	0.05054	0.06053
	6	0.00014	0.00667	0.01313	0.02476	0.02163	0.03716	0.04503	0.05132
CS-B	0	0.00012	0.00573	0.01433	0.02466	0.02512	0.04722	0.08145	0.10988
	2	0.00012	0.00581	0.01426	0.02338	0.02273	0.02643	0.03326	0.03009
	4	0.00012	0.00591	0.01423	0.02342	0.01995	0.02313	0.02783	0.02559
	6	0.00012	0.00528	0.01476	0.02263	0.01862	0.02050	0.02426	0.02229
CS-C	0	-	-	-	-	0.02719	0.05149	0.07313	0.10294
	2	-	-	-	-	0.02340	0.03564	0.0371	0.04303
	4	-	-	-	-	0.02135	0.03161	0.03393	0.03838
	6	-	-	-	-	0.02078	0.02999	0.03174	0.03606
CAT-E	0	-	-	-	-	0.01581	0.03062	0.04648	0.06740
	2	-	-	-	-	0.01430	0.02717	0.04246	0.06004
	4	-	-	-	-	0.01391	0.02630	0.04027	0.05853
	6	-	-	-	-	0.01366	0.02602	0.03921	0.05740
CAT-s-E	0	0.00008	0.00392	0.00829	0.01670	0.01796	0.03397	0.05764	0.07828
	2	0.00009	0.00423	0.00842	0.01660	0.01671	0.03315	0.05323	0.07350
	4	0.00009	0.00421	0.00818	0.01598	0.01800	0.03287	0.05281	0.07161
	6	0.00009	0.00424	0.00824	0.01621	0.01648	0.03242	0.05204	0.07171

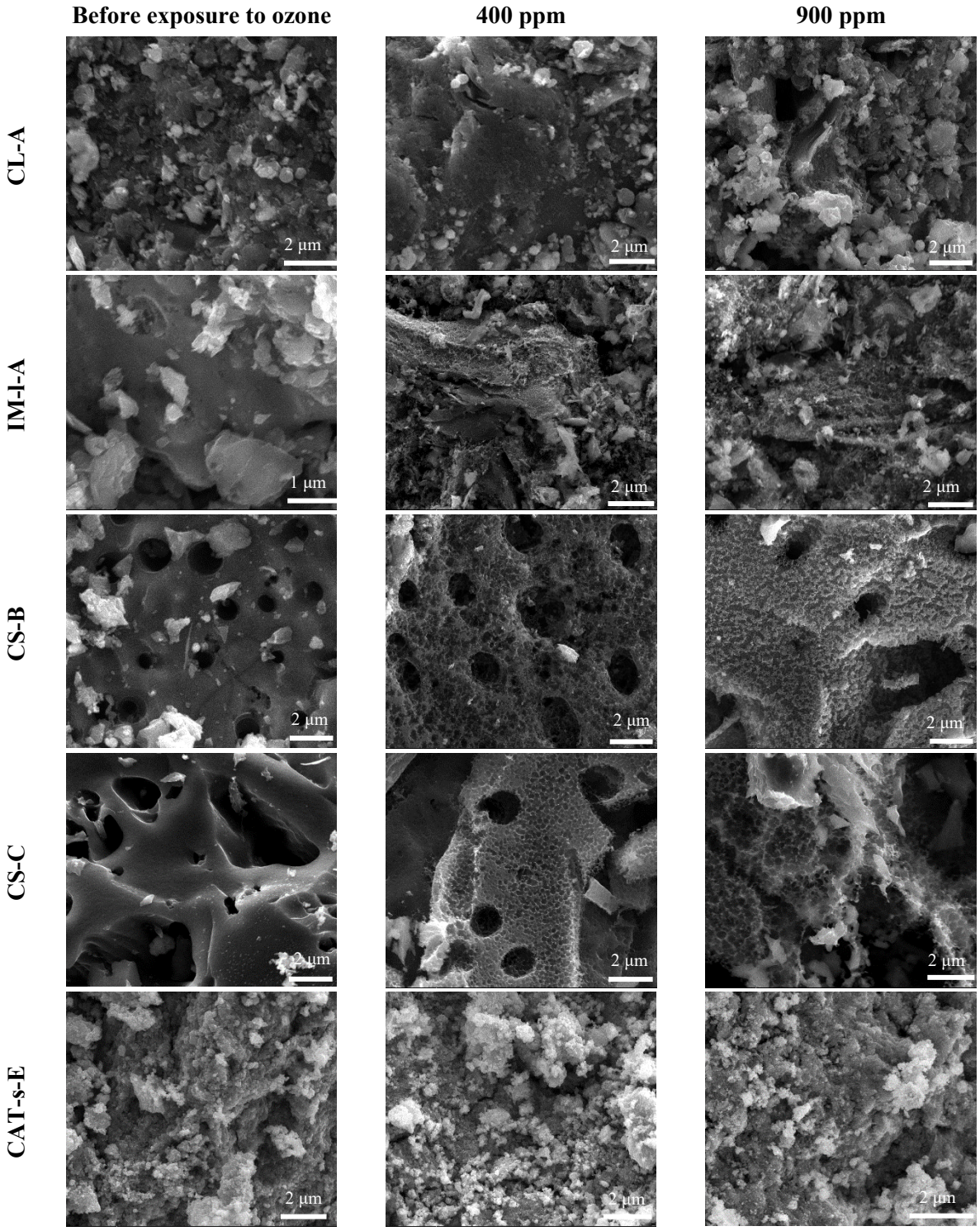

Figure 3.4. FE-SEM images from the materials' surface before and after exposure to ozone with 10000 magnifications. Ozone affected the morphology of activated carbon samples significantly, while it has minor effects on the CAT-s-E.

Table 3.3. The calculated surface area and pore volume of 4 different media before exposure to ozone and after exposure to 900 ppm ozone for 6 h.

	Before exposure to ozone					After exposure to 900 ppm ozone				
	S^1_{BET}	S^2_{mic}	S^3_{ext}	V^4_{tot}	V^5_{mic}	S_{BET}	S_{mic}	S_{ext}	V_{tot}	V_{mic}
CL-A	1114.93	**404.41**	710.52	0.4525	**0.1656**	**1372.10**	264.43	**1107.68**	**0.5599**	0.1153
IM-l-A	**1143.69**	**297.85**	**845.84**	**0.4764**	**0.1200**	1031.25	194.21	837.04	0.4203	0.0839
CS-B	**1001.4**	**807.45**	**193.95**	**0.3980**	**0.3192**	700.18	555.44	144.74	0.2767	0.2192
CAT-s-E	**287.69**	18.47	**269.22**	**0.1232**	0.0060	254.19	**31.33**	222.85	0.1228	**0.0118**

[1] the specific surface area calculated *via* BET method (m^2/g)
[2] the micropores' surface area calculated *via* t-plot method (m^2/g)
[3] the external surface area ($S_{ext}= S_{BET} - S_{mic}$) ($m^2/g$)
[4] total pore volume calculated *via* t-plot method (cm^3/g)
[5] micropore volume calculated *via* t-plot method (cm^3/g)

The surface chemistry of the materials, using the XPS analysis also confirmed the higher chemisorption capacity of coconut shells compared to the other ACs (Figure 3.5 and Figure S3.3 to S3.5). Before exposure to ozone, CS-B had a higher percentage of surface carbon compared to CL-A and IM-l-A— CL-A had silicone on its surface and IM-l-A had both potassium and silicone (Figure 3.5). After exposure to ozone, the amount of oxygen raised on all surfaces due to the emergence of oxygen-containing functional groups (according to Equation 3.4) (Figure 3.5 A to F and Figure S3.3-S3.5). The most dramatic change was recorded on the CS-B sample, consistent with its strongest reactivity with ozone. This intense interaction most likely resulted from a higher initial amount of unsaturated carbon-carbon bonds on the CS-B sample, which reportedly tend to react with ozone to produce carboxylic, lactone, and carbonyl groups (Figure S3.3-S3.5) [141]. The emergence of potassium after ozone exposure on the CS-B surface was another sign of its remarkable ozone reactivity. Given the CS-B initially had potassium in its bulk, the destruction of surface layer by ozone exposed the internal atoms resulting in the detection of potassium in the XPS analysis.

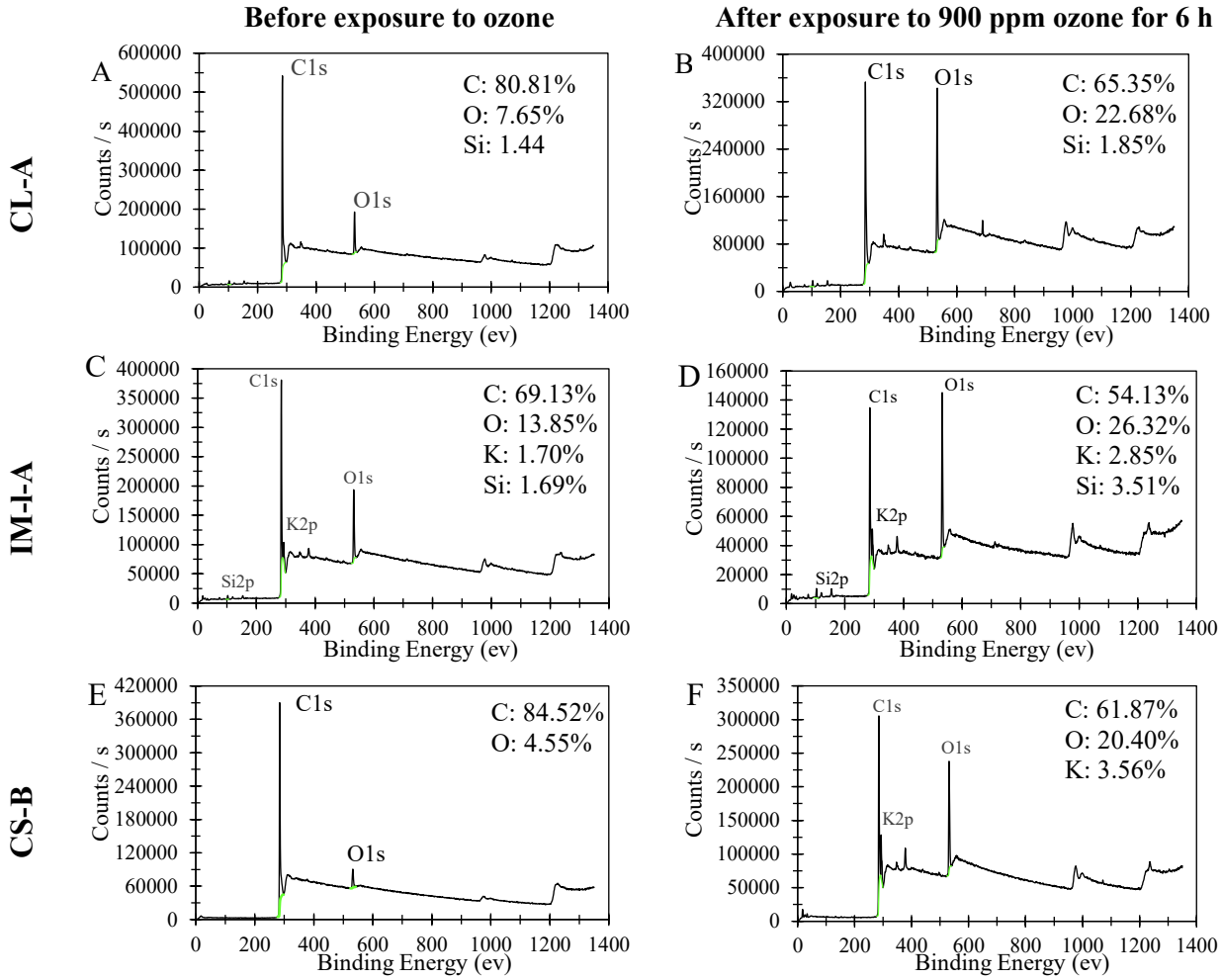

Figure 3.5. The XPS survey of CL-A (A and B), IM-l-A (C and D), and CS-B (E and F), Ozone exposure has a significant effect on the surface composition of AC-based materials.

Interestingly, the impregnated coal-based AC had a higher decomposition rate than the virgin coal-based—at all ozone levels. This can be well explained by analyzing the IM-l-A's ozone removal pathways. Previous studies showed that, impregnating the AC with *KOH* increases its pore volume, enhancing the chemisorption [142]. Meanwhile, *KOH* changes the surface chemistry by providing OH^- groups on the surface [143], [144], which could contribute to ozone decomposition reaction according to Equation 3.7 [144]–[146]. Here the involvement of OH^- in the reaction was verified by measuring the number of basic groups on the AC surface. Table 3.4 shows that the number of basic groups decreased after ozone exposure, demonstrating the considerable reactivity between ozone and the basic groups. Therefore, it can be inferred that the basic groups at longer exposure time were likely to act as the active site for the catalytic ozone decomposition enhancing IM-l-A efficiency over other AC-based materials at high ozone

concentration levels (>400 ppm). This notion also corroborated with the observation that CS-C, which have higher amount of OH^- groups compared to CS-B (Table 3.4), showed higher efficiency than CS-B when ozone was greater than 200 ppm (Figure 3.3).

$$OH^- + O_3 \rightarrow HO_2^- + O_2 \quad (3.7)$$

Table 3.4. The concentration of basic groups on the surface of the materials. Blank sample was a 0.02 N HCl solution. The H^+ ion concentration for each sample is calculated using pH equation. The OH^- concentration is calculated using: $[OH^-]_{sample} = [H^+]_{blank} - [H^+]_{sample}$.

Sample	pH	H^+ ion concentration	OH^- ion concentration
Blank	2.14	0.007244	-
CL-A	2.72	0.001905	0.005339
CL-A exposed to O_3	2.39	0.004074	0.003171
IM-l-A	2.83	0.001479	0.005765
IM-l-A exposed to O_3	2.78	0.001660	0.005585
CS-B	2.36	0.004365	0.002879
CS-B exposed to O_3	2.28	0.005248	0.001996
CS-C	2.41	0.003890	0.003354
CS-C exposed to O_3	2.32	0.004786	0.002458
CAT-s-E	4	0.000100	0.007144
CAT-s-E exposed to O_3	3.66	0.000219	0.007026

Unlike ACs, the XPS analysis of the catalyst showed that the surface atomic composition was unaffected by ozone (shown for CAT-s-E in Figure 3.6 A and B, and Figure S3.6). This was consistent with the catalytic decomposition mechanism, which necessitates no change in chemical composition. The behavior of metal oxide catalysts is instead determined by the density and durability of active sites, which is reflected in the average oxidation state (AOS) of the metal [18]. According to the XPS results, the AOS of Mn slightly increased from 3.303 to 3.740 (Figure 3.6 C and D), clearly showing that the active sites were highly conserved for both catalysts (i.e., oxygen vacancies).

Given that the chemical composition of CAT-E and CAT-s-E are identical, the difference in their performance must be purely physical. A notable physical distinction between the catalysts was their granule size difference. The improved performance of CAT-s-E, which had smaller granule size, therefore, most likely arose from its ability to be better packed (with 25 mL media loading, the bed porosity of the CAT-E and CAT-s-E was 4.5% and 2.6%, respectively), causing more even airflow distribution and a more effective collision between the air stream and the catalyst particles.

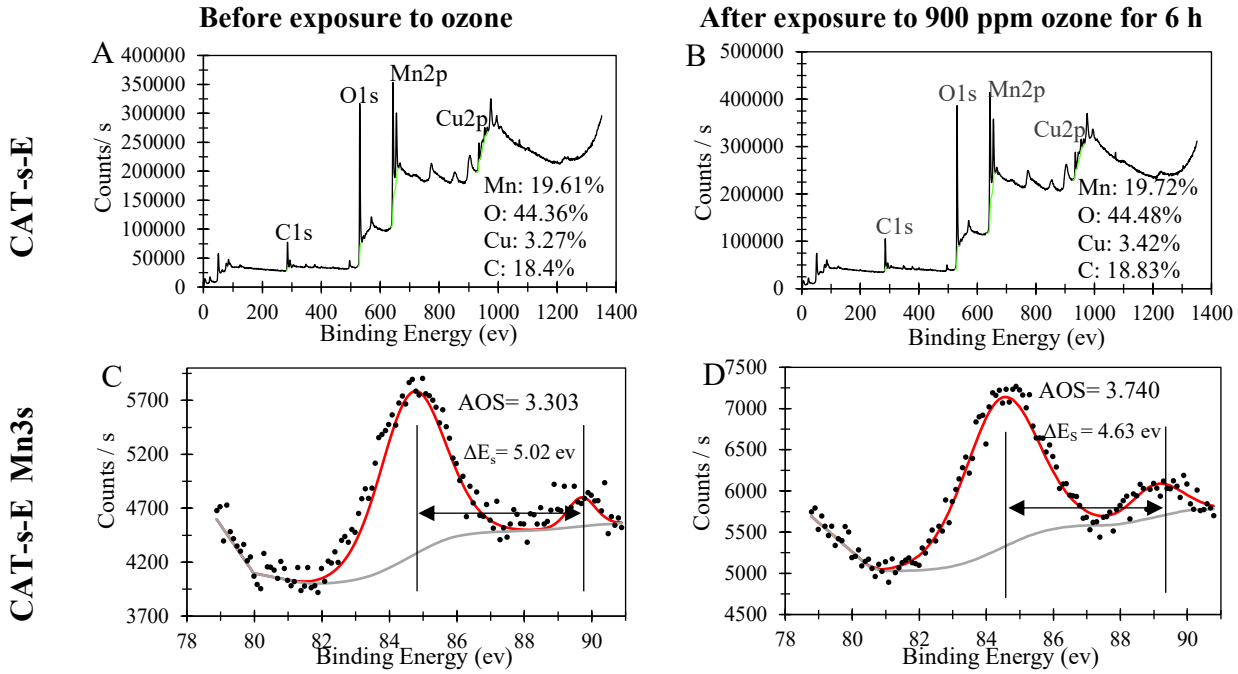

Figure 3.6. The XPS survey of CAT-s-E (A and B) and the high-resolution scan of Mn3s of CAT-s-E (C and D). Ozone exposure has a minor effect on the CATs.

An unexpected behavior concerning these two catalysts occurred upon increasing the concentration from 650 ppm to 900 ppm. After 45 min the efficiency of CAT-E at 900 ppm surpassed its efficiency at 650 ppm, which stood in contrast to the CAT-s-E behavior, and the rest of the materials at these concentrations (Figure 3.2 and Figure 3.3). This effect can also be explained in terms of the physical structure of the catalysts upon ozone exposure. The pore volume and external surface area of the CAT-E exposed to 900 ppm ozone was higher than the one that was exposed to 650 ppm (Table S3.1). Ozone decreased the surface area, and the total pore volume, while it increased the micropore volume (Tables 3.3 and S3.1). When the ozone increased from 650 ppm to 900 ppm, the micropore volume of the CAT-E was maintained and the total pore volume was increased along with the external surface area (Table S3.1). This showed that further exposure of CAT-E to higher levels of ozone changed the morphology leading to increment of pore volume and external surface area, which marginally improved the removal efficiency.

3.4.3. Comparison of the results with previous works

The mechanistic assessment of various granular AC-based and catalyst media provides new insights into catalytic and chemisorption-based ozone decomposition. Previously it has been shown that AC-based media can remove ozone efficiently through chemisorption mechanism when the concentration is at ppb level [9], [11], [12]. The current results demonstrated that such

mechanism can robustly decompose ozone up to 200 ppm establishing that AC was superior to catalysts across a wide range of concentration. These results are unique given that catalysts were conventionally believed to be more efficient at such high concentrations. However, a key point worth noting is that in the earlier studies, the ozone removal media were mostly tested in form of a filter not granules [10]–[12]. For instance, Lee and Davidson [10] tested various types of AC-based commercial filters for removal of 120 ppb ozone (the efficiencies were varied from 98% to less than 2%). The filters contained adhesives, woven fabrics, and other materials. In this study, AC materials were all in granular form which enabled us to resolve the ACs' performance in terms of their inherent properties. Accordingly, it is deduced that exploiting AC's excellent chemisorption capacity is only possible when it is used in granular form.

The importance of surface chemistry is further evident when comparing the performance of various media. Since the chemisorption relies on surface properties, it has been argued that the surface area is among the most critical parameters [8], [10]. Here, it was proved otherwise; the surface area of CL-A was 1.11 times higher than CS-B, nonetheless it showed poorer performances. It can thus be reasoned that commercial media perhaps benefitted from high density of chemisorption sites; the ineffective surface chemistry was instead responsible for the material's low reactivity toward ozone. It is cautiously highlighted that the current work did not provide a systematic assessment of the relative significance of physical and chemical factors, these preliminary results suggest that surface chemistry along with surface area must be systematically studied and optimized to achieve higher removal yields.

The removal assessments also bring into attention salient points regarding catalytic ozone removal. The catalysts were mostly studied in the powder form in the earlier works [127]. Here it was demonstrated that a commercial granular catalyst can have high efficiency. However, the granular size effect is still an important parameter to be investigated. A granular catalyst in two sizes was studied. Both catalysts showed a durable performance—the small size one had higher efficiency—and its performance was slightly affected by increasing the concentration. Future studies are required to investigate the effect of operational parameters, other than the ozone concentration, on the granular catalyst performance.

Lastly, all these results point to the possibility of predicting the media service life based on the lab-scale experimental results. ASHRAE 145.1 standard test method assumes that the results at high ozone level in short term predict the performance at lower ozone level in long term [137]:

Han et al [147] have confirmed this assumption. Therefore, according to the results at 400 ppm ozone level, where the materials' performances were clearly distinguishable, one can deduce that the high efficiency of catalyst media outlasts AC-based media. Furthermore, among the AC samples, the service life has the following order: coal AC impregnated with KOH> coconut shell AC> coal AC.

3.4.4. Practical implications of findings

The current study's results, obtained from a systematic assessment of various commercially available AC and catalytic media, hint to important consideration regarding the application of each medium. These results can serve as a preliminary guideline for selecting the type of granular media in ozone removal systems. AC-based media are popular for gaseous pollutants removal and cleaning the air. However, some organizations like CNESST (standard, equity, occupational health, and safety commission) does not suggest AC as an ozone removal media [148]. In many studies, accordingly, ozone removal tests have been restricted to low ozone concentrations. Based on current results, AC-based media efficiently remove low levels of ozone—below 1 ppm all the tested ACs removed ozone with >99% efficiency, and below 50 ppm impregnated coal-based AC and coconut shell-based AC removed ozone with >96% efficiency. Therefore, AC-based media are good candidates for indoor air applications like residential buildings, and office buildings. If, the media can be exposed to high ozone concentrations intermittently or for removal of high levels of ozone (<50 ppm) in short-term, coconut-shell based AC are highly desirable (like for the buildings placed near high traffics or in the down-stream of a wildfire). For the applications that the media is routinely exposed to high levels of ozone or when a reliable performance is desired, such as air crafts or the exhaust of industrial ozone generators, catalyst media are most likely the best choice, since they have a high and stable efficiency unaffected by the ozone concentration. Moreover, the ozone removal mechanism analysis that is discussed in this study could help to find the best combination of materials for the air treatment systems that can efficiently remove not only ozone but also other types of air pollutants.

3.5. Conclusion

Various kinds of granular AC (coal-based, coal-based impregnated with KOH, and coconut shell-based), common materials in air cleaning devices, and a granular catalyst, the most common material for ozone removal, were investigated in this study. The performance of the chosen materials was compared to one another by testing them under different operational conditions. The

results confirmed that the ASHRAE 145.1 standard test method cannot fulfil its requirements in a one-day test run since none of the materials could reach the 50% breakthrough; therefore, the experimental condition had to be modified. The coconut shell-based activated carbon (CS-B) showed the best performance at ozone levels below 200 ppm during 6 h exposure to ozone. However, the small size catalyst (CAT-s-E) had superior performance than the others when the ozone concentration was >200 ppm. Furthermore, KOH impregnated coal-based AC had an improved ozone removal performance by more than 60% compared to the virgin coal-based one.

The materials were analyzed before and after exposure to ozone by multiple characterization techniques including specific surface area measurement, SEM imaging, and XPS analysis. These techniques provided sufficient information to compare the materials based on their removal mechanism. AC-based materials remove ozone through chemisorption and catalytic reaction; here it is confirmed that the chemisorption capacity of ACs is much higher than their catalytic capability. During chemisorption, oxygen-containing functional groups form on the surface of the AC and oxygen, carbon dioxide, and carbon monoxide are produced (ozone consumes the carbon). The coconut shell-AC has a high chemisorption capacity, resulting in its high removal performance below 200 ppm ozone. SEM images and XPS results show the strong interaction between ozone and the CS-B material confirming its high chemisorption capacity. Above 200 ppm ozone, the AC materials efficiency decreased significantly, but the small size catalyst (CAT-s-E) showed more than 92% efficiency. The catalyst is designed to have a high density of stable active sites, and the XPS results showed a minor increase in the AOS of the catalyst, which means only a small portion of active sites were deactivated after 6 h exposure to 900 ppm ozone.

Based on the findings in this study, the high chemisorption capacity of AC-based media makes them good candidates for indoor air applications in residential buildings and office buildings. If the ozone concentration can rise above 1 ppm (<50 ppm) for a short-term, coconut shell-based ACs are the best choice among the AC-based media. When the ozone concentration is constantly high, like in the intake air pathway of aircraft cabins or the exhaust of ozone generation systems, catalyst-based media with a high density of stable active sites are desirable.

3.6. Supporting Information

Table S 3.1. The calculated surface area and pore volume of CAT-E material after exposure to 650 ppm and 900 ppm ozone for 6 h.

	After exposure to 650 ppm ozone					After exposure to 900 ppm ozone				
	S_{BET}^{1}	S_{mic}^{2}	S_{ext}^{3}	V_{tot}^{4}	V_{mic}^{5}	S_{BET}	S_{mic}	S_{ext}	V_{tot}	V_{mic}
CAT-E	199.911	25.3298	174.581	0.08605	0.00998	219.969	25.3939	194.575	0.09467	0.00993

[1] the specific surface area calculated *via* BET method (m^2/g)
[2] the micropores' surface area calculated *via* t-plot method (m^2/g)
[3] the external surface area ($S_{ext}= S_{BET} - S_{mic}$) ($m^2/g$)
[4] total pore volume calculated *via* t-plot method (cm^3/g)
[5] micropore volume calculated *via* t-plot method (cm^3/g)

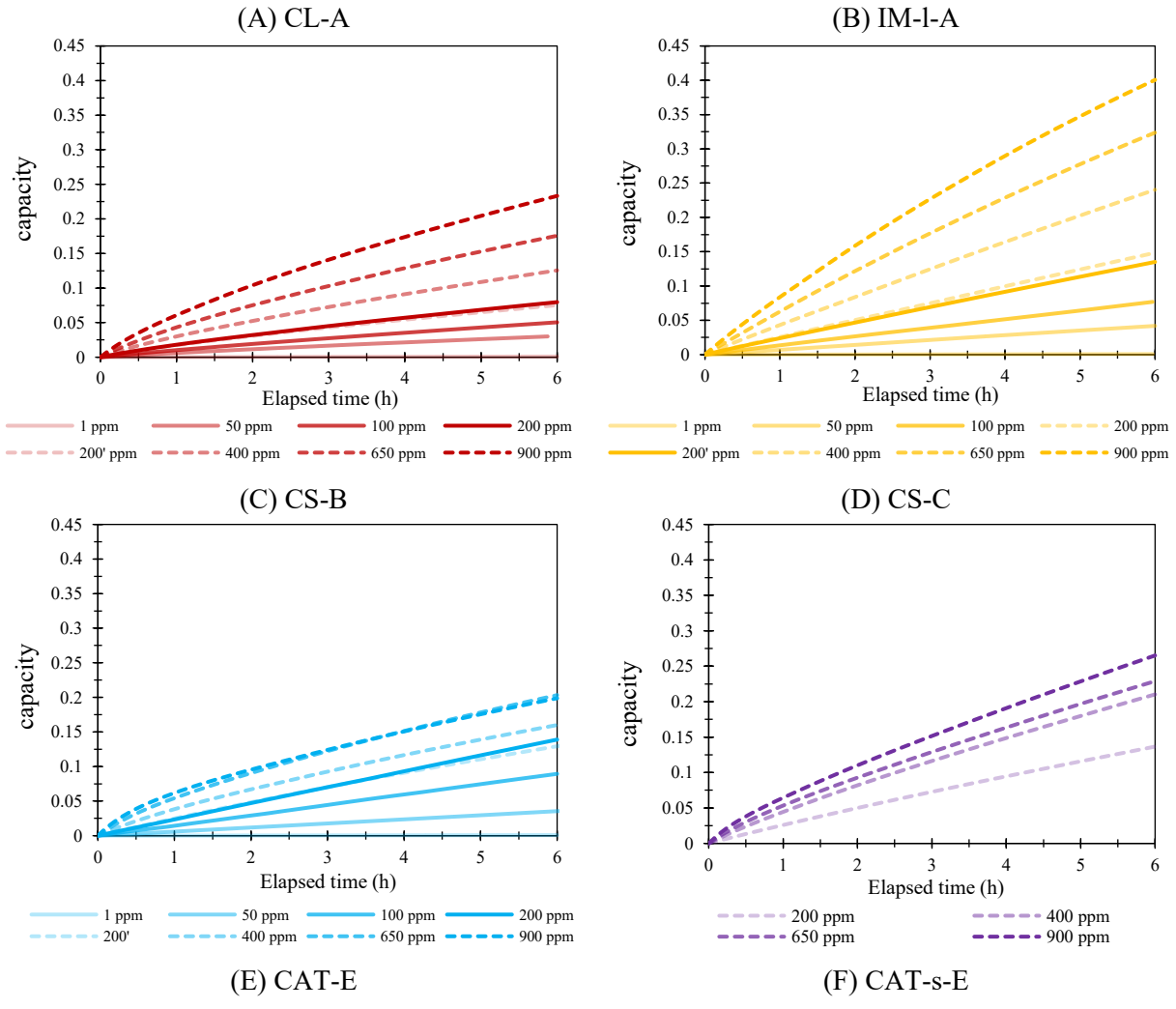

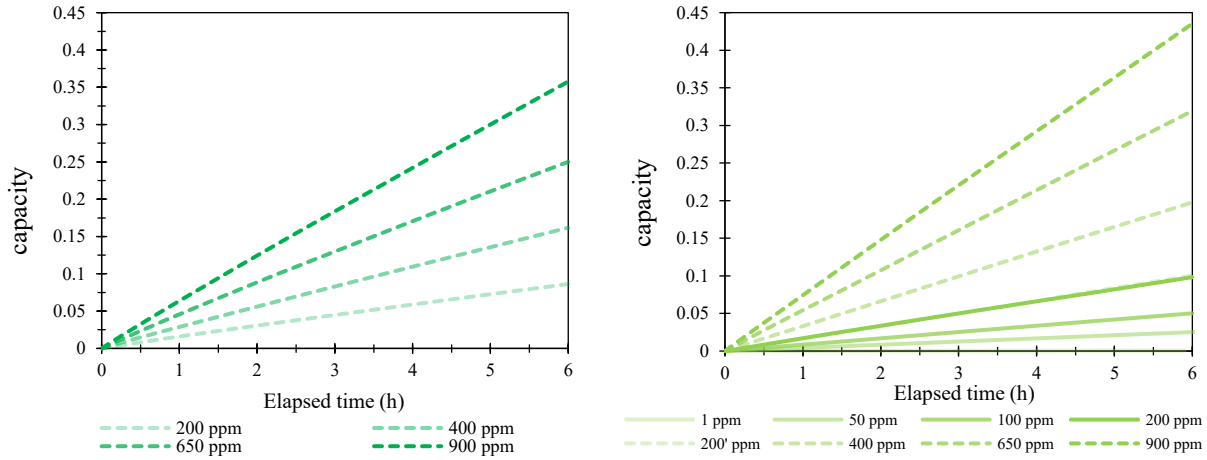

Figure S 3.1. The ratio of cumulative mass of removed ozone to the total mass of the media during 6 h exposure to ozone. At low concentration, the ratio increases with a constant rate; however, by increasing the ozone concentration, the rate of increase is altering; it decreases over time. (solid lines: airflow rate= 28.2 L/min, media loading= 50 mL; dashed lines: airflow rate= 14.1 L/min, media loading= 25 mL).

(A) CL-A

(B) IM-l-A

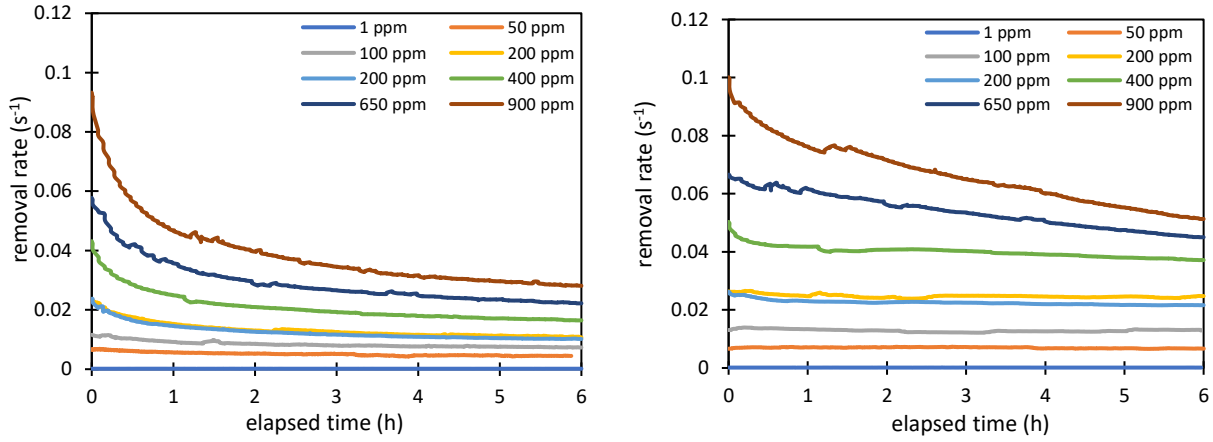

(C) CS-B

(D) CS-C

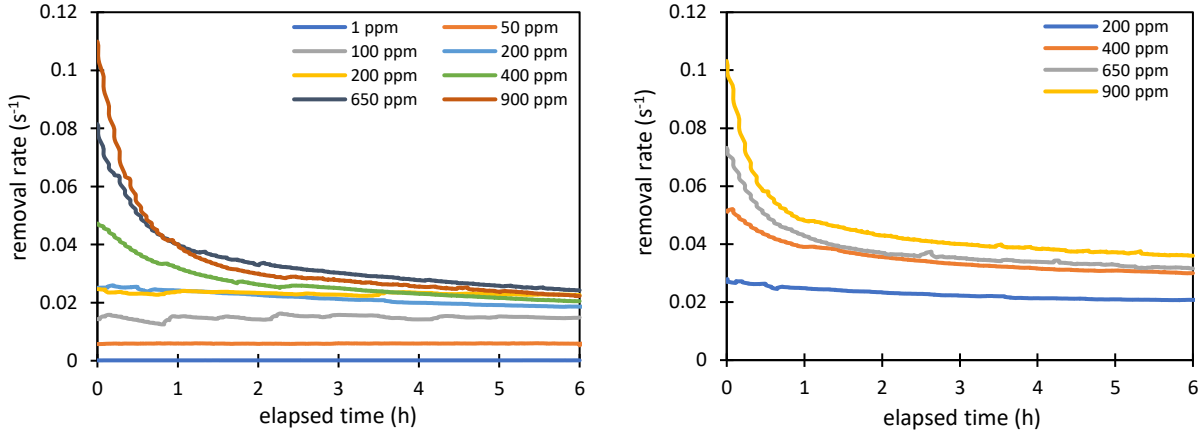

(E) CAT-E

(F) CAT-s-E

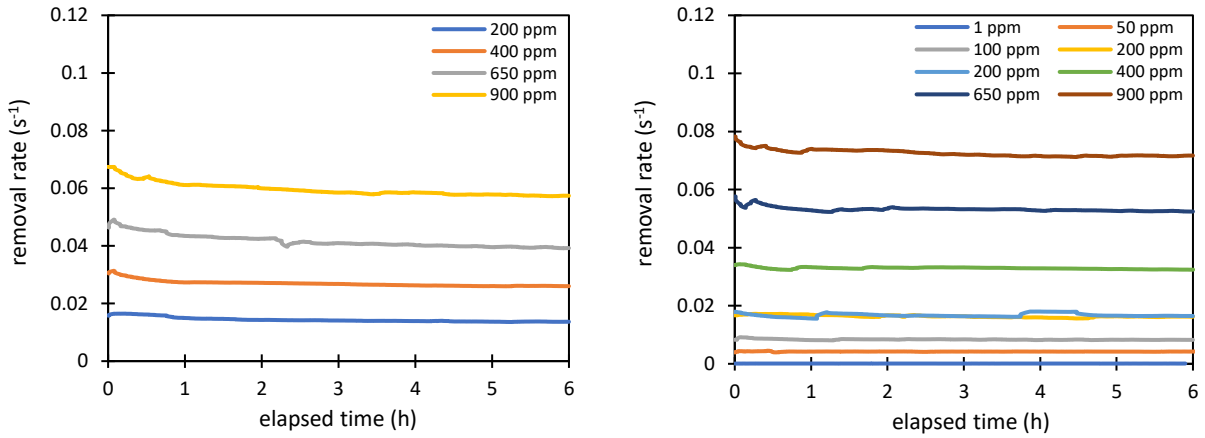

Figure S 3.2. The ozone removal rate (s^{-1}) of the media during 6 h exposure to ozone. The profile is different for AC-based media and the catalyst media. Regarding AC-based media at low concentrations the removal rate is constant and by increasing the concentration an abrupt non-linear decay is observed which indicates shifting the removal mechanism. Regarding the catalyst media, the removal rate is almost constant, and it is proportional to the concentration level.

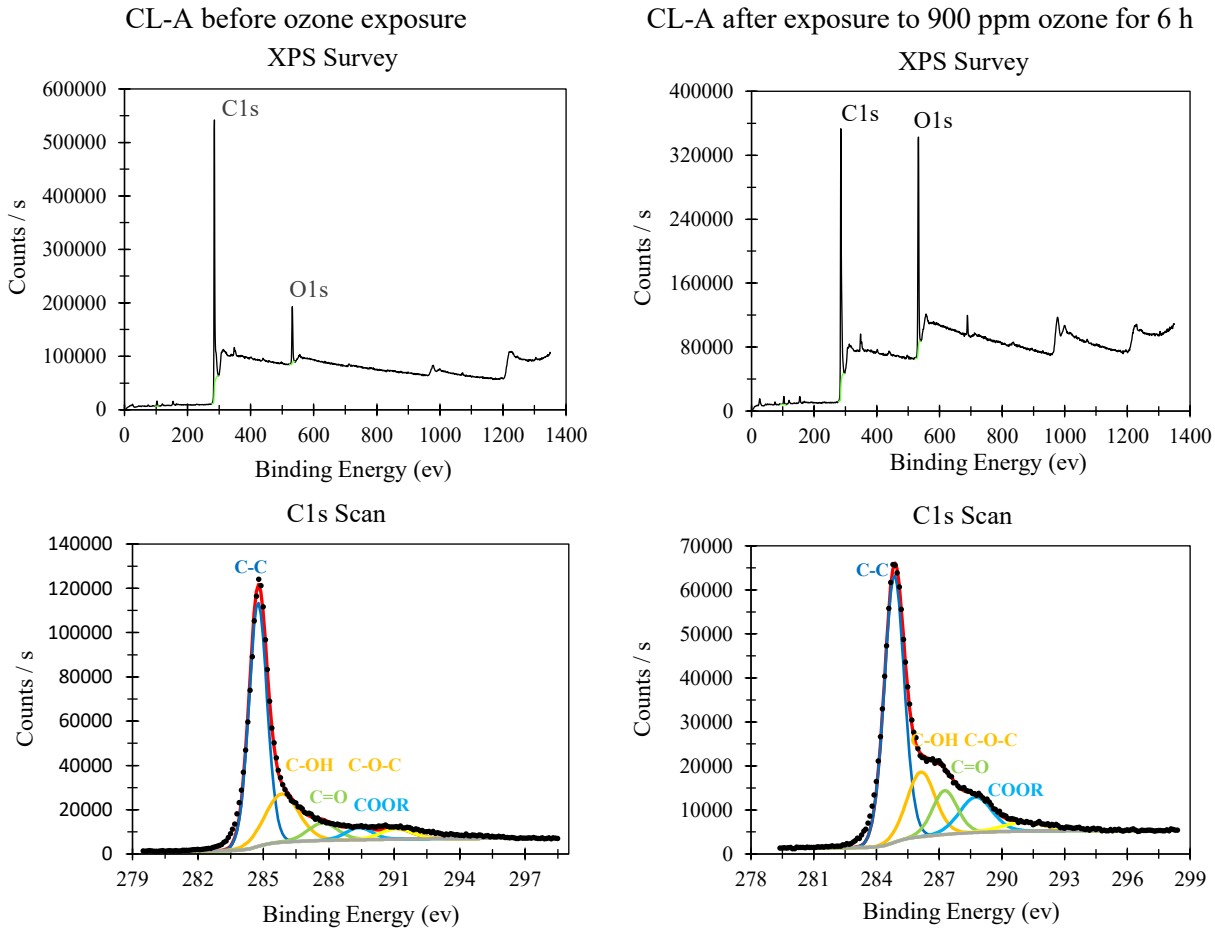

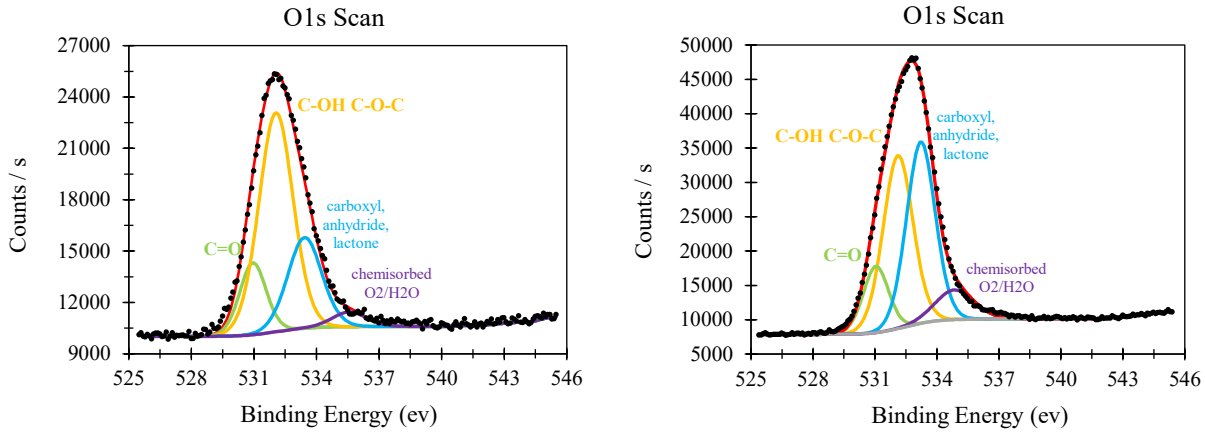

Figure S 3.3. XPS spectra of CL-A before and after exposure to 900 ppm ozone; survey scan and high-resolution scans of C1s and O1s. The amount of oxygen is increased after exposure to ozone (survey scan). Also, the surface chemistry has changed (high resolution scans)

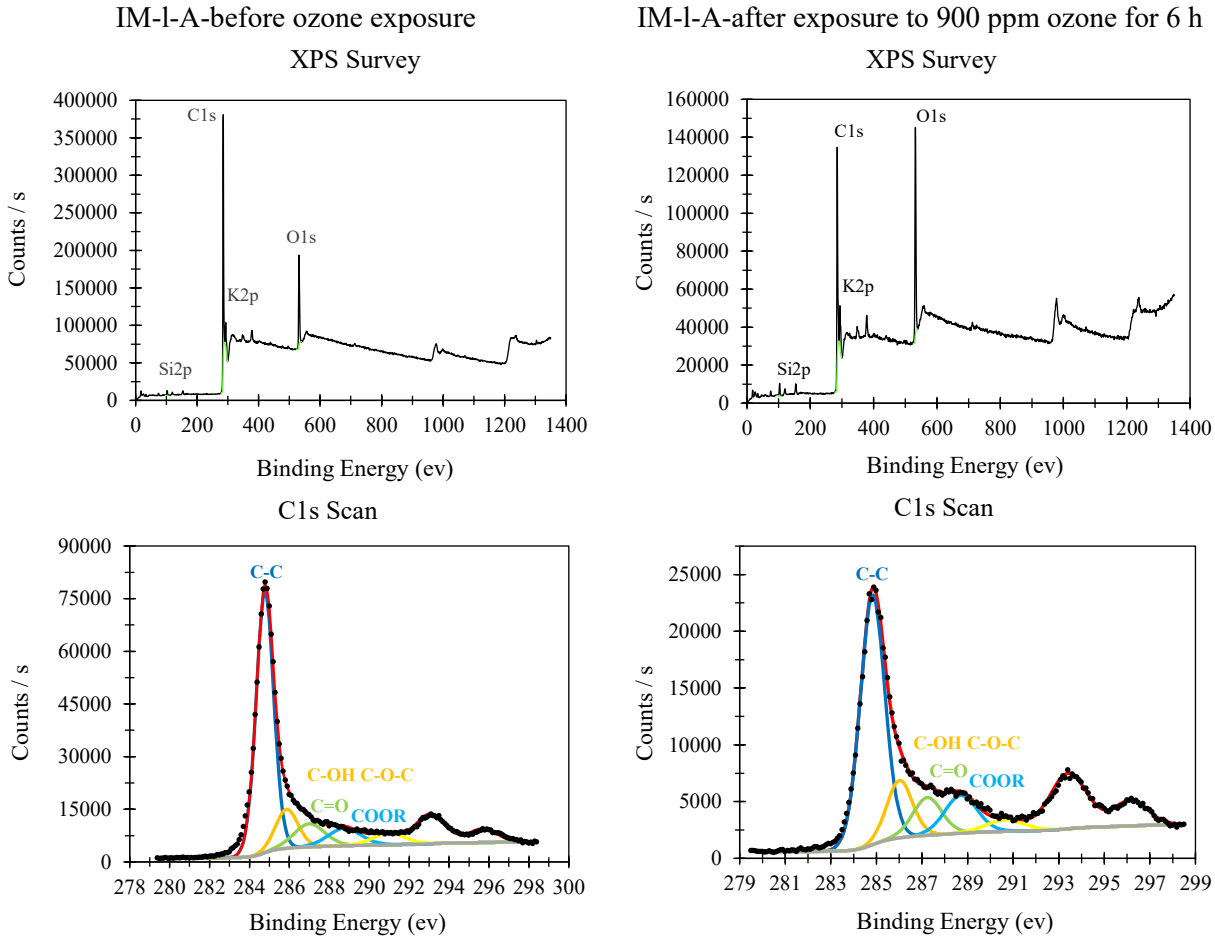

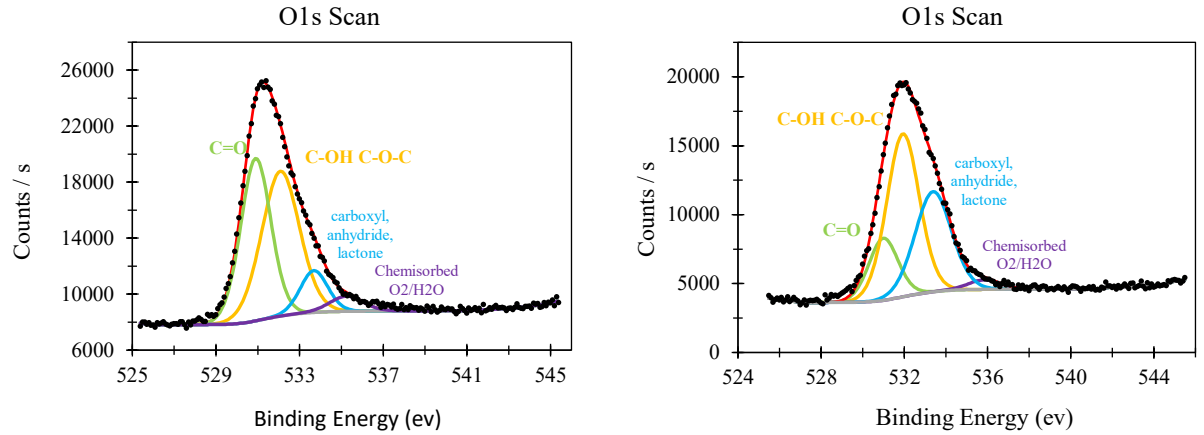

Figure S 3.4. XPS spectra of IM-l-A before and after exposure to 900 ppm ozone; survey scan and high-resolution scans of C1s and O1s. IM-l-A has potassium on its surface compared to CL-A. The potassium caused the peaks at 293.5 ev and 296 ev in the C1s high resolution scan spectra. The amount of oxygen is increased after exposure to ozone (survey scan). Also, the surface chemistry has changed (high resolution scans)

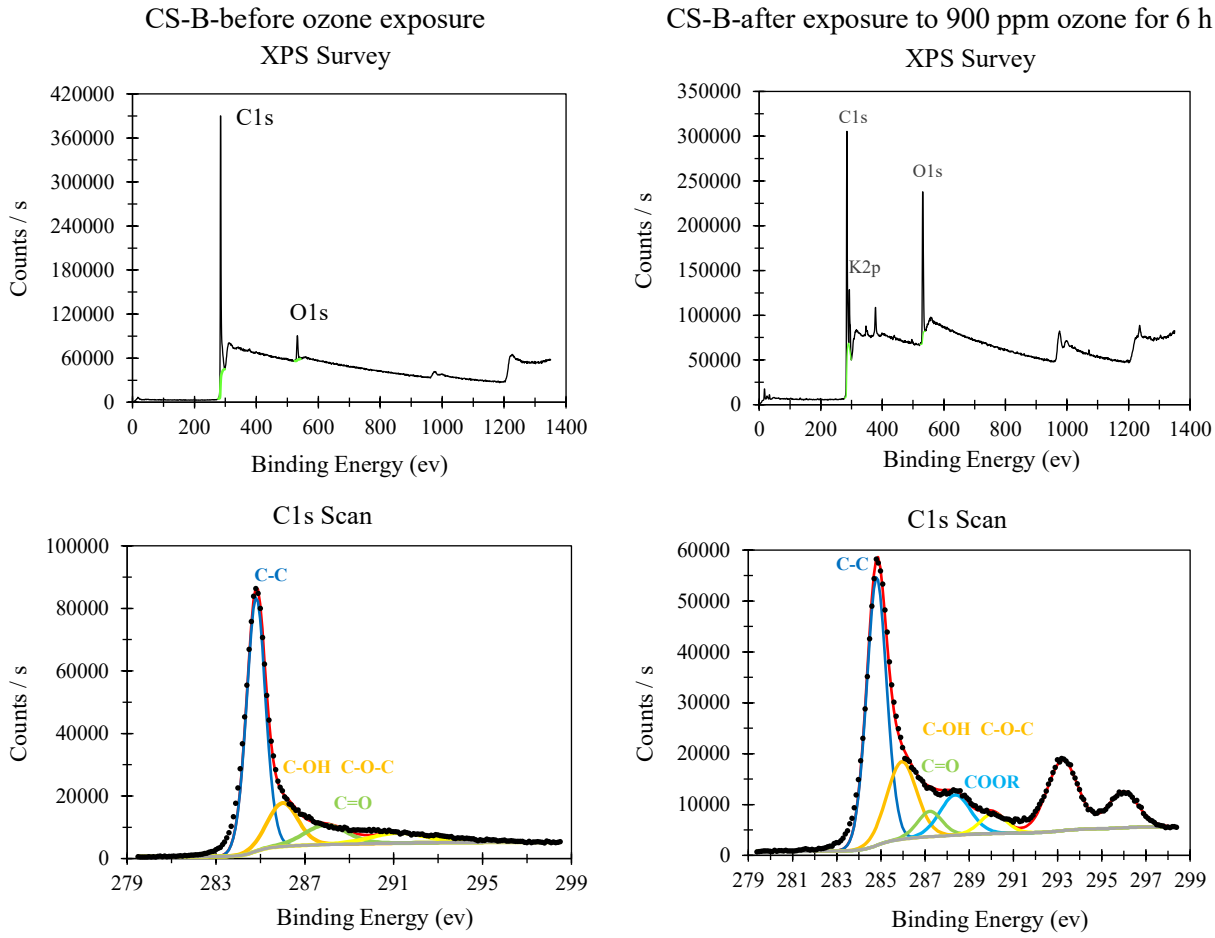

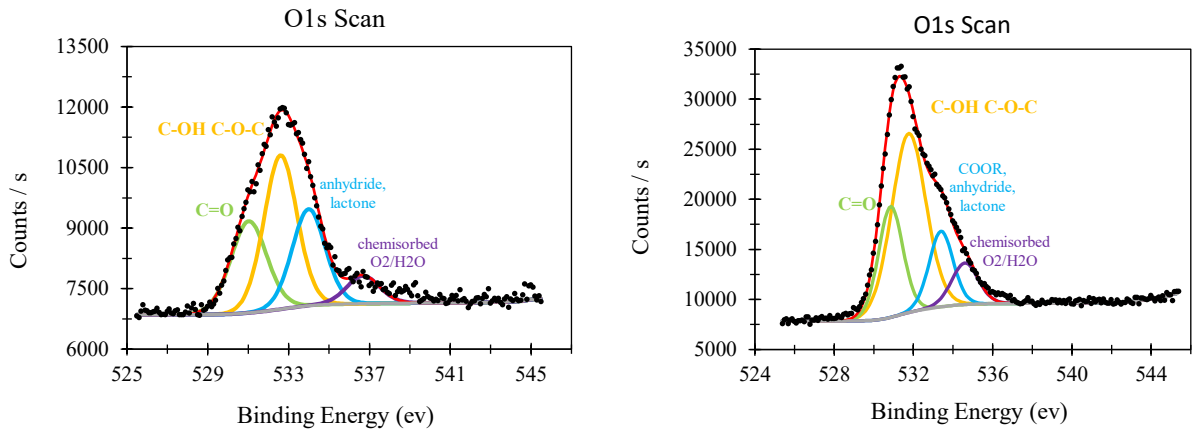

Figure S 3.5. XPS spectra of CS-B material: survey scan and high-resolution scan of C1s, and O1s. After exposure to ozone, potassium atoms are detected on the surface. The presence of potassium causes the peaks at 293.2 ev and 296 ev in C1s high resolution scan after exposure to ozone.

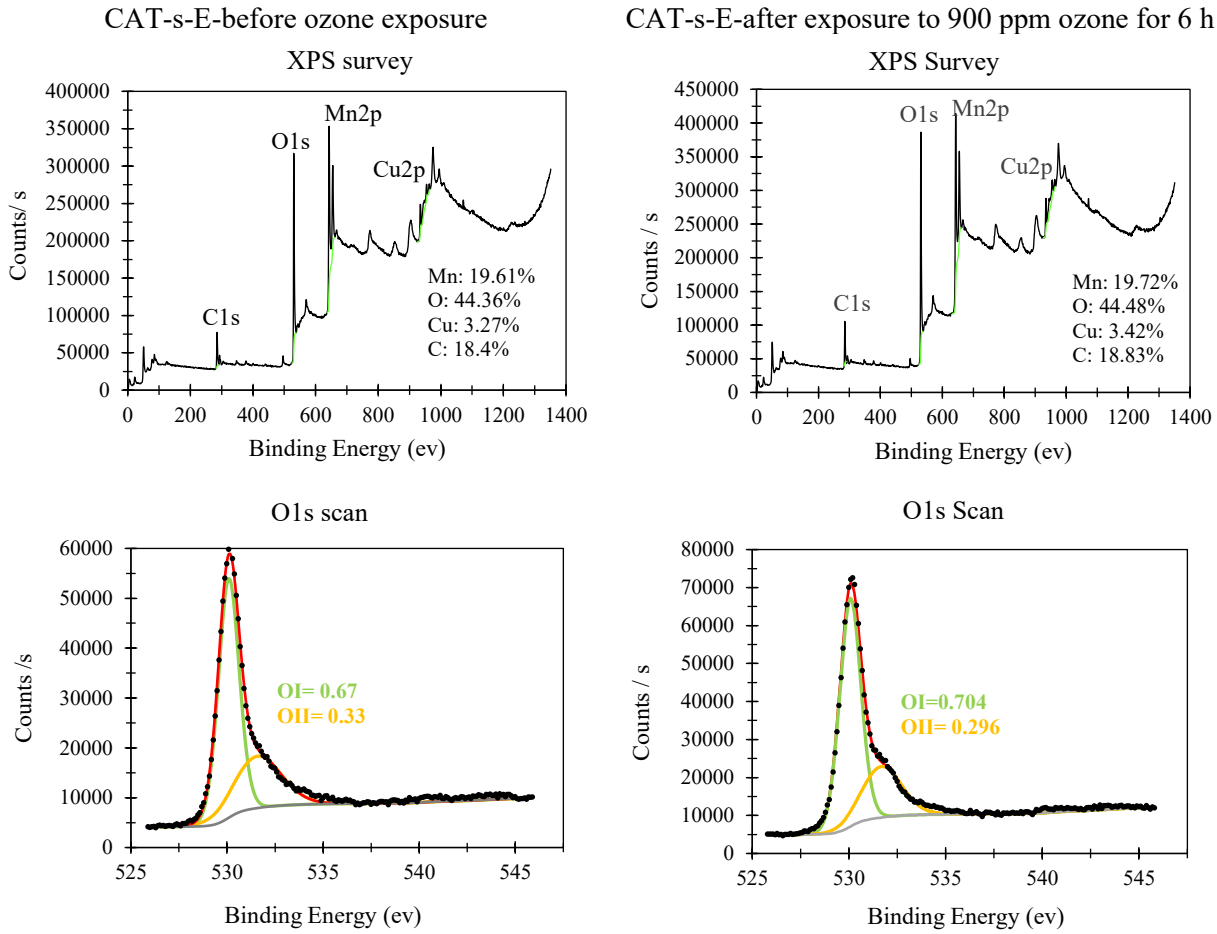

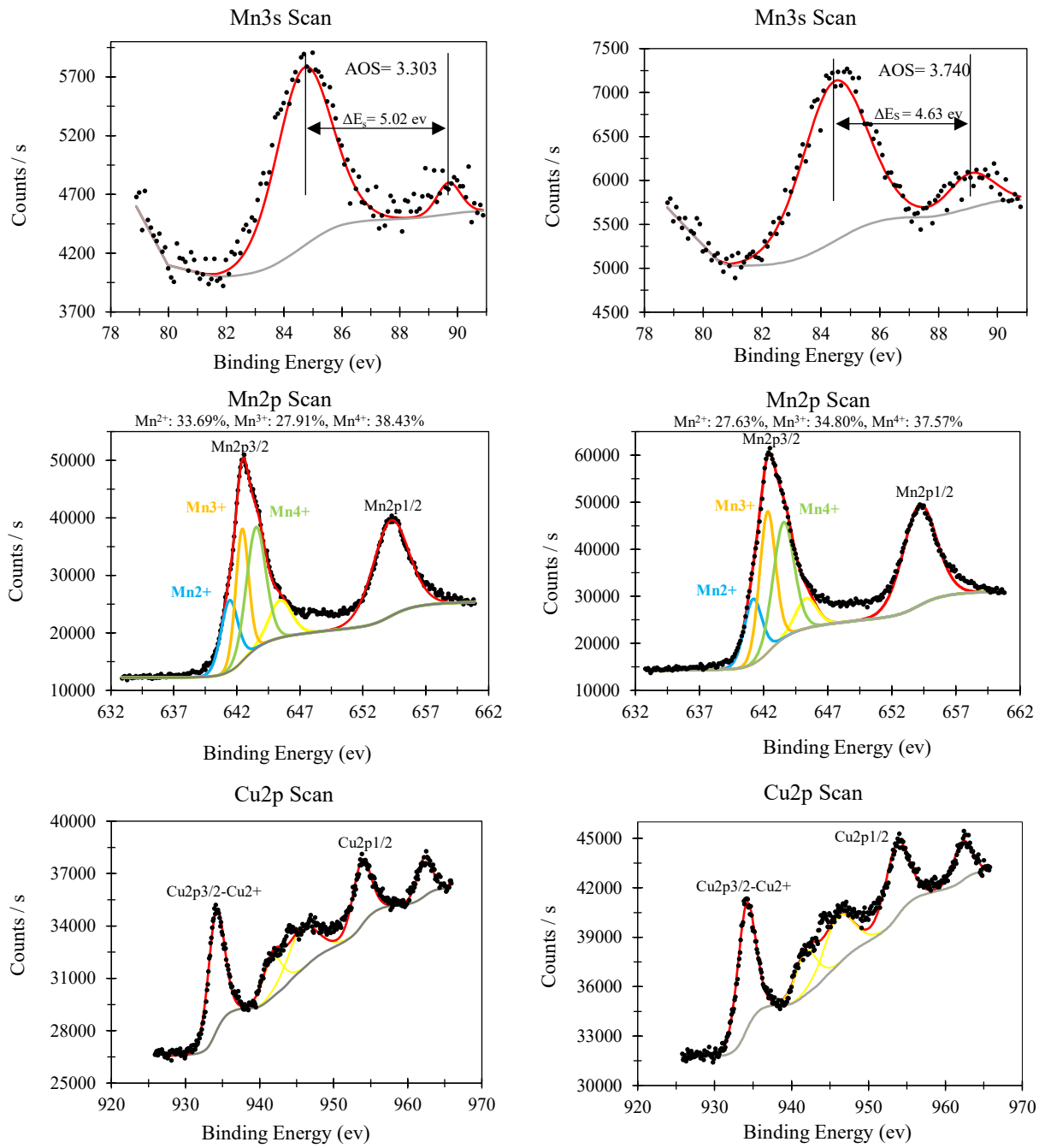

Figure S 3.6. XPS spectra of CAT-s-E material: survey scan and high-resolution scan of Mn3s, Mn2p, O1s, and Cu2p.

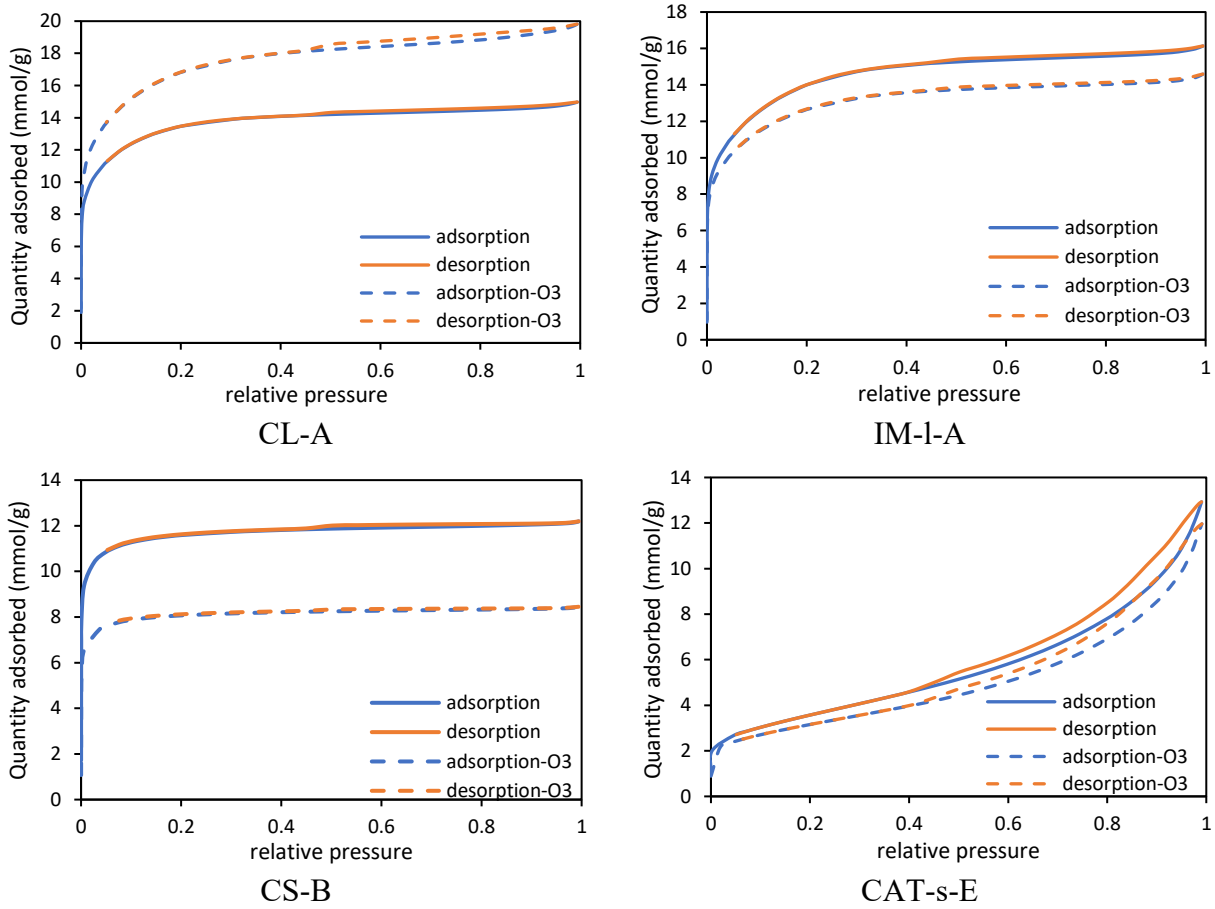

Figure S 3.7. Nitrogen adsorption-desorption isotherm of CL-A, IM-l-A, CS-B, and CAT-s-E. AC-based samples affected by ozone much more than the CAT-s-E (solid lines before exposure to ozone; dashed lines after exposure to 900 ppm ozone).

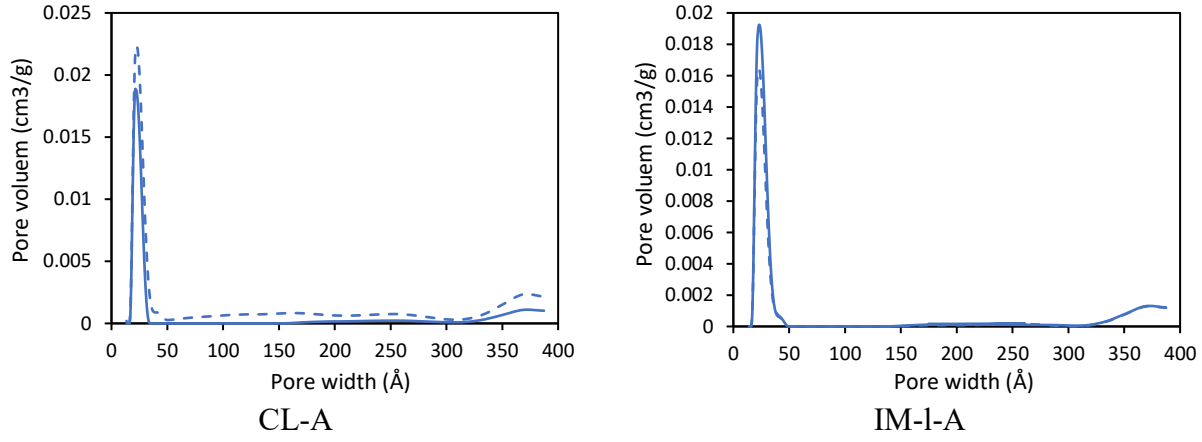

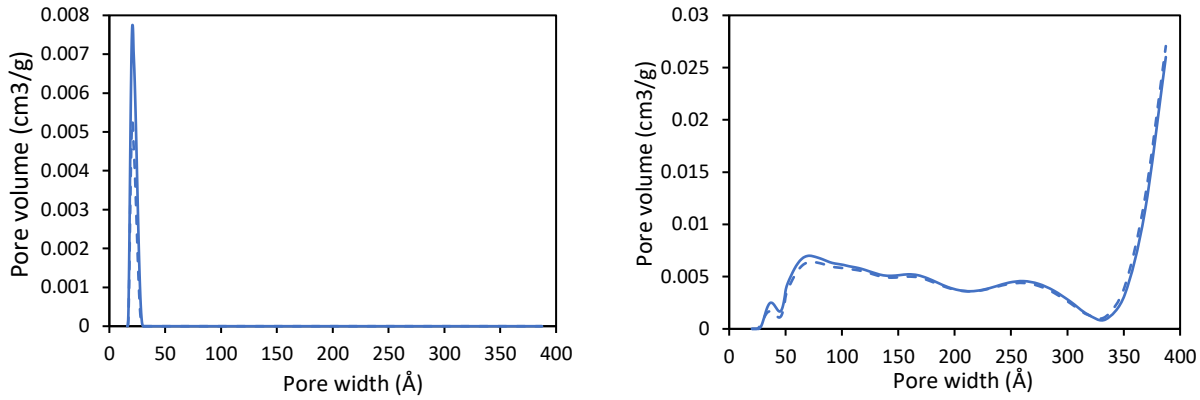

CS-B CAT-sE

Figure S 3.8. Pore size distribution of CL-A, IM-l-A, CS-B, and CAT-s-E before and after ozone exposure (solid lines: before exposure, dashed lines after exposure to 900 ppm ozone for 6 h). The pore volume of micropores decreased after ozone exposure for IM-l-A, and CS-B. On the other hand, the pore volume of CL-A increased after ozone exposure. The pore size distribution of CAT-s-E is unaffected by ozone exposure.

Chapter 4. The effect of operational conditions on the performance of granular ozone removal media: Statistical experimental design and kinetic modeling

4.1. Abstract

Ozone, a strong oxidizer, and a hazardous air pollutant can adversely affect human health and the environment; therefore, its concentration must be kept within a specific limit. Several ozone removal technologies are available for this purpose, which may be used under different operational conditions. Despite the selection flexibility that these technologies bring about, they raise the need to better understand the feasibility of each technique for various applications. Such a broad perspective, however, is currently lacking due mainly to the cost and resources required for comprehensive studies. Using a statistical design approach, this study aims to address this important gap. The fractional factorial method, as a reliable statistical technique, was used to study the effect of ozone concentration, humidity level, airflow rate, and media volume on the ozone removal performance of common granular materials including different types of activated carbon (CL-A: coal-based, CS-B: coconut shell-based, IM-l-A: coal-based impregnated with KOH) and a catalyst (CAT-E). The role of individual parameters and their interactions were studied. The results show that depending on the physicochemical properties of the material, humidity could substantially improve or deteriorate its performance. Among the materials tested across all operational conditions, on average, CL-A showed the poorest performance (mean efficiency=62%, standard deviation=0.31), CS-B was highly sensitive to operational conditions (efficiency was varied from 25% to 100% at different humidity levels), IM-l-A showed the highest efficiency robustness among activated carbon media (mean efficiency=77.6%, standard deviation=0.20), and CAT-E featured the best performance (mean efficiency=86.5%, standard deviation=0.16). Additionally, the data were fitted into a packed bed kinetic model that elucidated physicochemical mechanisms underlying distinctive behaviors of each tested material.

4.2. Introduction

Ozone is a well-known oxidizing agent with extensive application in water treatment, and food, agriculture, and pulp and paper industries [127], [149] which is expected to have a market share of more than $1.22 billion by 2028 [150]. Ozone is generated by means of ozone generators for direct industrial use [127] or as a by-product in commercial and industrial devices such as photocopiers, laser printers, and welding machines, which can increase the ozone concentration beyond the permissible limits [151]–[154]. The prolonged exposure to ozone puts workers' health

at risk [127], [152]–[156], causing respiratory inflammation, lung damage, and exacerbating cardiovascular problems and asthma [124], [127], [157], [158]. Such adverse effects oftentimes manifest at the population levels as statistical surveys report a strong link between the daily increase in ambient ozone level and surge in hospital visits and consequently higher mortality rates [159], [160]. Also, high ozone level has environmental hazards such as damaging plants in addition to reducing crop yields and wildlife food [161]. To protect the workers' and occupants' health and safety, and protect the environment, ozone removal technologies are required.

Despite the common need for ozone removal technologies in various applications, industrial and commercial systems differ widely in operational conditions. As reported earlier [10], [124], [127], [162], ozone concentration level, humidity level, and residence time are among the key factors affecting granular media performance—ozone influences the consumption rate of active sites and it can change the physical characteristics of the material [162], humidity can deactivate the active sites [10], [127], and residence time plays a key role in the kinetics of ozone decomposition reaction. These parameters span a wide range of industrial applications. For instance, in the exhaustion pathway of the ozone generator system in a water treatment plant, the ozone concentration and humidity levels are significantly high while in the ventilation system of an ozone-related industry the ozone concentration is relatively low and variable, the airflow rate is high, and the humidity level is moderate. Thus, understanding the effect of operational parameters on the performance of ozone removal media is crucial and facilitates selecting the best technology for each application.

Various statistical experimental design methods exist to identify the effect of operational parameters on the media performance including one-factor-at-a-time, full factorial, fractional factorial, and response surface [163]. Due to their ability to reduce the experimental runs, the fractional factorial design method has been preferred in numerous studies to identify the effect of parameters and their interactions [164]–[169], and optimize the process operational conditions [165], [168], [170]. Despite fewer runs than full factorial designs, fractional factorial design outputs the most significant parameters in addition to the effect of some of the interactions in the form of a mathematical model [163]. Identifying the key parameters and their range is highly important in designing the fractional factorial to achieve a thorough model. The selected range should be large enough so that the response variation substantially exceeds experimental error

[169], [171]. Therefore, using an appropriate experimental framework with the ability to produce a wide range of conditions is necessary to obtain accurate models.

Eleven different granular media were investigated according to the ASHRAE 145.1 standard test method in a bench-scale test set-up [162], where we used this method to capture a wide range of ozone removal performances over a practical experimental timescale of a few hours. This study used a similar bench-scale test set-up capable of varying experimental conditions to analyze the impact of operational parameters including ozone concentration level, humidity level, airflow rate, and the media volume on the ozone removal performance of four widely used commercial granular media, exploiting statistical experimental design and kinetic modeling. The tested media include: a coal-based activated carbon (CL-A), a coal-based activated carbon impregnated with KOH (IM-l-A), a coconut shell-based activated carbon (CS-B), and a MnO_2-CuO catalyst (CAT-E). The fractional factorial design (half fraction) with two replicates and resolution IV, which is the highest possible resolution consistent with half fraction, was conducted using Minitab software to perform the statistical analysis. Furthermore, to discuss the results of statistical analysis and gain mechanistic insights into the effect of operational parameters on the materials' performance an empirical kinetic model was proposed and fitted to the experimental data, resulting in obtaining the ozone decomposition rate constant of each material and their deactivation rate constant.

4.3. Methodology

4.3.1. Fractional factorial design

Among the key operational parameters affecting the ozone removal performance, humidity level, ozone concentration, and residence time, which is adjustable by changing the airflow rate and loading volume, were selected. To study the effect of these parameters (humidity level, ozone concentration level, airflow rate, and media volume), two levels, a high (+1) and a low (-1), were assigned to each (Table 3.1). The selected ranges should be large enough to cause changes that exceed experimental error [163], [169]: (i) the high humidity level (70%) was selected based on the high end of comfort zone; (ii) the ozone concentration level was selected based on the previous study [162], where at 1 ppm no changes were observed in the performance and above 650 ppm increasing the ozone level had no effect; therefore, 10 ppm and 600 ppm were selected as the low and high level; (iii) a wide range of residence time was included, from 0.05 s (half of the 0.1 s suggested by the ASHRAE 145.2 test method) to 0.75 s (more than 0.7 s suggested for granular catalysts) by varying the airflow rate and loading volume.

With four parameters, each in two levels, the number of experimental runs using half fractional factorial design is 8 ($^1/_2 \times (2^4\ number\ of\ required\ runs\ for\ a\ full\ factorial\ design)$). Each run was repeated twice to enable the analysis of variance. Three centre points (0) were added to verify the significance of the curvature. Therefore, in total 19 experimental runs were given for each material to be carried out in the bench scale test set-up (Figure 4.1). The experiments were done randomly (based on the random order that the design assigns) to minimize the effect of unknown parameters such as operator error. A summary of the experimental conditions is presented in Table 4.1.

According to the fractional factorial design, none of the main effects are aliased with the two-way interactions; however, two-way interactions are aliased with one another. Since it was desired to investigate the effect of all the two-way interactions, the design should have been de-aliased by adding extra experimental runs. The design of extra runs for de-aliasing is presented in Table 4.2.

After performing the experiments and analyzing the data, a regression model (Equation 4.1) was established for each material (higher than two-way interaction terms were not considered):

$$\eta = \beta_0 + \beta_1 A + \beta_2 B + \beta_3 C + \beta_4 D + \beta_{12} AB + \beta_{13} AC + \beta_{14} AD + \beta_{23} BC + \beta_{24} BD + \beta_{34} CD + \varepsilon \quad (4.1)$$

where, η is the ozone conversion, β_0, β_i, and β_{ij} are the regression coefficients for intercept, linear coefficients, and interaction coefficients, respectively. A, B, C, and D represents the operational parameters in coded units, and ε is the error term. The regression coefficients are estimated based on the least square method. The adequacy of the regression model was verified by calculating R^2, adjusted R^2 (R^2_{adj}), and R^2 of prediction (R^2_{pred}) and using the normal probability plot of standardized residuals.

Besides the adequacy of the regression model, the ANOVA table was tabulated using the Minitab software, in which the significance of each model term is expressed by the *p-value*. In this study, a *p-value* less than 0.05 defined a significant effect. Then, the insignificant terms were removed to obtain the reduced model and the ANOVA table for the reduced model was obtained. Other statistical analyses including the normal probability plot of standardized effects, Pareto chart of standardized effects, and residual plots, were done by the software.

Table 4.1. Design of experiment, ½ fractional factorial design. -1 is the lower level, +1 is the upper level and 0 is the center point. For humidity level: -1 (0%), 0 (35%), and +1 (70%); ozone concentration: -1 (10 ppm), 0 (305 ppm), and +1 (600 ppm); airflow rate: -1 (2 L/min), 0 (8.5 L/min), and +1 (15 L/min); media loading: -1 (12.5 mL), 0 (18.75 mL), and +1 (25 mL).

Standard Order	Run Order	Center Pt	Humidity level	Ozone concentration	Airflow rate	Media loading	Residence time (s) *
1	13	1	-1	-1	-1	-1	0.375
2	4	1	1	-1	-1	1	0.75
3	12	1	-1	1	-1	1	0.75
4	6	1	1	1	-1	-1	0.375
5	1	1	-1	-1	1	1	0.1
6	17	1	1	-1	1	-1	0.05
7	7	1	-1	1	1	-1	0.05
8	16	1	1	1	1	1	0.1
9	14	1	-1	-1	-1	-1	0.375
10	19	1	1	-1	-1	1	0.75
11	8	1	-1	1	-1	1	0.75
12	11	1	1	1	-1	-1	0.375
13	18	1	-1	-1	1	1	0.1
14	10	1	1	-1	1	-1	0.05
15	5	1	-1	1	1	-1	0.05
16	2	1	1	1	1	1	0.1
17	9	0	0	0	0	0	0.132
18	15	0	0	0	0	0	0.132
19	3	0	0	0	0	0	0.132

$^{*}residence\ time = {loading\ volume\ (mL)}\Big/{airflow\ rate\ (\frac{mL}{s})}$

Table 4.2. The design of extra experimental runs to de-alias the original design

Run Order	Center Pt	Humidity level	Ozone concentration	Airflow rate	Media loading	Residence time
20	1	-1	-1	-1	1	0.75
21	1	1	1	-1	1	0.75
22	1	-1	1	-1	-1	0.375

4.3.2. The experimental setup

The designed bench scale test set-up (Figure 4.1) consists of two reactors in parallel to increase the throughput. The carrier gas was compressed air and its total flow rate was controlled by a mass flow controller. The airflow rate through each reactor was measured from the reactors' outlet and was controlled at the required levels (2 L/min, 8.5 L/min, and 15 L/min) by means of rotameters before each reactor (Figure 4.1). A humidifier was used to adjust the humidity level (0%, 35%, and

70%). Before ozone injection, the humidified air was passed through the reactors until the humidity level before and after the reactors became equal. Ozone was generated at 10 ppm level by a vacuum UV lamp in a pressure vessel with compressed air as the feed gas and was injected into the mainstream. Higher ozone levels (305, and 600 ppm) were produced by an ozone generator (BMT 203, Germany) with oxygen as the feed gas. All the measured operational parameters are presented in Table S4.1.

The ozone decomposition reactor is made of glass and polytetrafluoroethylene (PTFE). Within the reactor, the media holder is a PTFE tube with a specific volume (12.5 mL, 18.75 mL, 25 mL). Inside the PTFE tube, the media was sandwiched between two meshes made of perfluoroalkoxy (PFA). The ozone concentration was measured before and after the reactor by an ozone monitor (3-channel 2B Technologies 106M). Before testing the media, the ozone concentration before and after the empty reactor was measured, ensuring that the reactor itself did not remove any ozone.

The ozone removal performance of the media was reported in terms of conversion (Equation 4.2), calculated using the measured ozone concentration before and after the reactor.

$$\eta = \frac{C_{inlet} - C_{outlet}}{C_{inlet}} \tag{4.2}$$

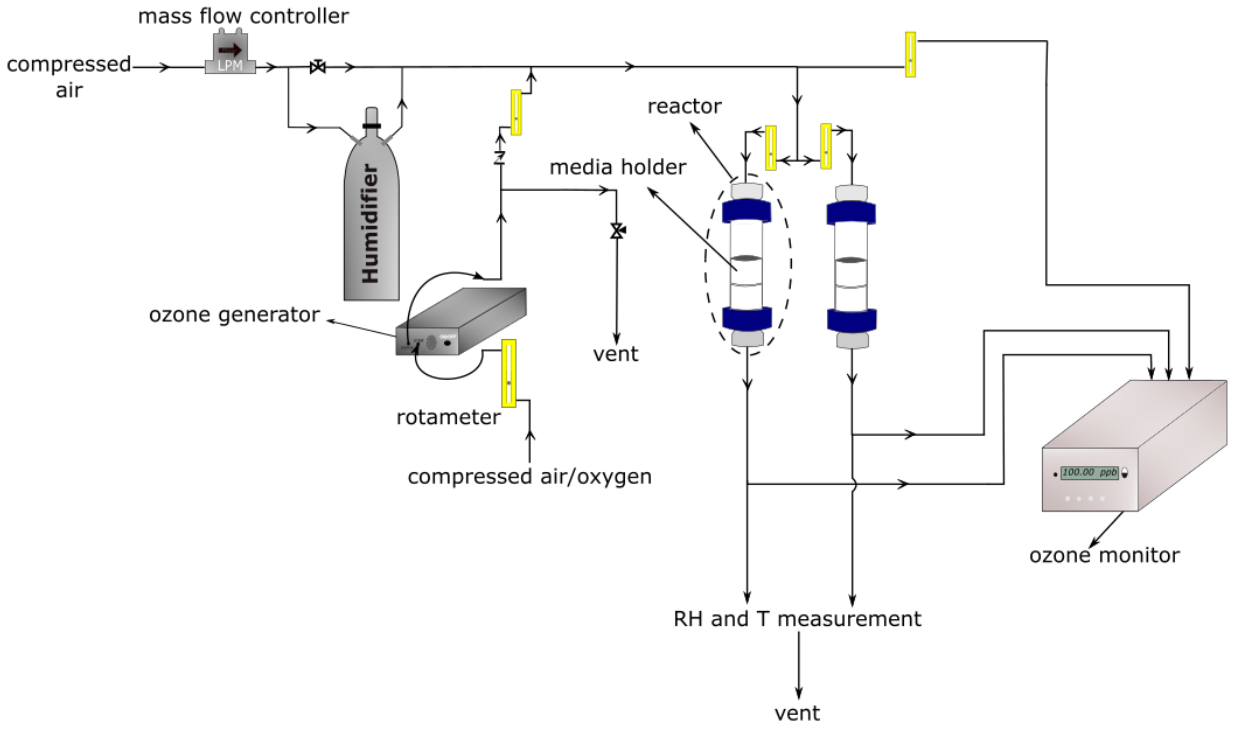

Figure 4.1. Bench-scale test set-up layout. All the tubes are made of PTFE. The tube size is ¼ inch. The rotameters, valves, and fittings exposed to ozone are made of ozone-compatible materials like stainless steel, PTFE, and polyvinylidene fluoride (PVDF).

4.3.3. Kinetic model

A kinetic model was developed, assuming the ozone reaction is first order, based on the model proposed by Fogler [172] for packed beds containing porous media with axially dispersed plug flow, assuming that the ozone reaction is first order, there is no radial dispersion within the bed, the air velocity and temperature are uniform and constant, and the granules are uniformly distributed in the bed and their physical characteristics such as specific surface area and porosity remain constant during the reaction [124], [172]–[174]:

$$\frac{\partial C}{\partial t} = D_a \frac{\partial^2 C}{\partial z^2} - u\frac{\partial C}{\partial z} - k'' \rho_b S\, a\, C\, \Omega \tag{4.3}$$

$$\frac{da}{dt} = -k_d\, a^{n1}\, C^{n2} \tag{4.4}$$

Initial conditions:

$$t = 0 \;:\; C = 0\,, a = 1 \tag{4.5}$$

Boundary conditions:

$$z = 0 : C = C_0 \tag{4.6-1}$$

$$z = L \;:\; \frac{\partial C}{\partial z} = 0 \tag{4.6-2}$$

where, C ($\frac{mol}{m^3}$) is the ozone concentration in the bulk, *t (s)* is the time, *z (m)* is the axial coordinate, D_a ($\frac{m^2}{s}$) is the axial dispersion coefficient (Appendix A), u($\frac{m}{s}$) is the face velocity, k'' ($\frac{m}{s}$) is the reaction rate, ρ_b $\left(\frac{g}{m^3}\right)$ is the material's bulk density, S ($\frac{m^2}{g}$) is the material's specific surface area, a is the activity of the material, k_d($\frac{1}{s}$ ($\frac{m^3}{mol}$)^{n2}) is the activity decay rate, Ω is the overall effectiveness factor (Appendix A), C_0 ($\frac{mol}{m^3}$) is the inlet ozone concentration, and L (m) is the packed bed length.

To solve the system of equation, first, they were nondimensionalized as follows. Non-dimensionalized equations enable identifying the most important parameter and make it feasible to compare the importance of each term relatively. Also, it is helpful in reducing the stiffness of the equation and increasing the numerical stability.

$$C' = \frac{C}{C_0} \;\; ; \;\; z' = \frac{z}{L} \;\; ; \;\; t' = \frac{t}{t_f} \tag{4.7}$$

where C_0 ($\frac{mol}{m^3}$) is the inlet ozone concentration, L (m) is the packed bed length, and t_f (s) is the reaction duration.

The nondimensionalized system of equations are:

$$\frac{\partial C'}{\partial t'} = \frac{D_a\, t_f}{L^2}\frac{\partial^2 C'}{\partial C'^2} - \frac{u\, t_f}{L}\frac{\partial C'}{\partial z'} - k''\rho_b S\, a\, C'\Omega\, t_f \quad (4.8)$$

$$\frac{da}{dt'} = -k_d\, a^{n1}\, C'^{n2}\, {C_0}^{n2}\, t_f \quad (4.9)$$

Initial conditions:

$$t' = 0\ : C' = 0\,, a = 1 \quad (4.10)$$

Boundary conditions:

$$z' = 0 : C' = 1 \quad (4.11-1)$$

$$z' = 1\ :\ \frac{\partial C'}{\partial z'} = 0 \quad (4.11-2)$$

Then, the nondimensionalized system of equations (Equations 4.8 to 4.11) were numerically solved in Python, using scipy.integrate.solve_ivp, and were fitted to the experimental data (the ratio of ozone concentration in the outlet to the inlet), using scipy.optimize.curve_fit, to determine k'', k_d, n_1, and n_2.

4.3.4. Characterization

The specific surface area of media was calculated using the N_2 adsorption-desorption isotherm obtained from the MicroActive TriStar II Plus instrument (Micromeritics Instrument Co.) based on the Brunauer-Emmet-Teller theory (S_{BET}).

The pore volume and pore size distribution were determined based on nonlocal density functional theory (NLDFT) using the same isotherms; this method is applicable for pores with a diameter less than 400 Å. To include the pores with greater sizes in the pore volume and pore size distribution analysis Mercury intrusion porosimetry was done, using the MicroActive AutoPore V instrument. Because of the different sizes of nitrogen and mercury molecules, by performing both techniques, a wide range of pore diameters were included in the porosimetry analysis.

4.4. Results and Discussion

4.4.1. Preliminary evaluation of the results

The ozone removal performance of media after 6 h exposure to ozone, where the ozone concentration in the outlet became almost stable, at the conditions given by the experimental design are presented in Table S4.2. These data were first used to illustrate the direct effect of parameters, excluding interactions, in Figure 4.2. The operational conditions of airflow rate, ozone concentration, loading volume, and humidity were determined to substantially impact the reactor yield in most cases. Notably, these responses are non-linear in several cases, particularly for the

AC-based media where deviations of the center points from the dashed-blue line were shown to be more significant. The degree of significance of operational parameters along with their two-way interactions was more rigorously investigated using the Minitab software to calculate the p-value (Table 4.3), and plot the normal probability of standardized effects (Figure 4.3-A) and Pareto chart (Figure 4.3-B). Normal probability of standardized effect shows the direction and significance of the regression model variables, and Pareto chart (Figure 4.3) shows the absolute values of the standardized effect. The reference line in the Pareto chart is calculated based on the significance level (here is 0.05), and each variable that crosses this line is considered statistically significant. Since Pareto chart shows the absolute value, thus it makes it feasible to compare the magnitude of the effects.

Initially, all the parameters and their two-way interactions were considered in the regression model. After conducting an analysis of variance (ANOVA), the parameters with p-value>0.05 were removed to reduce the deviation of residuals from normality in the normal probability plot of standardized residuals, and to prevent over fitting (p-value>0.05 represent statistically insignificant) [163]. Then, only the statistically significant parameters were retained. A summary of the software's output including the coded coefficients and the ANOVA is presented in Table 4.3. The advantage of coded coefficients is that the absolute value of the factor's coefficient is a true indicator of the effect of that factor. The coded coefficients thus allow comparing the effect of the factors on the ozone removal performance among different media.

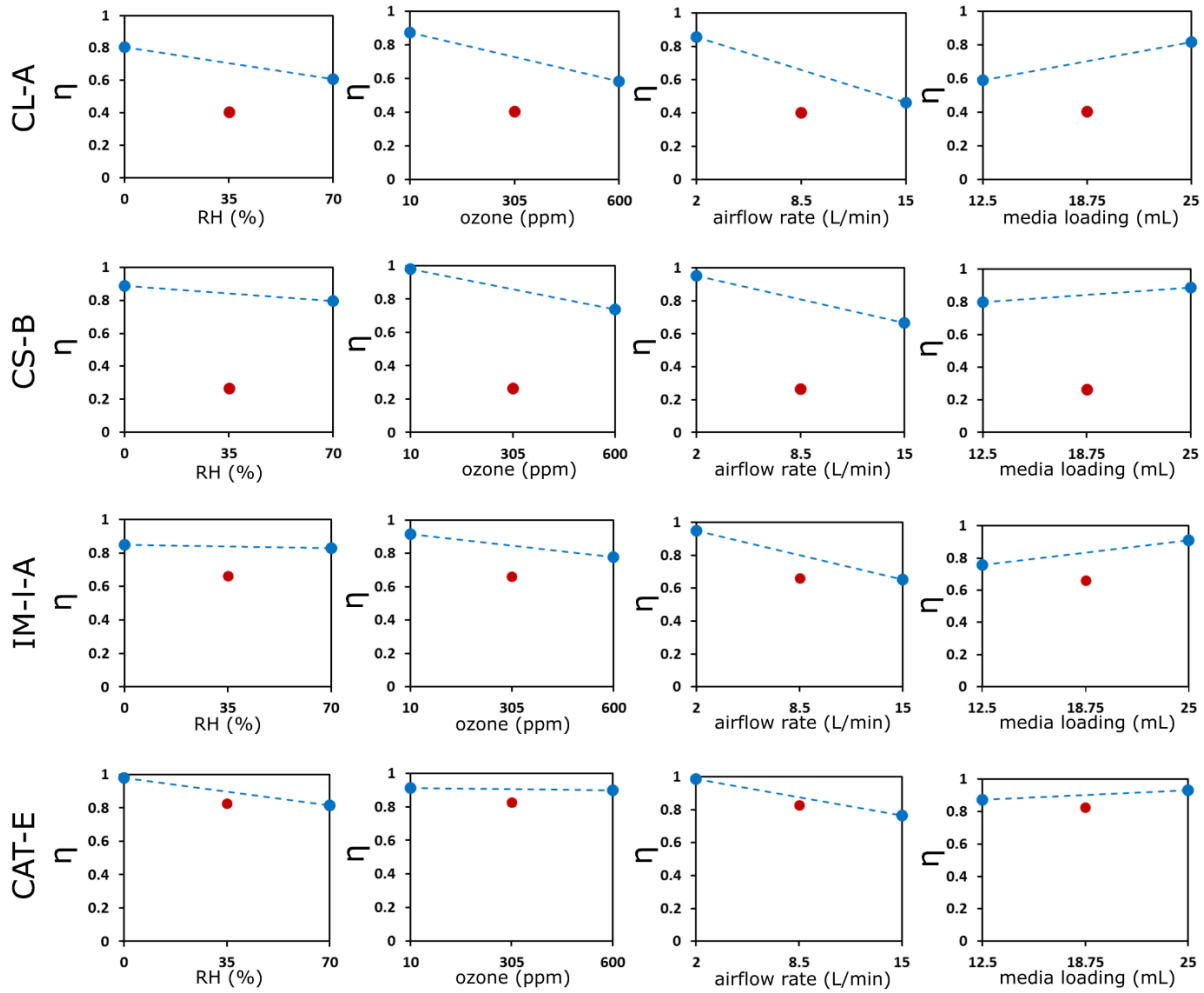

Figure 4.2. The main effect of the operational parameters on the media's ozone removal performance after 6 h exposure to ozone. The main effect of each parameter (positive or negative) was revealed by averaging the responses at each parameter's level obtained from the experiments. The red circle is the center point. The deviation of the red circle from the dashed blue line shows non-linearity.

Table 4.3. The obtained results from the Minitab software (using the ozone removal conversion of the media after 6 h exposure to ozone) include coded coefficient [a] for each factor, p-value [b] of each factor, the regression model, and the model summary. (A: RH, B: O_3 concentration, C: airflow rate, D: loading volume)

	CL-A		CS-B		IM-I-A		CAT-E	
	Coded Coef.[a]	P-value[b]	Coded Coef.	P-value	Coded Coef.	P-value	Coded Coef.	P-value
Model	N/A	0.00	N/A	0.00	N/A	0.00	N/A	0.00
Linear	N/A	0.00	N/A	0.00	N/A	0.00	N/A	0.00
A	-0.11	0.00	-0.04	0.00	-	-	-0.1	
B	-0.18	0.00	-0.17	0.00	-0.09	0.00	-0.02	0.00
C	-0.20	0.00	-0.13	0.00	-0.15	0.00	-0.11	0.00
D	0.11	0.00	0.04	0.00	0.07	0.00	0.03	0.00
2-way interaction	N/A	0.00	N/A	0.00	N/A	0.00	N/A	0.00
A*B	-0.03	0.004	-	-	-	-	-	-
A*C	-0.06	0.00	-	-	-	-	-0.08	0.00
A*D	0.02	0.015	0.04	0.00	-	-	0.02	0.00
B*C	-0.08	0.00	-0.15	0.00	-0.08	0.00	-0.01	0.00
B*D	0.05	0.00	-	-	-	-	-	-
C*D	0.02	0.037	-0.02	0.02	0.03	0.00	0.01	-
Curvature[c]	N/A	0.00	N/A	0.00	N/A	0.00	N/A	0.00
Lak-of-fit[d]	N/A	-	N/A	0.31	N/A	0.23	N/A	0.51
Fitted regression model for ozone conversion	0.66 – 0.11 * A – 0.18 * B – 0.20 * C + 0.11 * D – 0.03 * A*B – 0.06 * A*C + 0.02 * A*D – 0.08 * B*C + 0.05 * B*D + 0.02 * C*D – 0.25 * CtPt		0.80 – 0.04 * A – 0.17 * B - 0.13 * C + 0.04 * D + 0.04 * A*D – 0.15 * B*C – 0.02 * C*D – 0.53 * CtPt		0.79 – 0.09 * B – 0.14 * C + 0.07 * D – 0.08 * B*C – 0.13 * CtPt		0.87 – 0.10 * A – 0.02 * B – 0.11 * C + 0.03 * D – 0.08 * A*C + 0.02 * A*D – 0.01 * B*C – 0.05 * CtPt	
R^2 (%)	99.68		99.21		98.78		99.78	
R^2_{adj} (%)	99.40		98.82		98.37		99.65	
R^2_{pred} (%)	98.73		97.89		97.37		99.35	

[a] Coded coefficient: the coefficient describes the size and direction of the relationship between a term in the model and the response variable.

[b] p-value: the p-value is a probability that measures the evidence against the null hypothesis. Lower probabilities provide stronger evidence against the null hypothesis. p-value<0.05: rejects the null hypothesis

[c] Curvature: a curved relationship between the factors and the response

[d] If the p-value is larger than 0.05, you cannot conclude that the model does not fit the data well

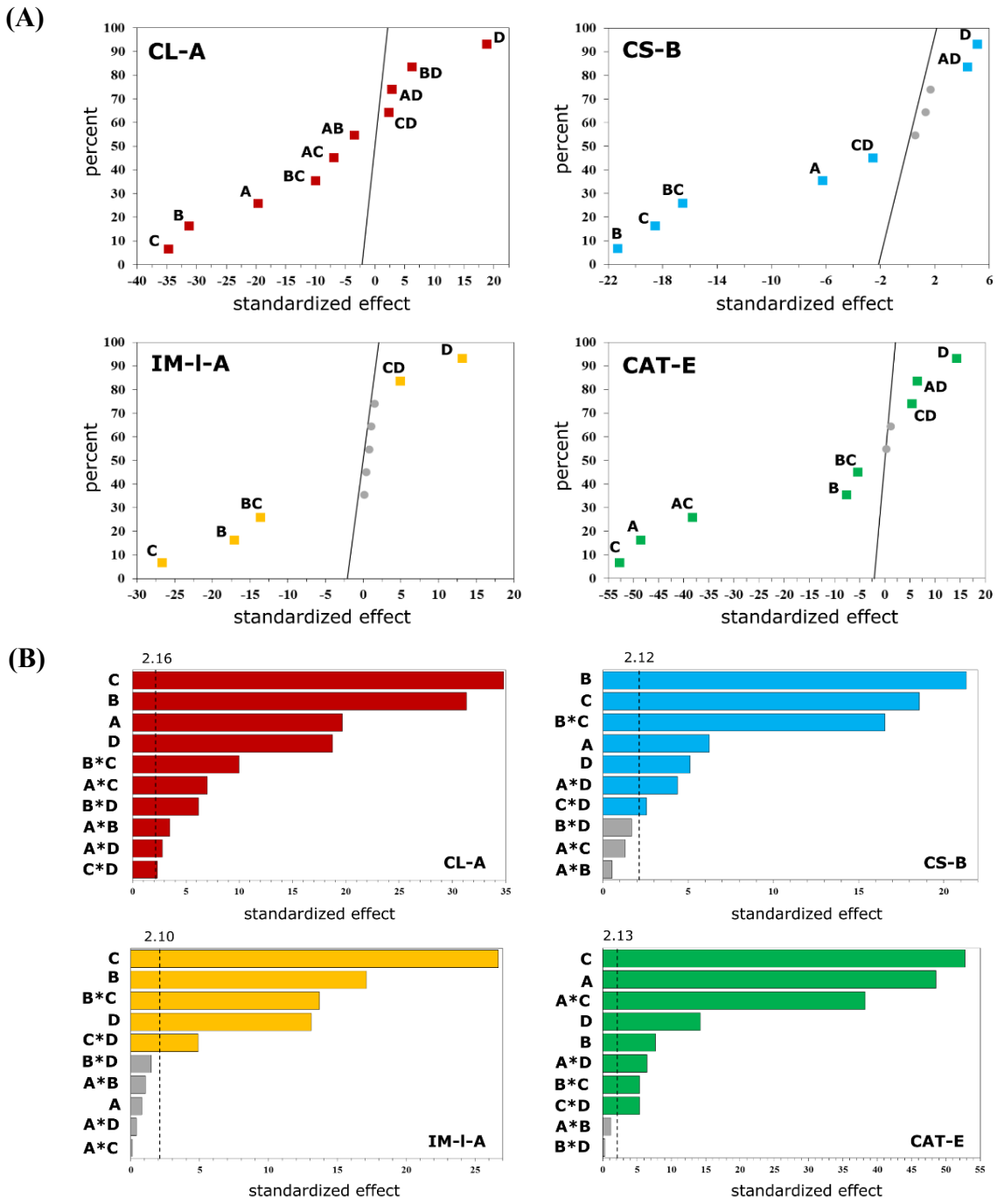

Figure 4.3. (A) Normal probability plot of standardized effect. The colored square means that the parameter has a significant effect and is included in the regression model. The gray circle represents the term that was not statistically significant and was excluded from the regression model. The sign of each parameter determines its direction. A: RH, B: O_3, C: airflow, D: loading. **(B)** Pareto chart of the standardized effect. Bars that cross the reference line (the vertical dashed line) are statistically significant

Based on the calculated p-values (Table 4.3), the following points can be remarked: i) The regression model captures the variation of the media's ozone conversion and the lack of fit of the

model is not statistically significant; ii) the linear effects of the operational parameters, which are RH, O_3 concentration, airflow rate, and loading volume, are significant and correlated with the media performance; iii) the effect of two-way interactions between the parameters are statistically significant and the ones with a p-value<0.05 strongly impact the media performance; iv) for all media at least one parameter has a curved relationship (non-linear relationship) with the performance (p-value of the curvature = 0.00); v) the regression models adequately fit the experimental data for all the material (R^2 >98.78%); and vi) The small difference between R^2, the R^2_{adj}, and the R^2_{pred} for all the regression models indicates that the models do not over-fit the data.

To further analyze these statistical results, it was essential to first classify and then assess the materials based on their ozone removal mechanism. Here along with the statistical analysis, we prepared a reaction-diffusion model of the packed bed reactor (Equation 4.8) and analyzed it against the statistical derivations (see Materials and Methods and Appendix 4.A). In this model, the ozone decomposition reaction rate constant ($k''\,(\frac{m}{s})$) and the activity decay function parameters ($k_d(\frac{1}{s}\,(\frac{m^3}{mol})^{n2}), n_1, and\ n_2$) of each material were determined (Table S4.3) by fitting the model to the experimental data. Broadly, the model approximately fits the experimental data with a considerable difference between the reaction rate constant and activity decay function of ACs and catalyst. This can be attributed to the fundamental difference in the removal mechanism between AC and catalyst, which matches the previous study analyses [162]. AC removes ozone through chemisorption and generates O_2, CO_2, and CO while the catalyst decomposes ozone to oxygen [162]; among the ACs, CS-B has a higher chemisorption capacity than others [162], which is reflected in its higher reaction constant rate (Table S4.3). Besides the fundamental difference in the reaction mechanism, the pore structure of the materials is different as the N_2 adsorption-desorption isotherms of CL-A, CS-B, and IM-l-A are type I and for the CAT-E it is type II [162], and their specific surface area, pore volume, and pore size distribution are substantially different (see Table 4.4 and Figure 4.5). Because of the physicochemical distinctions between ACs and catalyst, herein, the effects of operational parameters are discussed separately.

4.4.2. Detailed analysis of AC-based media

Considering the direct effects of the operational parameters, decreasing the airflow rate has the highest positive effect on AC-based media performance (Figure 4.3). At reduced airflow rates, the overall effectiveness factor (Ω, Equation 4.15) decreases due to the reduction in mass transfer

coefficient (Equation 4.18); however, this effect is countered by the attenuated ozone axial dispersion and convection through the bed (presented by the 1st and 2nd term, respectively, on the right-hand side of Equation 4.8). Also, lower airflow rates reduce the chance of channeling in packed beds (which is not accounted for in the reaction-diffusion equation). The results show latter effects, i.e., lower ozone dispersion and convection and lower airflow channeling, are dominant, leading to the overall improvement of the bed's ozone removal performance.

In relative terms, the airflow rate effect is the smallest on CS-B followed by IM-l-A and CL-A, which can be attributed to the higher importance of the reaction compared to the convection and dispersion. This effect is clearly observed in the difference in the reaction rate constant (*k"*, Table S4.3) and granule size and shape, where CS-B has higher *k"* and smaller granules than CL-A and IM-l-A. This behavior is also consistent with the fact that the airflow rate variation did not affect the activity decay rate of CL-A, while it resulted in changes in the activity decay function of CS-B and IM-l-A (Table S4.3, CL-A: n_1=~2 and n_2=~1.1 for all the airflow rates, IM-l-A: n_2=0, n_1 increased from ~3.3 to ~4.5 from high to low airflow rates, CS-B n_1=~2.1, n_1 varied ~0.5 to ~1 from high to low airflow rates, note that according to Equation 4.9, higher n_1 and n_2 values mean lower deactivation rate). Assessing the two-way interaction highlights that the effect of airflow rate and loading volume interaction on ACs was statistically significant (Table 4.3, Figure 4.3). This interaction had a positive effect on CL-A and IM-l-A which was more pronounced at the lower loading volume while it had a negative impact on CS-B with a stronger correlation at the higher volume (see Figures 4.3 and S4.1 to S4.3). This may be due to the potential channeling effect between ACs since airflow channeling is affected by granule size and shape [175].

Another important parameter affecting the packed bed performance was the inlet ozone concentration, which had a negative effect on all ACs. The inlet ozone concentration directly affects the activity decay function (Equation 4.9), which could reduce the performance through the reaction term (Equation 4.8) and the Ω factor (Equation 4.15). The extent of the effect depends on the material's reaction rate constant and properties (e.g., specific surface area, bulk density, and granule size), which according to the experimental results and the kinetic model was shown to be overall greater on CL-A followed by CS-B and IM-l-A. The statistical analysis of experimental data further detected the most severe effect of inlet ozone concentration at high airflow rate on ACs (Figures S4.1 to S4.3 and Table 4.3). A higher airflow rate means higher ozone dispersion and convection through the bed, and higher inlet ozone concentration translated to a higher

deactivation rate. Thus, increasing both the airflow rate and inlet ozone concentration deteriorated the bed's performance synergistically. This interaction had the strongest effect among all the two-way interactions (Table 4.3, Figure 4.3), with a greater effect on CS-B than IM-l-A and CL-A.

Loading volume had a positive effect on the ACs' performance (Table 4.3, Figure 4.2), caused by decreasing the axial dispersion, increasing the residence time, and reducing the bed porosity. Examining the coded coefficient of this parameter in the regression model indicates that this effect was greatest for CL-A followed by IM-l-A and CS-B. The granules' surface area per unit volume calculations (A, Equation 4.16), which is affected by bed porosity and granule size, showed that doubling the bed volume (from 12.5 mL to 25 mL), enhanced A more noticeably in CL-A (~4.2%) than IM-l-A (~4%) and CS-B (~2.9%). It is worth noting that an association also exists between the ozone concentration and loading volume, which could potentially result from the relative competition between the decomposition reaction and ozone convection (Equation 4.8). This interaction predictably was statistically significant only for CL-A (Figure S4.1) where the negative effect of increasing ozone level at low media loading was higher due to a lower chemisorption capacity and higher ozone convection.

4.4.3. Humidity effect on AC-based media

The humidity seemed to have the most unpredictable effects, and thus deserved a detailed analysis. Based on the results, increasing the humidity level had a negative effect on CL-A and CS-B's ozone removal performance, but it had no effect on IM-l-A (Figure 4.2, and Table 4.3). Previous studies [9], [10] mentioned that humidity could have a dual effect on ACs' ozone removal performance. To further investigate it, extra experiments were carried out whereby all the parameters were kept constant at the center point (305 ppm ozone, 8.5 L/min airflow rate, 18.75 mL media loading), and the relative humidity level was adjusted at 0%, 35%, and 70%. The results (Figure 4.4) confirmed a negative effect on CL-A, while further unveiling a dual strong effect on CS-B and a small positive effect on IM-l-A. This is captured consistently in the deactivation equation of the model by the effect of the kinetic parameters, namely the decay rate constant (k_d) and the decay power (n_1). That is the decay rate constant of CL-A, on one hand, increased at high RH, while remaining constant for CS-B and IM-l-A; on the other hand, the trend for the latter two followed the variation of n_1 (Table S4.3).

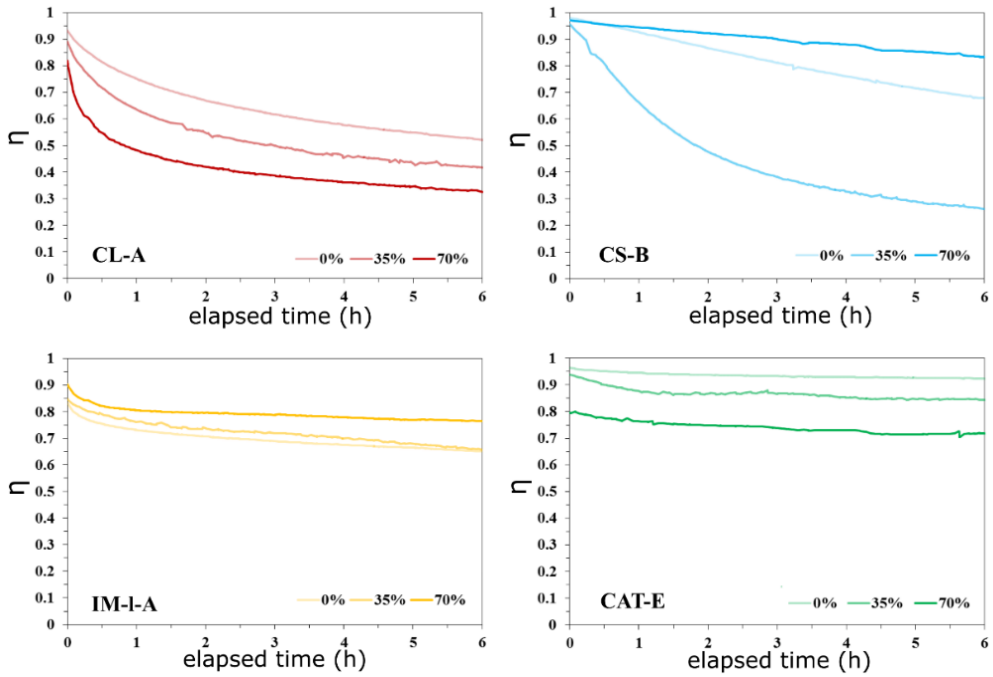

Figure 4.4. The effect of relative humidity on the performance of media. The humidity level increases from light to dark shade of colour. Measured operational conditions are: ozone concentration = 303.2±6.5 ppm; airflow rate = 8.52±0.02 L/min; media loading volume = 18.75 mL; humidity level = <1%; 35.4±1.1%, 70.1±1.2%.

It must be noted, however, that the direct effect of RH and the possible route of ozone reaction with water molecules on the surface of AC were not considered in the kinetic model. Therefore, in some scenarios, the model overestimated the ozone outlet concentration.

The humidity response implies a complex physicochemical interaction among the water, media, and ozone. When the airflow passes through the AC bed the primary sites (surface functional groups such as oxygen-containing ones) and the secondary sites (adsorbed water molecules) adsorb water vapor as a result of hydrogen bonding [176], [177]. In case of a constant flow of water vapor, it could lead to the formation of water clusters on the surface of AC [176], [177] that can contribute to ozone removal. Moreover, ozone is known as an oxidizer whose chemisorption by AC increases the number of oxygen-containing functional groups, which can adsorb water molecules on the AC's surface over time [162]. Drawing on this fundamental mechanism, the effect of humidity on different AC media could be more deeply investigated by assessing their physical and chemical properties.

Table 4.4. Materials properties calculated from N_2 adsorption-desorption isotherm and mercury intrusion porosimetry results.

	CL-A	CS-B	IM-l-A	CAT-E
N_2 adsorption-desorption isotherm				
S_{BET} (m^2/g)	1114.93	1001.4	1143.69	287.69
V_{total} (NLDFT[1]) (cm^3/g) (pore width<387.34 Å)	0.5	0.42	0.53	0.34
Average pore width (Å)	18.65	16.78	19.59	47.23
Mercury intrusion porosimetry				
V_{total} (cm^3/g)	0.47	0.19	0.36	0.31
Average pore width (µm)	2.54	0.59	2.94	0.03
Porosity (%)	27.35	13.89	22.6	46.07
Tortuosity	5.69	4.66	5.93	5.47
Permeability[2] (mD)	1669.52	9677.59	1665.73	3140.38
Conductivity formation factor[3]	0.004	0.025	0.005	0.006

[1] the pore volume was calculated based on the non-local density functional theory (NLDFT) method
[2] The capacity of a material to transmit fluid. The conductance of fluid flow that a porous or fractured medium exhibits.
[3] The ratio of the electrical conductance of a sample permeated with a conductive liquid to the electrical conductance of the liquid

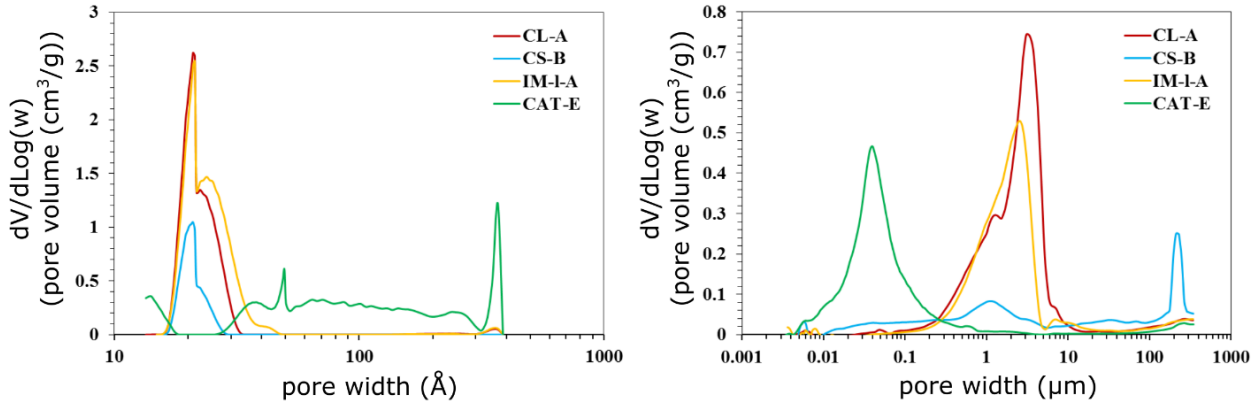

Figure 4.5. Material's pore size distribution. Left: Obtained from N_2 adsorption-desorption isotherm by NLDFT method, and Right: Obtained from mercury intrusion porosimetry.

CL-A has a high specific surface area and pore volume (Table 4.4). The pore size distribution obtained from N_2 adsorption-desorption isotherm and mercury intrusion shows that CL-A pore sizes are in the range of 15 to 30 Å and 0.1 to 10 µm (Figure 4.5), proving a porous structure having micro-, meso-, and macro-pores. It is very likely that water molecules introduced by the airflow condense within the pores due to capillary effects and cover the AC active sites, hindering ozone from reaching the active site and reducing the yield. Another effect to consider is the chemical interaction of adsorbed water molecules with ozone. Previously, we observed CL-A has

a lower chemisorption capacity, hence a lower reaction rate constant, than CS-B; so smaller numbers of oxygen-containing functional groups were formed on its surface during chemisorption, and, in addition, it had a lower number of basic groups (OH^-) than IM-l-A [162]. Therefore, although water molecules themselves could contribute to ozone removal [127], CL-A's adsorption of water vapor, was insufficient to compensate for the deactivated sites.

IM-l-A, albeit having a similar specific surface area, pore volume, and pore size distribution as CL-A (Table 4.4 and Figure 4.5), harbors a higher density of OH^- groups on its surface [162], hence, it could adsorb more water molecules than CL-A. The water clusters formed on OH^- and other oxygen-containing functional groups (formed through chemisorption) could, therefore, contribute to ozone removal and improving the IM-l-A's performance from the RH of 35% to 70%. Across the 0% to 35% RH range, the efficiency enhancement was less than 5%, indicating a potentially lower chance of forming water clusters relative to highly humid conditions. Notably, the model reports a smaller reaction rate constant for IM-l-A compared to CL-A, nevertheless, this may not represent the realistic reaction mechanisms for this material due to overlooking the OH^- surface reaction, which can deviate substantially at high-humidity circumstances.

CS-B has a lower specific surface area, and lower pore volume than CL-A and IM-l-A (Table 4.4), and its pore sizes vary mostly between 15 to 30 Å, 0.4 to 4 μm and 150 to 300 μm (Figure 4.5), thus CS-B has larger pores than CL-A and IM-l-A—the SEM images [162] from the surface of these materials show the macro-pores on CS-B surface. Although CS-B has a lower pore volume than CL-A and IM-l-A, it has a significantly higher conductivity formation factor (which is directly related to porosity) and permeability (Table 4.4). Therefore, it can be inferred that the CS-B's pores better resemble interconnected tunnels. Additionally, CS-B has the highest chemisorption capacity and reaction rate constant among the ACs (Table S4.3) [162]; therefore, it is expected that a higher number of oxygen-containing functional groups form on its surface during the ozone removal process. Consequently, when the RH was elevated to 35%, it is more likely that the water vapour swiftly condenses in the pores due to the capillary effects, impairing the efficiency. At 70% RH, water clusters might form on the secondary adsorption sites and the extra adsorbed water molecules can contribute to ozone removal, outbalancing the inhibiting effect of the covered-active-site. This could justify the enhanced ozone removal performance—even higher than the dry condition.

The effect of RH interaction with other operational parameters in some cases was statistically significant, which is discussed in the following.

- *RH*loading*

The *RH*loading* did not affect IM-l-A, and it had a positive effect on both CL-A and CS-B (Figures 4.3 and S4.1 to S4.3) such that, at low loading volume, (12.5 mL) the effect of humidity was stronger and statistically more significant for CS-B (Table 4.3, see coded coefficients). From the variation of CS-B's data, it is hypothesized that there would be an optimum loading volume and humidity level to maximize the efficiency, which can be investigated in future studies. The distinctly different physical and chemical properties of the AC-based media could underlie the considerable difference between their responses to this confounding relationship, yet further studies are needed to resolve the governing mechanisms.

- *RH*ozone and RH*airflow rate*

Among the AC-based media, the effect of these two-way interactions was negative and statistically significant in the case of CL-A media (Table 4.3, Figure 4.3) which could be more susceptible to water deactivation due to its lower total chemisorption capacity than the other two media. Specifically, the *RH*airflow* factor, which is determined to be stronger interaction, uncovers a stiff collective interaction between the RH and airflow. Further identification of this mechanism demands future experimental and modeling investigations.

4.4.4. Catalyst media

Increasing the airflow rate had the largest negative impact on the ozone removal performance of the CAT-E media (Figures 4.2 and 4.3-B). Comparing the coded coefficients of the parameters for CAT-E (Table 4.3) revealed that the airflow rate, in terms of either direct or two-way interactions, had the largest effect among all the operational parameters. At elevated airflow rates, despite the increase in the mass transfer coefficient and subsequently Ω factor, the ozone axial dispersion, and faster convection through the packed bed (i.e., lower residence time) (Equation 4.8), which have larger numerical values, are the major factors in degrading the bed's performance.

The second important parameter was RH such that humidity, known previously to reduce the catalyst removal efficiency through the occupation of active sites [127], causes a 400-fold rise in decay rate. Interestingly, the RH also appeared in a confounding term with the airflow rate, the most influential two-way interaction among all. While RH's effect proved to be negligible at a low

airflow rate (2 L/min), it becomes prominent at higher inflows (15 L/min) (Figure S4.4). At high airflow rates, the mass transfer coefficient of water molecules increases, which could make the competition between water molecules and ozone for active sites more intense leading to the escalated effect of RH at elevated air flows.

The loading volume has a slightly favorable effect, which was the lowest term compared with all the AC media, caused by a decrease in the axial dispersion. This could be related to the porosity that, unlike ACs, by expanding the bed volume from 12.5 mL to 25 mL has remained constant. The loading volume interacted with both RH level and airflow rate (Table 4.3, Figure 4.3). These interactions had a positive effect on ozone elimination, highlighting that the detrimental effect of RH level or airflow rate was abated by incorporating a larger amount of loading material (Figure S4.4). A possible explanation for this observation is that, with more media loading, the channeling effect resulting from a high airflow rate might be weaker [175], lessening its negative effect.

Lastly, increasing the ozone level slightly decreased the efficiency of the media—the effect of ozone exposure on CAT-E was significantly weaker than the AC-based media [162]. CAT-E has the highest reaction rate constant among all the media and n_2=0 in the activity decay function, meaning that the deactivation is independent of the inlet ozone abundance. CAT-E media as a manganese oxide-cuprous oxide-based catalyst designed for ozone removal; has a high density of stable active sites (i.e., oxygen vacancies) [162]. Such functionality can arguably make the media resilient to ozone concentration, particularly at low airflow rates (Figure S4.4) where the ozone influx is less, and the residence time is higher. Comparing the coded coefficient (Table 4.3) of *the O_3*airflow rate* for each material revealed that it had a more pronounced impact on ACs (CS-B > CL-A, IM-l-A > CAT-E), which is in alignment with the degradation of their material structure and dependence of deactivation on ozone concentration, in the chemisorption in contrast to catalytic decomposition.

4.5. Limitations

The incorporation of statistical and kinetic model analyses elucidates how operational parameters affect the ozone removal performance of granular media. However, both regression and kinetic models that were proposed in this study have limitations.

- The regression model is based on fractional factorial design outcomes. Although the design was de-aliased and center points were added, a factorial design does not consider the non-linear effect of parameters in the regression model.
- In the kinetic model, chemisorption and catalytic reactions were integrated in one term despite the fact that their decay rate could be different. Also, the ozone reaction with OH groups was not considered in the model. The mass transfer was considered one dimensional and the radial mass transfer and dispersion was excluded based on the assumption that the ozone concentration in radial direction is uniform.

4.6. Conclusion

The ozone removal performance of granular media could vary over a wide range depending on the operational conditions. Herein it was demonstrated that, due to differences in chemical and physical properties of granular materials, each ozone removal technology performs uniquely. Important correlational relationships between operational parameters and ozone removal efficiency were found via statistical and kinetic modeling analyses. These methods revealed that the airflow rate and ozone level were the most influential parameters for ACs whereas the effect of humidity was the most significant one on the catalyst's performance. The effect of humidity was, in fact, one of the most complex effects owing to the sophisticated chemical and physical interactions of water with the materials' surface. Increasing the humidity level from 0% to 70% had a negative effect on the removal performance of CL-A, a dual effect on CS-B (first negative up to 35% and then positive until 70%), no effect on IM-l-A, and a negative effect on CAT-E. Furthermore, the statistical analysis showed that the impact of two-way interactions of parameters could be statistically significant, namely, the most important ones were found to be O_3**airflow* on ACs and *RH*airflow* on CAT-E. At low airflow rates, CS-B and IM-l-A were indifferent to ozone, and humidity had no effect on CAT-E, while at high airflow rates the impacts were considerable.

The results from statistical analyses have important implications for media selection for various applications. Among ACs, the ozone removal efficiency of CS-B, despite having the highest chemisorption capacity, experienced the most dramatic vulnerability to the change of the operational parameters (its center point had the largest deviation from the corners), while IM-l-A,

having OH^- groups on its surface, experienced the least. Therefore, according to these findings, CL-A is not recommended for extensive ozone elimination, particularly for indoor air quality applications, while IM-l-A could be drawn upon as a reliable ozone removal media. For industrial applications, at elevated ozone concentrations, catalyst could be the best candidate—comparing the ACs with the catalyst revealed that, on average, catalyst is the most efficient ozone removal media. The main limitation of the study is its inability to consider the non-linearity of the operational variables in the regression model. However, the broad insights gained here can fuel complementary studies for each material in the future.

4.7. Appendix 4.A

The axial dispersion coefficient, D_a, is estimated by the correlation proposed by Wakao and Funaskri [178] for packed beds where mass transfer is taking place between the fluid and the granules' surface and the Re number is between 3 to 10000:

$$\frac{D_a \varepsilon_b}{D_m} = 20 + 0.5\, Re\, Sc \tag{4.12}$$

$$Re = \frac{d_s\, u}{\nu\,(1-\varepsilon_b)} \tag{4.13}$$

$$Sc = \frac{\nu}{D_m} \tag{4.14}$$

where ε_b is the bed porosity, d_s *(m)* is the granule spherical equivalent diameter, *u(m/s)* is the face velocity, *Re* is the Reynolds number, *Sc* is the Schmidt number, ν *(m^2/s)* is the kinematic viscosity, and D_m *(m^2/s)* is the molecular diffusivity.

The overall effectiveness factor, Ω, was calculated according to the following equation [172]:

$$\Omega = \frac{actual\ overall\ rate\ of\ reaction}{reaction\ rate\ if\ the\ entire\ surface\ was\ exposed\ to\ the\ bulk\ concentration}$$

$$= \frac{\omega}{1 + \frac{\omega\, k''\, \rho_b\, S\, a}{K\, A}} \tag{4.15}$$

$$A = 6\frac{1-\varepsilon_b}{d_s} \tag{4.16}$$

$$d_s = \frac{3}{{}^{2}/_{d} + {}^{1}/_{l}} \tag{4.17}$$

$$\frac{K\, d_s}{D_m} = \frac{1-\varepsilon_b}{\varepsilon_b}\, Sh \tag{4.18}$$

$$Sh = 2 + 1.1\, Re^{{}^{3}/_{5}}\, Sc^{{}^{1}/_{3}} \tag{4.19}$$

where ω is the internal effectiveness factor, $k''(\frac{m}{s})$ is the reaction rate constant, $\rho_b(\frac{g}{m^3})$ is the material's bulk density, S $(\frac{m^2}{g})$ is the specific surface area, a is the activity, *K (m/s)* is the mass transfer coefficient, *A* (m^2/m^3) is the surface area per unit volume, ε_b is the bed porosity, d_s *(m)* is the granule spherical equivalent diameter, *d (m)* is the granule diameter, *l (m)* is the granule height, and *Sh* is the Sherwood number, which is calculated based on the correlation proposed by Wakao and Funaskri [178] for packed beds when Re number is between 3 to 10000.

The internal effectiveness, ω, is calculated based on the following equation [172]:

$$\omega = \frac{actual\ overall\ rate\ of\ reaction}{reaction\ rate\ if\ the\ entire\ interior\ surface\ was\ exposed\ to\ the\ granule's\ surface\ concentration} = \frac{3}{\varphi}\left(\frac{1}{\tanh\varphi} - \frac{1}{\varphi}\right) \quad (4.20)$$

$$\varphi = \frac{d_s}{2}\sqrt{\frac{k''\,\rho_p\,S\,a}{D_{eff}}} \quad (4.21)$$

$$D_{eff} = \frac{\varepsilon_p/\tau}{1/D_K + 1/D_m} \quad (4.22)$$

$$D_K = \frac{d}{3}\sqrt{\frac{8\,R\,T}{\pi\,M}} \quad (4.23)$$

where, φ is the Thiele modulus, d_s *(m)* is the granule spherical equivalent diameter, $k''(\frac{m}{s})$ is the reaction rate constant, ρ_p $(\frac{g}{m^3})$ is the material's apparent density, S $(\frac{m^2}{g})$ is the specific surface area, a is the activity, D_{eff} *(m²/s)* is the effective diffusivity, D_K *(m²/s)* is Knudsen diffusion coefficient, D_m *(m²/s)* is the molecular diffusivity of ozone in the air, ε_p is the granule porosity, τ is the granule tortuosity, *R (g m/s²mol K)* is the global gas constant, *T (K)* is the temperature, and *M (g/mol)* is the molecular weight.

4.8. Supporting Information

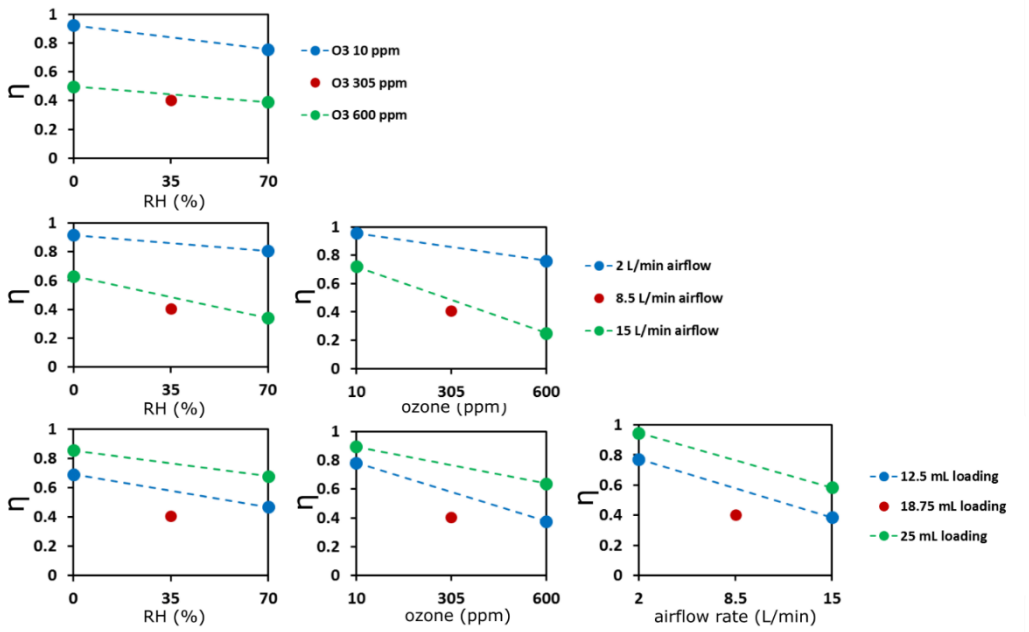

Figure S 4.1. Two-way interactions' effect on the ozone removal performance of the CL-A. Parallel lines means the effect is insignificant. The red circle shows the center point. Each point is the average of the responses at the related conditions given by the regression model (Table 4.6)

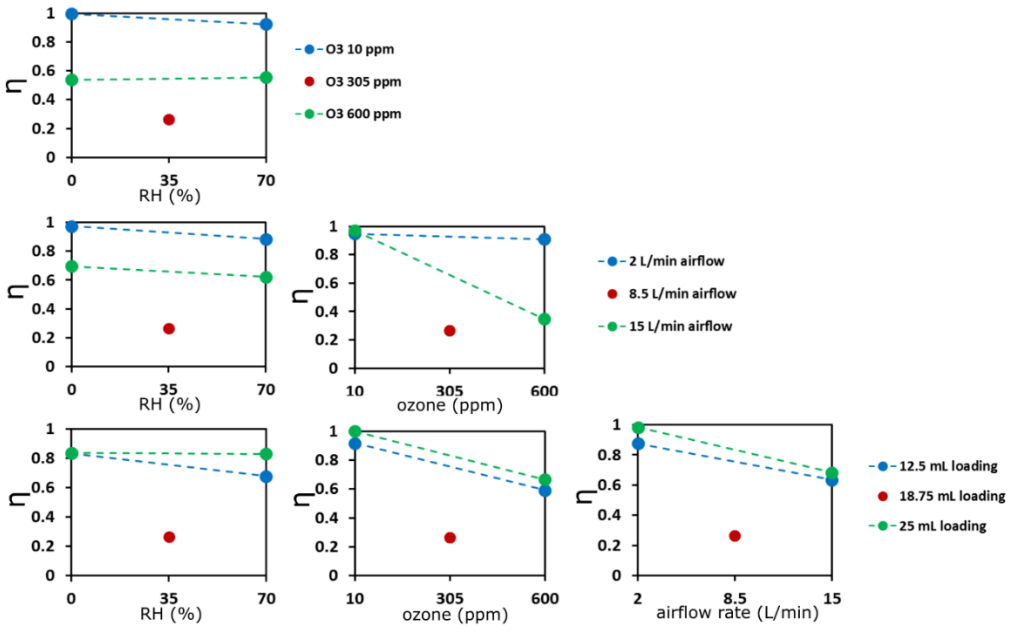

Figure S 4.2. Two-way interactions' effect on the ozone removal performance of the CS-B. Parallel lines means the effect is insignificant. The red circle shows the center point. Each point is the average of the responses at the related conditions given by the regression model (Table 4.6)

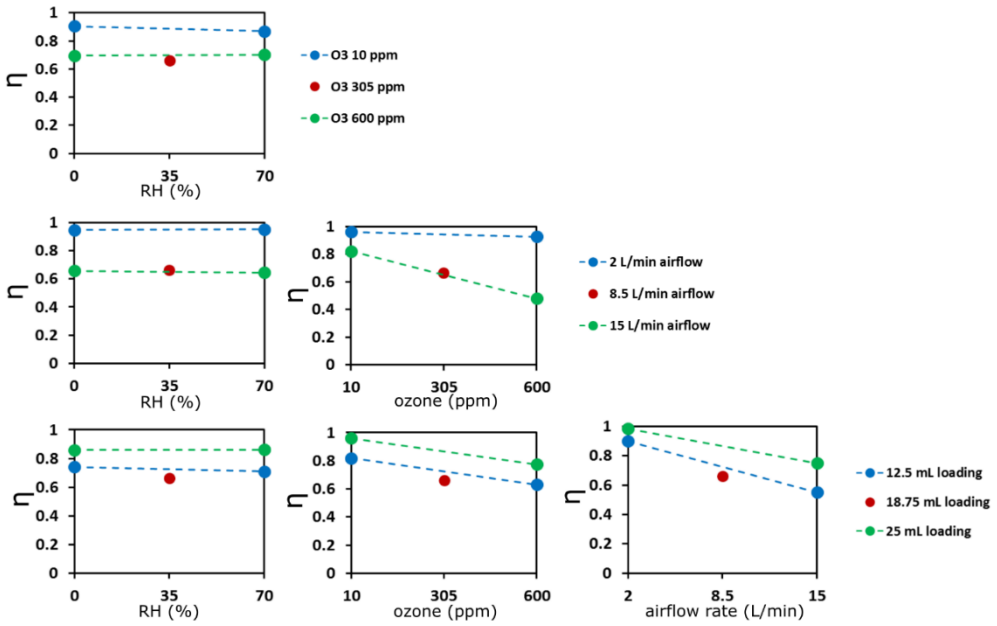

Figure S 4.3. Two-way interactions' effect on the ozone removal performance of the IM-l-A. Parallel lines means the effect is insignificant. The red circle shows the center point. Each point is the average of the responses at the related conditions given by the regression model (Table 4.6)

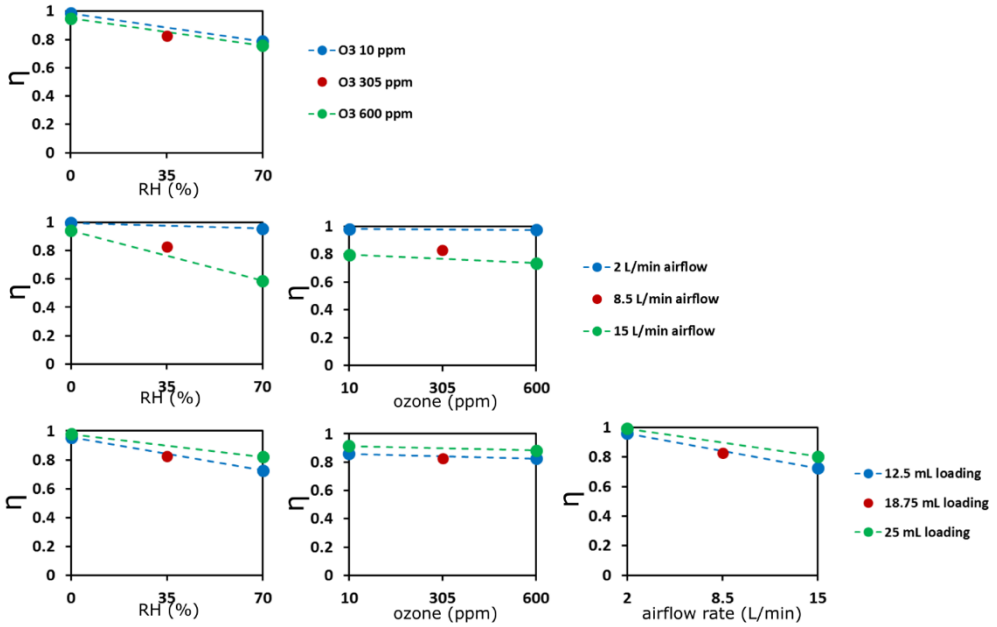

Figure S 4.4. Two-way interactions' effect on the ozone removal performance of the CAT-E. Parallel lines means the effect is insignificant. The red circle shows the center point. Each point is the average of the responses at the related conditions given by the regression model (Table 4.6)

Table S 4.1. Operational condition

conditions given by the software				measured operational conditions				
Humidity level (%)	**Ozone (ppm)**	**Airflow rate (L/min)**	**Media loading (mL)**	**Humidity level (%)**	**Ozone (ppm)**	**Airflow rate (L/min)**	**Media Loading**	**Temperature (˚C)**
0	10	2	12.5	<1	10±0.4	2.03±0.03	12.5	18.8±0.1
70	10	2	25	70.3±0.6	10.1±0.6	2.01±0.01	25	19.5±0.1
0	600	2	25	<1	598.6±8.9	2.02±0.01	25	19.07±0.1
70	600	2	12.5	71.2±2.1	601±7.2	2.04±0.01	12.5	19.5±0.2
0	10	15	25	<1	10.1±0.2	15±0.01	25	19.5±1.3
70	10	15	12.5	69.7±2.9	10.5±1.1	15.06±0.04	12.5	18.9±0.2
0	600	15	12.5	<1	601.1±7.1	15.04±0.02	12.5	19.4±0.1
70	600	15	25	69.8±2.5	599.3±9.1	15.01±0.02	25	20.1±0.2
0	10	2	12.5	<1	10.6±0.3	2.01±0.02	12.5	18.8±0.2
70	10	2	25	70.1±0.9	10.3±0.5	2.01±0.01	25	18.5±0.2
0	600	2	25	<1	590.6±7.3	2.03±0.02	25	18.6±0.1
70	600	2	12.5	70.5±3.1	599.6±8.1	2.1±0.03	12.5	18.8±0.1
0	10	15	25	<1	10.4±0.4	15.02±0.04	25	18.4±0.3
70	10	15	12.5	70.7±2.2	10.4±0.9	15.05±0.02	12.5	18.5±1.5
0	600	15	12.5	<1	600.2±4.5	15.02±0.04	12.5	19.2±0.2
70	600	15	25	71.7±3.3	597.4±9.4	15.02±0.02	25	18.8±0.1
35	305	8.5	18.75	35.3±0.4	305.6±5.5	8.51±0.01	18.75	19.5±0.2
35	305	8.5	18.75	35.9±1.8	304.9±6	8.53±0.02	18.75	19.1±0.1
35	305	8.5	18.75	34.9±1.3	300.7±6	8.52±0.01	18.75	18.8±0.2

Table S 4.2. Ozone removal performance of different media after 6 h exposure to ozone at the given operational conditions by the experimental design.

Humidity level (%)	**Ozone (ppm)**	**Airflow rate (L/min)**	**Media loading (mL)**	**η**			
				CL-A	**IM-l-A**	**CS-B**	**CAT-E**
0	10	2	12.5	0.969	0.938	1	0.999
70	10	2	25	0.988	0.988	0.999	0.998
0	600	2	25	0.959	0.978	0.999	0.999
70	600	2	12.5	0.473	0.867	0.824	0.923
0	10	15	25	0.911	0.922	0.996	0.995
70	10	15	12.5	0.507	0.729	0.890	0.559
0	600	15	12.5	0.242	0.389	0.403	0.881
70	600	15	25	0.209	0.618	0.398	0.603
0	10	2	12.5	0.969	0.938	1	0.999
70	10	2	25	0.992	0.996	0.999	0.999

0	600	2	25	0.961	0.985	0.999	0.999
70	600	2	12.5	0.560	0.875	0.704	0.916
0	10	15	25	0.918	0.929	0.998	0.992
70	10	15	12.5	0.458	0.701	0.899	0.571
0	600	15	12.5	0.252	0.388	0.401	0.892
70	600	15	25	0.200	0.529	0.349	0.628
35	305	8.5	18.75	0.403	0.689	0.252	0.821
35	305	8.5	18.75	0.393	0.657	0.263	0.843
35	305	8.5	18.75	0.417	0.637	0.282	0.814

Table S 4.3. Kinetic parameters of each material obtained after curve fitting the kinetic model with the experimental data.

Standard order	CL-A				CS-B				IM-l-A				CAT-E			
	k	k_d	n_1	n_2	k	k_d	n_1	n_2	k	k_d	n_1	n_2	k	k_d	n_1	n_2
1	0.05	0.08	1.96	1.15	0.63	0.87	2.40	1.10	0.0012	0.1	4.80	0	1	0.01	2.75	0
2	0.05	2.84	2.42	1.10	0.63	0.87	2.23	1	0.0012	0.1	4.50	0	1	4	2.85	0
3	0.05	0.08	2.15	1.10	0.63	0.87	2.66	1	0.0012	0.1	5.19	0	1	0.01	2.27	0
4	0.05	2.83	2.43	1.10	0.63	0.87	2.04	1	0.0012	0.1	3.35	0	1	4	2.26	0
5	0.05	0.08	1.66	1.11	0.63	0.87	2.22	0.52	0.0012	0.1	3.42	0	1	0.01	2.35	0
6	0.05	2.83	2.18	1.07	0.83	0.87	2.19	0.49	0.0012	0.1	5.50	0	1	4	2.85	0
7	0.05	0.08	1.96	1.10	0.63	0.87	1.91	0.53	0.0012	0.1	2.31	0	1	0.01	2.40	0
8	0.05	2.85	2.12	1.5	0.63	0.87	1.72	0.59	0.0012	0.1	2.02	0	1	4	1.93	0
Cnt [a]	0.05	2.83	2.15	1.18	0.63	0.87	1.67	0.58	0.0012	0.1	2.36	0	1	0.5	2.12	0
Cnt L [b]	0.05	0.08	1.87	1.10	0.63	0.87	1.82	0.58	0.0012	0.1	2.25	0	1	0.01	1.80	0
Cnt H [c]	0.05	2.85	2.1	1.10	0.63	0.87	1.93	0.57	0.0012	0.1	2.60	0	1	4	2.20	0

[a] center point
[b] center point, low humidity level
[c] center point high humidity level

Chapter 5. Synthesis and physicochemical modification of an MnO_x-based catalyst for enhanced ozone decomposition in humid conditions

5.1. Abstract

Ozone is a hazardous air pollutant with many adverse effects on human health and the environment. As the application of ozone in industry is growing, it becomes increasingly important to implement appropriate ozone removal systems to mitigate these effects. MnOx-based catalysts hold immense promise for ozone decomposition; however, a major challenge in their application is deactivation by water molecules, especially at high humidity levels. This study seeks to address this limitation by investigating physicochemical modifications through synthesis using solid interface reaction and co-precipitation methods. The developed catalysts were tested in a bench-scale removal setup and characterized using various techniques, including X-ray diffraction crystallography, X-ray photoelectron spectroscopy, scanning electron microscopy, transmission electron microscopy, and N2 adsorption-desorption. Additionally, the properties of the catalysts were studied performing density functional theory (DFT) calculations. It was determined that MnOx-based catalysts made via a solid interface reaction method offer the highest efficiency. Further catalyst modification by doping with transition metals such as silver and cerium enhanced the physicochemical properties of the catalysts. Ce-doped catalyst (molar ratio $\frac{Ce^{3+}}{Mn^{2+}} = 0.1$) feature a large surface area via flower-like hollow spherical structures and high density of oxygen vacancies. Also, DFT calculations showed that the energy gap between the frontier orbitals of the Ce-doped catalyst and the O_2^{2-} intermediate was the lowest. Ce(0.1)Mn-S catalyst achieved the highest efficiency (47.5%), 1.6 times higher than the undoped one, at 80% RH level and 10 ppm ozone, 1 h post-exposure. The catalyst, however, experienced efficiency loss due to humidity during prolonged exposures (after 6h the efficiency decreased to 22%). To prevent this, a novel modification technique was employed involving the mixing of poly(vinylidene fluoride) particles, a hydrophobic ozone compatible polymer, with catalytic media. This modification boosted the performance dramatically to 91.5% efficiency, 1 h post-exposure, and 50%, 6 h post-exposure, at the above-mentioned conditions. It is expected that the proposed hybrid media will be of significant utility in numerous ozone removal systems.

5.2. Introduction

Ozone is an oxidizing compound with a growing range of applications in industry; it is, however, harmful to human health and the environment [46], [150], [179], [180]. To protect the occupants' health and safety and the environment, its concentration should be kept below a specific limit, both indoors and outdoors [181], [182]. The permissible exposure limits are determined by regulatory bodies such as occupational safety and health administration (OSHA) and world health organization (WHO) [127], [183]. Accordingly, increasing ozone utilization in industry is followed by rising demands for efficient, robust, and economical ozone removal technologies [184]. Activated carbon-based materials and catalysts were investigated and suggested for ozone removal [162], [185], [186]. Among these, Manganese oxides (MnO_x) have garnered significant attention because not only are they earth-abundant, inexpensive, and non-toxic, but also, they have high catalytic activity [18], [86], [151].

Manganese (Mn) is a transition metal that forms oxides with variable oxidation states (from +2 to +7), giving it catalytic properties [85]. Owing to the Mn's capability in possessing various oxidation states, a stable manganese oxide (MnO_x) catalyst could perform either as a reducing agent or oxidizing agent [62], [85], [187]. The presence of different oxidation states results in the formation of oxygen vacancies that act as the catalyst's active sites for ozone decomposition [31]. At dry conditions, MnO_x-based catalysts convert ozone to oxygen efficiently; however, at humid conditions, the efficiency reduces as water molecules compete with ozone to reach the active sites [30], [185]. Furthermore, as a result of the ozone reaction with active sites, peroxide intermediates form on the oxygen vacancies [30], [39], [62]. These intermediates can be transferred into the lattice structure, causing catalyst deactivation [63], [188]. Therefore, it is of significant interest to create durable active sites that are humidity-resistant and able to easily decompose intermediates.

To increase the robustness and effectiveness of MnO_x-based catalysts, researchers have attempted to strengthen the oxygen vacancies and optimize the average Mn oxidation state (AOS) in addition to improving the other physicochemical properties of the material such as specific surface area, crystal structure, and morphology [127], [189]. Studies showed that synthesizing procedure substantially affects the catalyst's properties [91], [96]. MnO_x-based catalysts synthesizing methods include co-precipitation, hydrothermal, sol-gel, and solid interface reaction (SIR) [151], [190]. By changing the Mn precursors [32], [191] and controlling the synthesizing condition (e.g., temperature and pH) [37], [97], [115] catalysts with different properties will be

formed. Also, several modification techniques including metal doping [189], coating [39], [111], [113], acid/base treatment [29], [95], and heat treatment [30] were introduced to fine-tune the catalyst characteristics. Each of these modifications have several effects including reducing the AOS of Mn, enhancing the specific surface area, improving the dispersion of oxygen vacancies, increasing the oxygen vacancy density, strengthen the catalyst reducibility, and facilitate the diffusion of ozone into the catalyst structure.

Doping, one of the most common modification techniques, could increase the density of surface oxygen vacancies, and change the crystallinity [189]. Decreasing crystallinity results in more surface defects and a higher specific surface area, which have positive effects on catalytic activity [35], [40], [101]. In addition, doping can create a mixture of different crystals, and change the morphology of the catalyst particles. The physical and chemical properties of the dopant are important and determine the nature of the change [35], [40], [105], [189]. Several transition metals, including Fe, Co, Ce, W, V, and noble metals such as Ag and Pd, have been used as dopants [189]. Among the transition metals, cerium (Ce) has been highlighted as a greatly effective dopant: it is able to change the crystal structure and morphology, the specific surface area, the density of oxygen vacancies, and oxygen vacancy recovery [25], [35], [40], [66], [107], [114], [115], [118], [119]. Among noble-metal dopants, silver (Ag) causes improvements in the catalytic activity by increasing the reducibility of the catalyst [120]. Additionally, doping a transition metal oxide with a lanthanide, such as lanthanum (La), forms a perovskite-type mixed oxide, which shows durability at high relative humidity [192].

Whereas the aforementioned modification techniques improve the MnO_x-based catalyst ozone decomposition performance; the catalysts have been unable to maintain their high efficiency at high humidity levels. This is because, although the increase in oxygen vacancies improves the catalyst's performance at low-humidity settings, it also renders the surface more hydrophilic, causing higher water absorption and catalyst deactivation. To address this challenge, this study explored physicochemical modifications to elevate the MnO_x catalyst's resistance against humidity. The SIR method was selected as the main synthesis procedure because of its feasibility to produce polycrystalline materials with high-throughput and its capability for large-scale production. An enhanced MnO_x-based catalyst was synthesized *via* chemical modification techniques, including doping with Ce, and Ag. To reduce the adverse effect of humidity, a novel technique was employed where catalysts were physically mixed with a polymer powder to change

the hydrophilicity of the media. The catalysts were coated on a nickel-foam filter to be evaluated in a flow-through bench-scale test set-up. It was found that the hybrid modifications improve the catalyst's performance *via* multiple mechanisms including enhancing the density of oxygen vacancy and repelling water molecules from the catalytic media. Furthermore, the structural stability, thermochemical properties, and the frontier orbitals' energy of the catalysts were investigated by conducting density functional theory (DFT) calculations.

5.3. Methodology

5.3.1. Catalyst synthesis

Two feasible preparation methods were chosen based on the literature: co-precipitation and SIR. Manganese sulfate monohydrate ($MnSO_4.H_2O$, Fisher Chemical) was used as the precursor, and potassium persulfate ($K_2S_2O_8$, Thermo-Scientific), or potassium permanganate ($KMnO_4$, Sigma-Aldrich) was used as the oxidizing agent.

The first type of catalyst, denoted as Mn-P-a, was synthesized by dissolving the same molar amounts of $MnSO_4.H_2O$ and $K_2S_2O_8$ in de-ionized (DI) water separately. After two homogeneous solutions were obtained, the latter solution was added to the first solution dropwise. The mixture's pH was decreased to 1 by adding sulfuric acid (H_2SO_4, Fisher Chemical). Silver nitrate ($AgNO_3$, Fisher Chemical) was added as a catalyst for the reaction (molar ratio of $AgNO_3$ to $MnSO_4.H_2O$ was 0.025), and it was stirred vigorously at 40 ℃ for 24 h. The precipitate was washed with DI water several times and dried in an oven at 180 ℃ for 6 h.

The second type of catalyst, denoted as Mn-P-b, was synthesized by dissolving $MnSO_4.H_2O$ and $KMnO_4$ separately in DI water with molar ratio of $\frac{Mn^{2+}}{Mn^{7+}} = 1.5$. After homogeneous solutions were obtained, the latter solution was added dropwise to the first one. The mixture was stirred at high speed at room temperature for 24 h. The precipitate was washed several times with DI water and dried in an oven at 180 ℃ for 6 h.

The last type of catalyst was synthesized *via* SIR method (Mn-S) where $MnSO_4.H_2O$ and $KMnO_4$ with molar ratio of $\frac{Mn^{2+}}{Mn^{7+}} = 1.5$ were fully grounded by a pestle in a mortar for 30 min. The obtained solid was washed several times with DI water and dried in an oven at 180 ℃ for 6 h. To dope the catalyst with a transition metal, the desired amount of the dopant's precursor (silver nitrate ($AgNO_3$, Fisher Chemical), cerium(III) nitrate hexahydrate ($Ce(NO_3)_3.6H_2O$, Thermo-Scientific), and lanthanum(III) nitrate hexahydrate ($La(NO_3)_3.6H_2O$, Thermo-Scientific)) was

grounded in the mortar with the mixture of reactants The molar ratio of the dopant to the Mn was determined according to the literature—two levels for each: $\frac{Ag^+}{Mn^{2+}} = 0.06, 0.1$; $\frac{Ce^{3+}}{Mn^{2+}} = 0.1, 0.17$; $\frac{La^{3+}}{Mn^{2+}} = 1, 1.67$. The doped catalyst was named M(x)Mn-S, where S refers to the SIR synthesis procedure, M refers to the transition metal, and x refers to the molar ratio of the transition metal ion to the Mn^{2+}. The catalysts' notations are explained in Table 5.1.

Table 5.1. Description of the lab-made catalysts' notations

	Synthesis method	Reactants	Dopant molar ratio	PVDF-to-catalyst mass ratio
Mn-P-a	co-precipitation	$MnSO_4.H_2O$ $K_2S_2O_8$	N/A	N/A
Mn-P-b	co-precipitation	$MnSO_4.H_2O$ $KMnO_4$	N/A	N/A
Mn-S	SIR	$MnSO_4.H_2O$ $KMnO_4$	N/A	N/A
Mn-S-0.2			N/A	0.2
Mn-S-0.4			N/A	0.4
Ag(0.06)Mn-S	SIR	$MnSO_4.H_2O$ $KMnO_4$ $AgNO_3$	$\frac{Ag^+}{Mn^{2+}} = 0.06$	N/A
Ag(0.1)Mn-S			$\frac{Ag^+}{Mn^{2+}} = 0.1$	N/A
Ce(0.1)Mn-S	SIR	$MnSO_4.H_2O$ $KMnO_4$ $Ce(NO_3)_3.6H_2O$	$\frac{Ce^{3+}}{Mn^{2+}} = 0.1$	N/A
Ce(0.1)Mn-S-0.2			$\frac{Ce^{3+}}{Mn^{2+}} = 0.1$	0.2
Ce(0.17)Mn-S			$\frac{Ce^{3+}}{Mn^{2+}} = 0.17$	N/A
La(1)Mn-S	SIR	$MnSO_4.H_2O$ $KMnO_4$ $La(NO_3)_3.6H_2O$	$\frac{La^{3+}}{Mn^{2+}} = 1$	N/A
La(1.67)Mn-S			$\frac{La^{3+}}{Mn^{2+}} = 1.67$	N/A

5.3.2. Coating the catalyst on nickel foam filter

The prepared catalysts, unmodified and metal doped, were coated on a nickel foam filter (Shanghai Tankii Alloy Material Co.) to be assessed in a bench-scale test set-up. To create coatings, the sample was first sieved using a 60 mesh (~250 μm) and then added to a mixture of ethanol and DI water (2:1 v/v) to prepare a 1 wt.% suspension. The mixture was stirred for 12 h using a magnetic stirrer followed by sonication for 1 h in an ultrasonic bath to reach a well-dispersed suspension. Next, the catalyst ink was uniformly drop casted on one side of a 10×15 cm pre-washed Ni-foam filter and dried in an oven at 80 ℃ for 1 h. The drop casting was repeated for the other

side of the filter and the final filter was dried in the oven at 80 ℃ overnight to evaporate water and ethanol from the filter. The filter's mass was measured before and after coating to calculate the mass of catalyst per surface area of the filter.

Physical modification of the catalyst media was performed by adding of poly(vinylidene fluoride (PVDF, Thermo-Scientific) as a hydrophobic polymer to the catalytic media. For this purpose, PVDF suspensions in the catalyst ink were prepared at the PVDF-to-catalyst mass ratios of 0.2 and 0.4. Tween 20 (Fisher Chemical) was added as the surfactant to the mixture to enable the dispersion of the hydrophobic PVDF in the water-ethanol solution. The mixture was stirred overnight and then sonicated for 1 h in an ultrasonic bath. The drop casting was performed similar to the procedure used for previous filters and the filter's mass was measured before and after casting.

5.3.3. Characterization

The particle size distribution (PSD) in the suspensions was studied by a laser scattering particle size distribution analyzer (Partica LA-950V2, Horiba Scientific). X-ray diffraction (XRD, Bruker, D8 advance) was used to identify the crystal phase of synthesized catalysts. Scanning electron microscopy (SEM, FEI ESEM Quanta 450 FEG) was used to observe the morphology of catalysts in addition to the deposition state of the media on the Ni-foam filter at the microscale. ImageJ (National Institute of Health) was used to measure the particle size from SEM images. Transmission electron microscopy (TEM, Thermo Scientific Talos F200X G2) was deployed to further analyze the crystal structure and shape at the nanoscale and to map the elemental composition.

Nitrogen adsorption-desorption was measured by a surface area and porosity analyzer apparatus (MicroActive TriStar II Plus, Micromeritics). The specific surface area of the sample was calculated according to the Brunauer-Emmet-Teller theory (S_{BET}) using the adsorption data [138]. Additionally, the t-plot method was used to calculate the micropore surface area (S_{mic}), the micropore volume (V_{mic}) and the total volume (V_{tot}), where the thickness of the adsorbed layer was calculated by Harkins and Jura equation [139]. Also, the pore size distribution was determined based on the Barret-Joyner-Halenda (BJH) approach using the nitrogen adsorption-desorption isotherm [193]. Before performing the nitrogen adsorption analysis, samples were dried at 50 ℃ for one week.

The surface chemistry including the elemental composition and Mn average oxidation state were analyzed by doing X-ray photoelectron spectroscopy by a K-α instrument (Thermo Scientific) using an Al-Kα radiation source (spot size: 400 μm). Three points were analyzed for each sample; the survey scan was performed by a 200-eV pass energy with 1 eV step size to study the surface elemental composition. The high-resolution scans were recorded by a 50-eV pass energy with 0.1 eV step size. The high-resolution scans were deconvoluted to their constituent peaks. The samples were completely dried before running the test.

5.3.4. Computational details

Several software packages are used for performing DFT calculations in computational chemistry, such as ORCA, VASP, and Gaussian, offering a wide range of quantum chemistry methods. ORCA is known for its efficiency, accuracy, and scalability. Additionally, it supports parallel computing, which facilitates studying large complex systems and accelerates computational chemistry simulations, including DFT calculations [194].

In this study, the structural optimization, frequency calculations, and DFT calculations were performed using ORCA 5.0.3 software, an ab initio quantum chemistry package [194], [195], on the Expanse supercomputer network (total of 345215 core-hour). Perdew-Burke-Ernzerhof (PBE) functional [196] was used. For oxygen and potassium DF2-SVP basis set [197], [198] was selected and for manganese, silver, and cerium Stuttgart-Dresden (SDD) effective core potential (ECP) was employed [199]–[201]Further details are explained in the supporting information.

After conducting the theoretical computations, the length of the Mn-O bond, frontier orbital energies (highest occupied molecular orbital: HOMO, lowest unoccupied molecular orbital: LUMO), and thermochemical properties were calculated. Furthermore, DFT calculations of O_2^{2-} intermediate was conducted to calculate the LUMO energy of the O_2^{2-}, enabling the determination of the HOMO-LUMO gap between the synthesized catalysts and the O_2^{2-} intermediate.

5.3.5. Catalyst activity

The activity of synthesized catalysts for ozone decomposition was evaluated in a continuous bench-scale experimental set-up, illustrated in Figure 5.1, at room temperature (20 °C). The compressed air was used as the carrier gas, and a mass flow controller set the airflow rate at 5 L/min (GHSV=~27000 $^{1}/_{h^{-1}}$). A bubbler was used to adjust the humidity level at 20%, 50%, and 80%. Ozone was generated in a pressure vessel by a vacuum UV-lamp and injected into the airflow to set the mainstream concentration at 1 ppm and 10 ppm. Two reactors were run in parallel to

increase the throughput. The reactors are three-stage filter holder assembly made of perfluoroalkoxy alkane (PFA). In the reactor, two coated Ni-foam filters with 47 mm diameter were mounted on each stage; therefore, in total, six filters were placed in each reactor with an average total thickness of 6.2 mm (residence time was 0.12 s). The ozone concentration was measured before and after the reactor by an ozone monitor (3-channel, 106 M, 2B Technologies). All the tubes, rotameters, valves, and fittings that were exposed to ozone were made from ozone compatible materials such as stainless steel 316, PTFE, and PVDF. The ozone removal performance of the media was calculated by the following equation:

$$ozone\ conversion: \eta = \frac{C_{inlet} - C_{outlet}}{C_{inlet}} \quad (5.1)$$

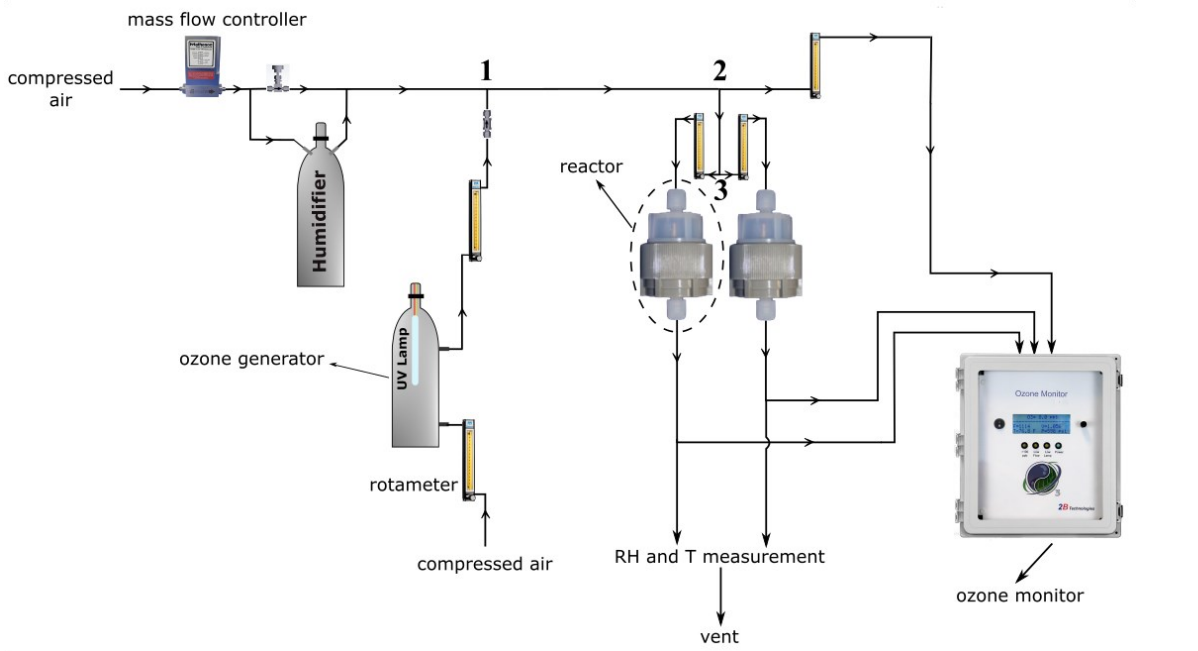

Figure 5.1. Bench-scale test set-up layout. Ozone was generated by the UV lamp in the pressure vessel and injected into the mainstream at point 1. The ozone laden airflow was split into two streams at point 3, which were introduced to the reactors (the streams have the same temperature, RH, and ozone concentration). The ozone concentration was measured before the reactors at point 2 and after each reactor.

5.4. Results and discussion

5.4.1. XRD characterization

The XRD patterns (Figure 5.2) show that all the synthesized catalysts were cryptomelane minerals having a monoclinic crystal system (potassium octahedral molecular sieve, K-OMS-2, chemical formula: $K_x(Mn^{4+}Mn^{3+})_8O_{16}$) [35], [86], [202]. The K-OMS-2 has a tunnel structure in which potassium ions are placed within a tunnel constructed of double chains of edge-sharing

MnO_6 units (2×2 tunnel). The simultaneous presence of Mn^{4+} and Mn^{3+} results in the formation of oxygen vacancy, which functions as active sites in the system [86], [203].

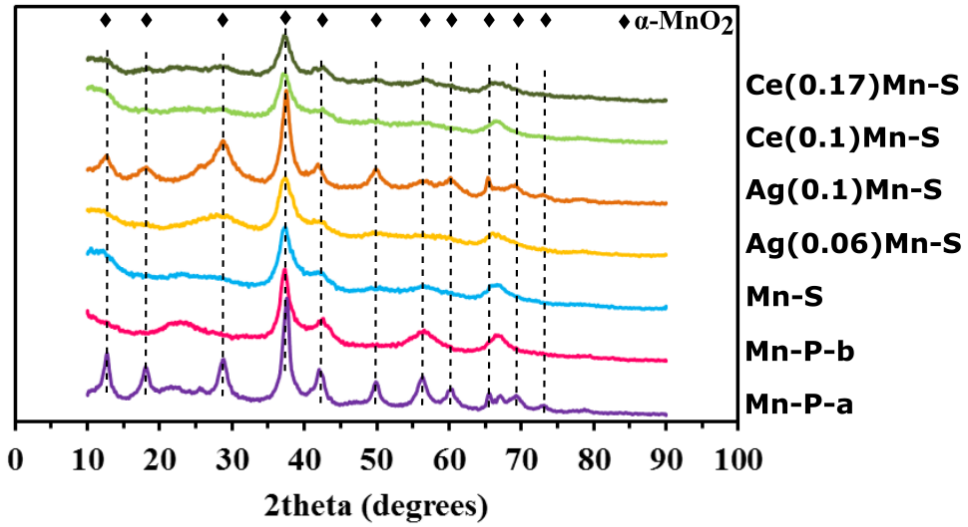

Figure 5.2. XRD patterns of synthesized catalysts. Preparation method and type of the oxidizing agent affects the crystal structures. SIR method produces catalysts with low crystallinity.

As shown by narrower peaks with higher intensity, Mn-P-a, synthesized with $K_2S_2O_8$ as the oxidizing agent, had higher crystallinity and crystal size compared to the Mn-P-b and Mn-S, made with $KMnO_4$ (Figure 5.2). This difference could be attributed to the pH of the reaction environment. Acidic conditions reportedly impact the crystal structure and crystallinity [204]. Here, the $KMnO_4$ solution was neutral while $K_2S_2O_8$ solution was acidic, with the pH adjusted to 1 for preparing Mn-P-a catalyst. Considering the MnO_2 crystal structure, concentration of K^+ has been previously shown to be an influential factor [98], [202]. K^+ ions released from $K_2S_2O_8$ solutions are three times higher than that of $KMnO_4$. Despite the fact that at low K^+ concentrations crystals with 1×1 tunnel are common, all the catalysts produced in this study had a 2×2 tunnel structure; therefore, the concentration of K^+ ion was enough in all catalysts to build 2×2 tunnel frameworks [98]. Figure 5.2 shows that in the metal doped catalysts' patterns, no distinctive peaks were observed for the dopant indicating that the dopant was homogeneously dispersed in the catalyst's crystal structure and no separate phase, like Ce_2O_3 or Ag_2O, was formed. TEM elemental mapping (Figure 5.3) also indicates the uniform dispersion of dopants and other elements in the catalysts' structure.

5.4.2. XPS characterization

The XPS general survey and the EDS-TEM results confirm the presence of Mn, O, K, and the dopant in the catalyst structure and show their molar ratios (Figures 5.3 and 5.4 and Table 5.2). According to the XPS results (Table 5.2) the elemental composition of Mn-P-b and Mn-S, which were synthesized using the same reactants but *via* different methods, were similar having $K_{0.38}Mn_8O_{16.03}$ and $K_{0.40}Mn_8O_{16.40}$ chemical formulas, respectively. However, deconvoluting the high-resolution scan of Mn2p (Figure 5.5) showed that Mn-S have higher ratio of $\frac{Mn^{3+}}{Mn^{4+}}$ than Mn-P-b (the ratios are presented in Table 5.2). The calculated AOS for both materials further confirmed a higher amount of Mn^{3+} in Mn-S structure (Table 5.2 and Figure 5.5).

According to the XPS and EDS-TEM results, shown in Figures 5.3 to 5.5 and presented in Table 5.2, doping the Mn-S catalyst with Ag and Ce was successful. However, the XPS general survey results (Figure 5.4 and Table 5.2) indicated that the actual amount of doping was lower than the initial amount that was used as reactant. Doping altered the surface chemistry of the catalyst, since the molar ratios, AOS, $\frac{Mn^{3+}}{Mn^{4+}}$ ratio, and $\frac{O_{II}}{O_I}$ ratio were changed (Table 5.2).

Table 5.2. Elemental composition derived from XPS general survey scan and $\frac{Mn^{3+}}{Mn^{4+}}$ and $\frac{O_{II}}{O_I}$, which are derived from Mn2p and O1s high resolution scans, respectively. The adventitious carbon percentage is excluded here, so the total amount of elemental composition is less than unity.

	Mn	**O**	**K**	**Ag**	**Ce**	$\frac{Mn^{3+}}{Mn^{4+}}$	$\frac{O_{II}}{O_I}$	**AOS**	**Chemical formula**
Mn-P-b	0.29	0.58	0.14	N/A	N/A	0.81	0.23	3.64	$K_{0.38}Mn_8O_{16.03}$
Mn-S	0.30	0.61	0.15	N/A	N/A	1.42	0.25	3.42	$K_{0.40}Mn_8O_{16.37}$
Ag(0.06)Mn-S	0.29	0.58	0.01	0.01	N/A	0.86	0.65	3.41	$K_{0.34}Ag_{0.36}Mn_8O_{16.37}$
Ag(0.1)Mn-S	0.27	0.55	0.01	0.02	N/A	0.75	0.27	3.63	$K_{0.42}Ag_{0.55}Mn_8O_{16.24}$
Ce(0.1)Mn-S	0.25	0.52	0.006	N/A	0.02	1.4	0.77	3.49	$K_{0.19}Ce_{0.76}Mn_8O_{16.39}$
Ce(0.17)Mn-S	0.24	0.55	0.006	N/A	0.02	0.83	0.42	3.56	$K_{0.21}Ce_{0.80}Mn_8O_{18.28}$

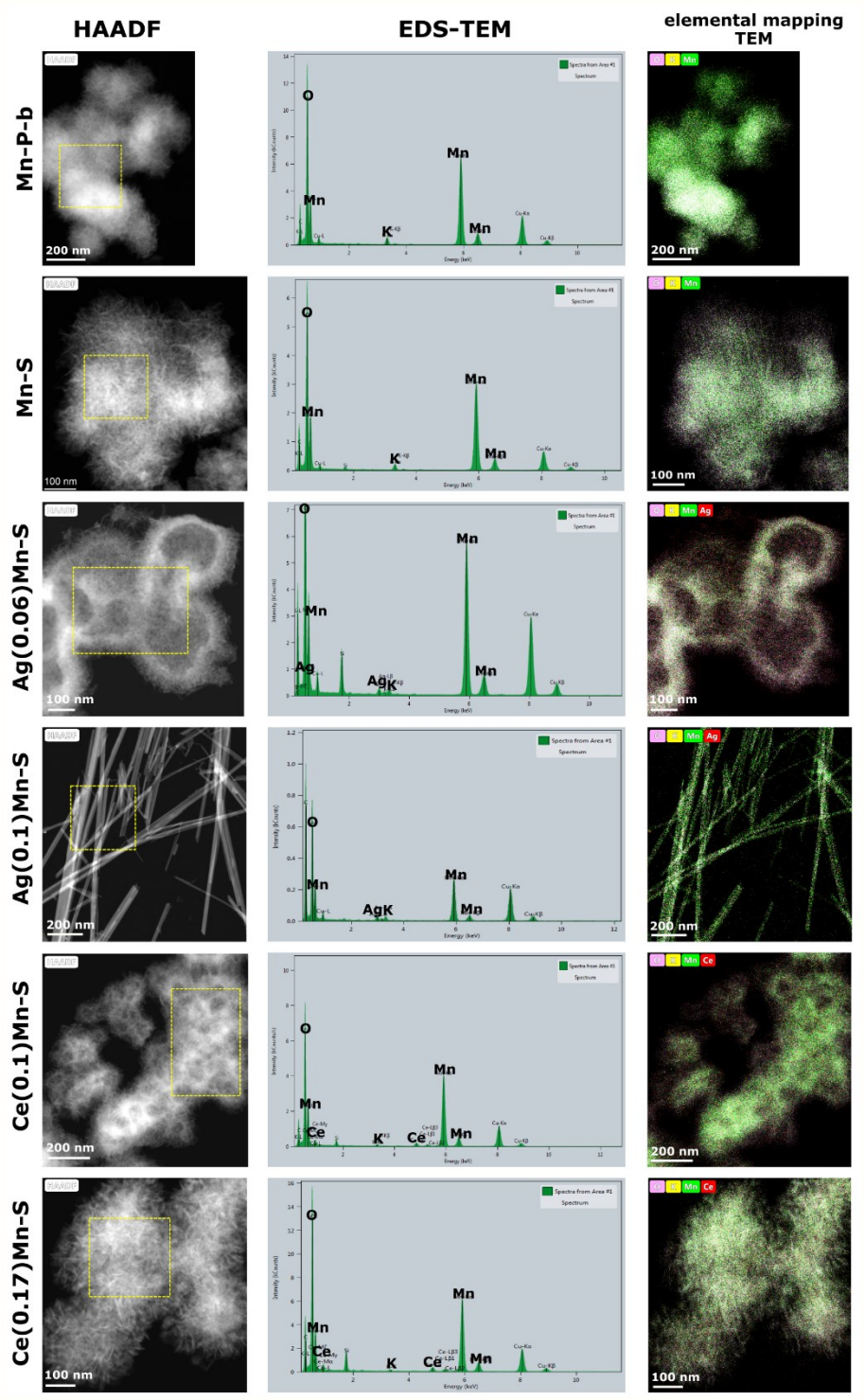

Figure 5.3. HAADF, EDS, and elemental mapping of the synthesized catalyst obtained *via* TEM. The EDS is over the marked area in the HAADF image.

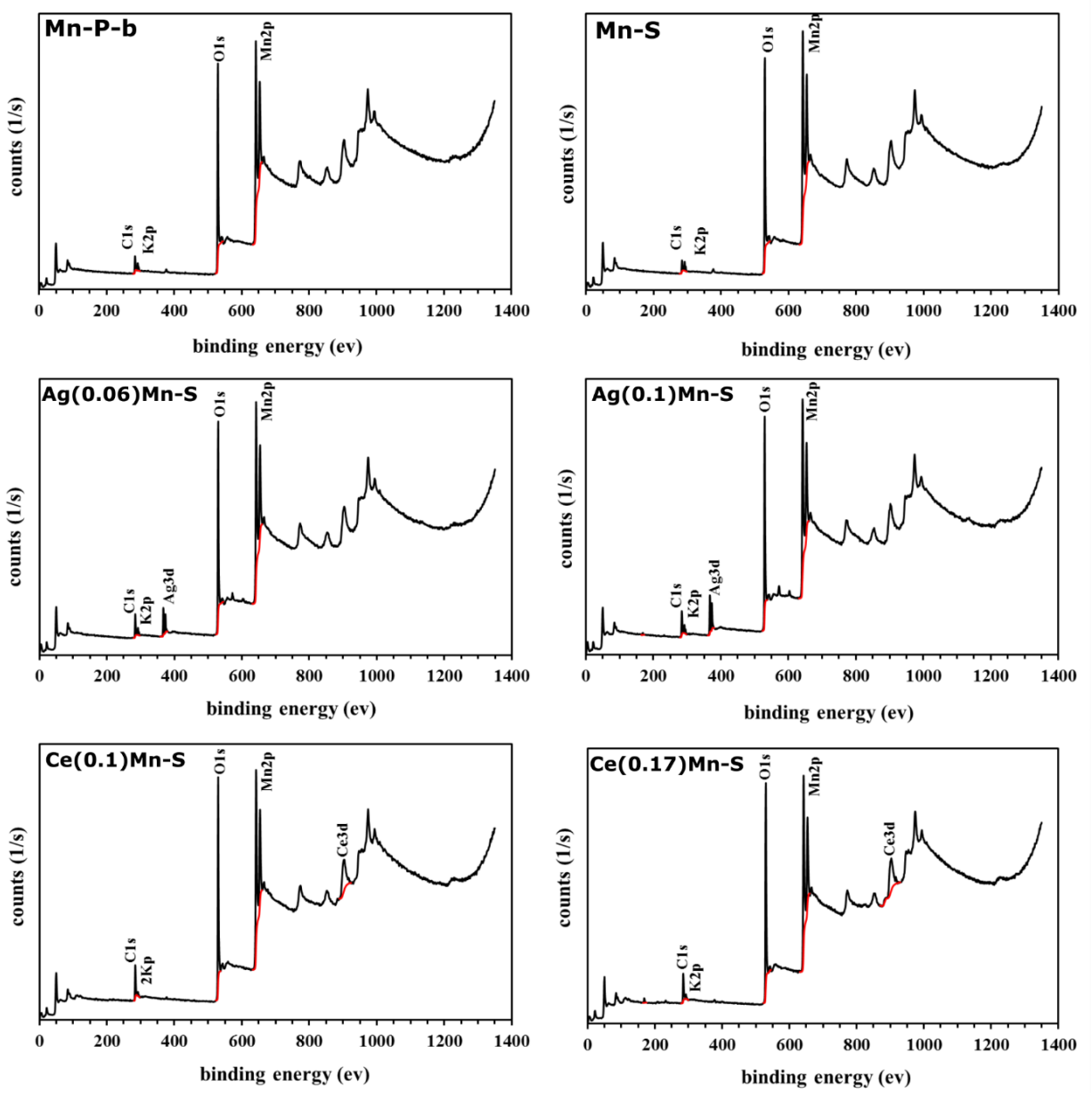

Figure 5.4. XPS general survey scan of the synthesized catalysts. C1s peak is attributed to the adventitious carbon and was used for charge correction. The C-C binding energy was adjusted at 284.8 ev.

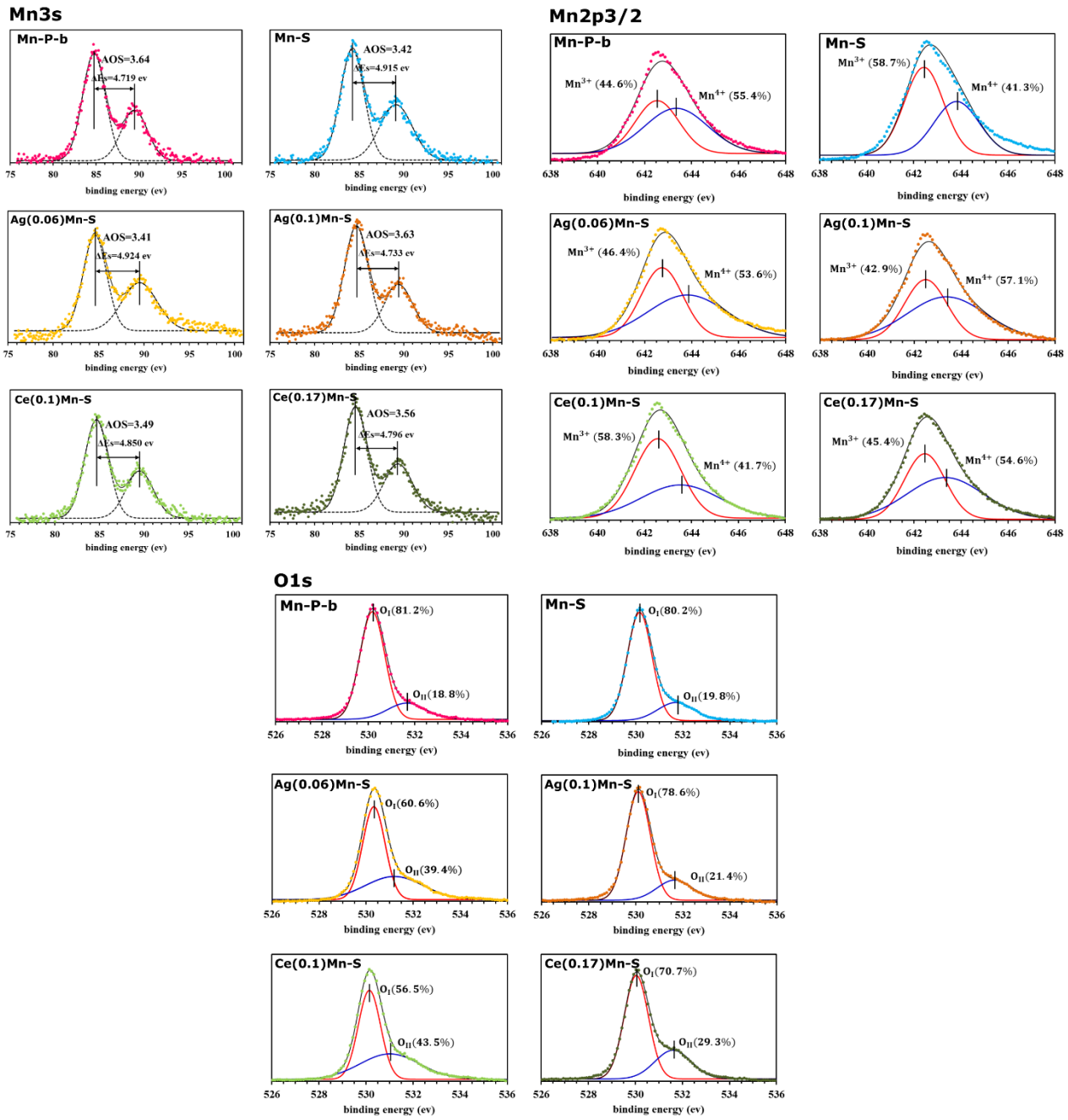

Figure 5.5. High-resolution XPS scans of Mn3s, Mn2p3/2, and O1s of synthesized catalysts. The difference in binding energy of the Mn3s peaks determines the AOS (AOS=8.956-1.126 ΔE_s). Mn2p3/2 was deconvoluted into two peaks Mn^{3+} and Mn^{4+}, and O1s was deconvoluted into two peaks O_I (lattice oxygen) and O_{II} (adsorbed oxygen)

5.4.3. Morphology

The catalyst morphology and structure were studied by SEM and TEM imaging (Figure 5.6). All the catalysts have a flower-like spherical shape except Mn-S-Ag(0.1), which has a hierarchical

nanofiber morphology. The particle sizes measured using SEM images are presented in Table 5.3. Doping the catalyst with Ce ($\frac{Ce^{3+}}{Mn^{2+}}$=0.1) decreased the particle size significantly. On the other hand, doping the catalyst with Ag ($\frac{Ag^{+}}{Mn^{2+}} = 0.1$) changed the morphology to nanofiber, Figure 5.6, with the width of 20 nm. Additionally, according to the SAED pattern, Mn-S-Ag(0.1) had a crystalline structure, in agreement with the XRD data. HR-TEM, SAED demonstrated amorphous structure for Mn-P-b and polycrystalline for Mn-S, Mn-S-Ag(0.06), Mn-S-Ce(0.1), and Mn-S-Ce(0.17).

Table 5.3. Particle size as measured by ImageJ using SEM images and particle size in suspensions as obtained from laser scattering particle size analyzer.

Catalyst	single particle size (μm)	agglomerated particles size in suspension (μm)
Mn-P-a	0.335±0.098	8.21±0.27
Mn-P-b	0.326±0.079	4.67±0.07
Mn-S	0.383±0.080	5±0.13
Mn-S-0.2	N/A	5.05±0.52
Mn-S-0.4	N/A	5.88±0.5
Ag(0.06)Mn-S	0.376±0.124	3.34±0.41
Ag(0.1)Mn-S	19.94±7.8 (nm)	2.98±0.48
Ce(0.1)Mn-S	0.173±0.021	2.36±0.28
Ce(0.1)Mn-S-0.2	N/A	3.26±0.25
Ce(0.17)Mn-S	0.321±0.043	2.80±0.67
La(1)Mn-S		4.08±0.09
La(1.67)Mn-S		3.93±1.05

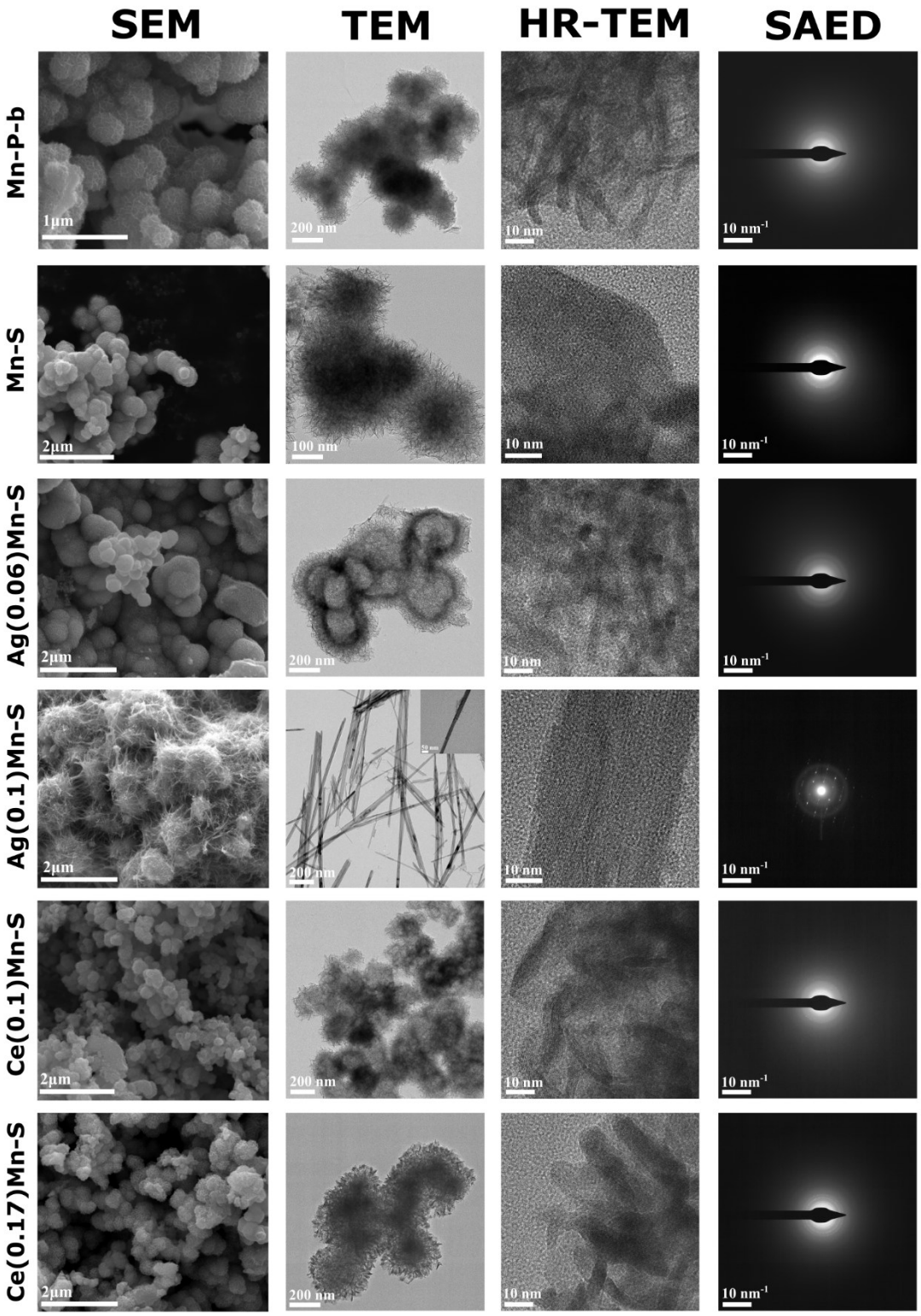

Figure 5.6. SEM, TEM, HR-TEM, and SAED images of synthesized catalysts. All the catalysts have flower-like spherical shape except Ag(0.06)Mn-S, which has a hierarchical nanofiber morphology. Also, according to the SAED patterns, all the catalysts formed polycrystalline or amorphous structure except Ag(0.06)Mn-S, which has a crystalline structure.

Table 5.4. Calculated surface area and pore volume using N_2 adsorption-desorption data.

	Mn-P-a	Mn-P-b	Mn-S	Ag(0.06) Mn-S	Ag(0.1) Mn-S	Ce(0.1) Mn-S	Ce(0.17) Mn-S	La(1) Mn-S	La(1.67) Mn-S
S_{BET} (m^2/g)	90.60	174.31	165.79	217.51	194.79	229.72	262.48	28.19	31.78
$S_{micropore}$ t-plot (m^2/g)	4.28	6.81	8.11	9.00	8.47	5.50	4.40	1.08	0.92
$S_{external}$ t-plot (m^2/g)	86.32	167.51	157.67	208.51	186.32	224.22	258.08	27.11	30.87
V_{total} t-plot (cm^3/g)	0.0438	0.0712	0.0715	0.0850	0.0869	0.0985	0.1261	0.0121	0.0152
$V_{micropore}$ t-plot (cm^3/g)	0.0018	0.0007	0.0025	0.0009	0.0023	0.0005	0.0004	0.0002	0.0002
$S_{BJH\text{-}adsorption}$ (m^2/g)	79.51	169.58	159.46	215.45	199.56	216.90	252.19	25.81	28.98
$S_{BJH\text{-}desorption}$ (m^2/g)	94.19	200.09	189.52	243.174	223.11	241.23	278.35	26.82	30.91
$V_{BJH\text{-}adsorption}$ (cm^3/g)	0.1531	0.2270	0.2357	0.2709	0.3969	0.3528	0.5000	0.1248	0.1357
$V_{BJH\text{-}desorption}$ (cm^3/g)	0.1815	0.2547	0.3207	0.3035	0.4752	0.3875	0.3885	0.0914	0.1141
d_{pore} adsorption (Å)	70.93	53.72	58.83	51.23	82.33	63.53	65.43	147.89	165.02
d_{pore} desorption (Å)	80.95	57.14	66.88	55.25	97.14	68.97	60.78	139.58	162.21

5.4.4. N_2 adsorption-desorption

The N_2 adsorption-desorption isotherms are shown in Figure 5.7. According to the IUPAC classification, all the synthesized materials have a type II adsorption isotherm and a type H3 hysteresis loop, which are attributed to aggregates of particles creating slit-shaped pores [205], [206]. The calculated micropore volume *via* the t-plot method (Table 5.4), also shows the negligible volume of micropores. Moreover, no microscale pore was observed in SEM or TEM images. From the adsorption-desorption data, the specific surface area, pore volume, pore size distribution, and average pore width were calculated (see section 5.3). Using $KMnO_4$ (Mn-P-b) as the oxidizing agent instead of $K_2S_2O_8$ (Mn-P-a) led to a catalyst with a higher specific surface area, higher pore volume and smaller pore width. It seems that the acidic environment of $K_2S_2O_8$ solution reduced the specific surface area by causing higher crystallinity. On the other hand, the S_{BET}, pore volume, and pore width of Mn-P-b and Mn-S were in the same range (Table 5.4). Doping the catalyst increased the S_{BET} by decreasing the crystallinity, leading to larger amounts of accessible oxygen vacancies [35], [189].

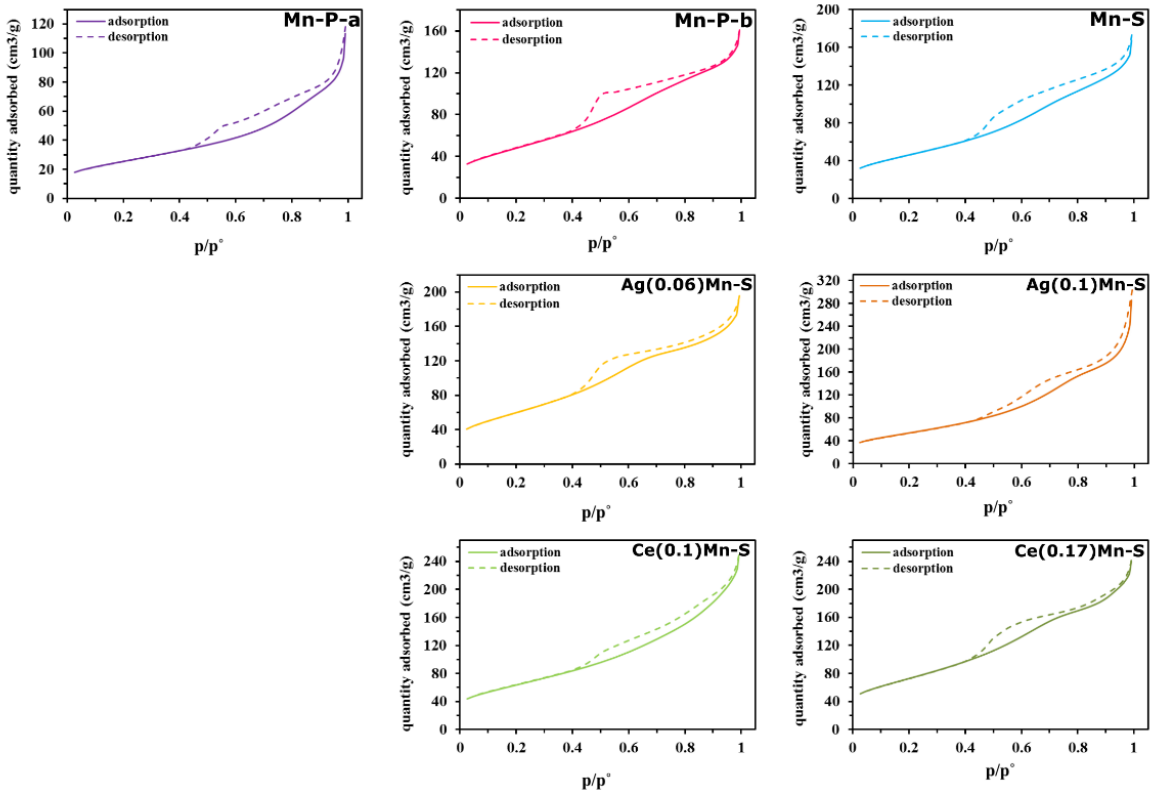

Figure 5.7. N_2 adsorption-desorption isotherms. All the catalysts have a type II adsorption isotherm with a type H3 hysteresis loop according to IUPAC standard classification.

5.4.5. Ozone decomposition performance of synthesized catalysts

The synthesized catalysts were coated on Ni-foam filters to be assessed for ozone decomposition. It was confirmed that the uncoated Ni-foam filter had no ozone removal capability. The mass of deposited catalyst on the Ni-foam filter per unit of area was 1.36±0.11 mg/cm^2. The particle size distribution was measured to assess the quality of deposition. SEM images of the filters (Figure 5.8 and Figure S5.1) showed that the deposition was uniform. Agglomerations were of larger size for Mn-P-a particles (Figure S5.1). For other catalysts, no difference between the size of agglomerations deposited on the filters was seen in SEM images, since their sizes in the suspension were in the same range. Undoped catalysts with and without PVDF were tested at 10 ppm ozone and dry condition. They had 100% efficiency during 6 h exposure to ozone. According to previous studies, humidity has a detrimental effect on the MnO_x-based catalysts. To evaluate the influence of modification techniques on humidity's adverse effects, all the filters were exposed to 10 ppm ozone for 6 h in three different humid conditions. Filters with better performance were selected and exposed to 1 ppm ozone concentration for 6 h. The results are shown in Figure 5.9 and discussed below.

5.4.5.1. The effect of synthesizing procedure

Mn-P-b showed significantly better ozone removal performance than Mn-P-a (Figure 5.9). At 20% RH level, Mn-P-b showed >95% efficiency after 6 h ozone exposure while Mn-P-a had <55% efficiency. Elevating the RH level deteriorated the performance of both catalysts, but Mn-P-a experienced a greater decline than the Mn-P-b. For instance, at 50% RH, Mn-P-a experienced 50% efficiency loss in less than 30 min while Mn-P-b underwent the same loss after 6 h. That means, the Mn-P-b had more humidity-resistant active sites. Furthermore, according to the XRD results, Mn-P-b had a lower crystallinity, and consequently smaller crystal size than Mn-P-a. Lower crystallinity translates into a higher specific surface area, at least two times higher, as proved by the calculated S_{BET} (Table 5.4). The SEM images (Figure 5.6) show that both catalysts have similar spherical shapes, morphologies, and particle sizes (Mn-P-a: 334±98 nm, Mn-P-b: 326±79 nm). However, in the suspension used for catalyst deposition on filters, Mn-P-a sizes were larger (almost two times, Table 5.3), indicating the aggregation of Mn-P-a particles, which could reduce the available surface area for reaction. Therefore, the enhanced performance of Mn-P-b could be due to its higher specific surface area and its ability to form a well dispersed suspension, which

increased the available and accessible oxygen vacancies for ozone decomposition on the filter compared with Mn-P-a.

Mn-P-b and Mn-S had similar ozone decomposition performances, except at 50% RH where Mn-S showed a better performance (56% compared to 45%, Figure 5.9). Their XRD pattern, morphology, particle size, specific surface area, and pore volume were similar; however, their chemical properties were different. During the SIR process, the continuous grinding exposes the surfaces of the reactants to interaction. This results in surface reactions and the formation of well-dispersed defects on the surface of produced materials, which is an advantage of the method [91], [96], [207]. The AOS of Mn-S was lower than that of Mn-P-b and its $\frac{Mn^{3+}}{Mn^{4+}}$ ratio was higher (Table 5.2), meaning that its surface density of oxygen vacancies were higher. Therefore, the SIR method produced catalysts with enhanced density of surface active sites that were more humidity-resistant than those on the Mn-P-b surface. Based on these results, Mn-S was selected for further modifications using chemical and physical methods.

5.4.5.2. The effect of metal doping

Doping of Mn-S with Ce and Ag improved its ozone decomposition performance while doping with La worsened the performance dramatically. Overall, the relationship between doping intensity and efficiency seemed complicated. Higher doping levels in most cases had adverse or negligible effects, and lower doping levels had a favorable effect in all cases. The level of La doping, selected according to the previous studies [192], [208], was much higher than Ce, and Ag, which led to reducing the S_{BET} (Table 5.4) and the efficiency (Figure 5.9) dramatically. Ce at a low doping level (0.1) showed the highest performance in moderate and high humidity (50-80%) and outperformed Ag. High Ce content, however, had a significant negative effect on the catalytic performance. The catalysts with the highest efficiencies, Mn-S, Ag(0.06)Mn-S, and Ce(0.1)Mn-S, were also tested at a lower ozone level (1 ppm). In this condition, Ce(0.1)Mn-S outperformed the others at all humidity levels (Figure 5.9)—with better results at lower humidities. Surprisingly, in some cases, even the low doping levels had poor performance. Notably, Ag(0.06)Mn-S suffered a considerable efficiency loss (Figure 5.9).

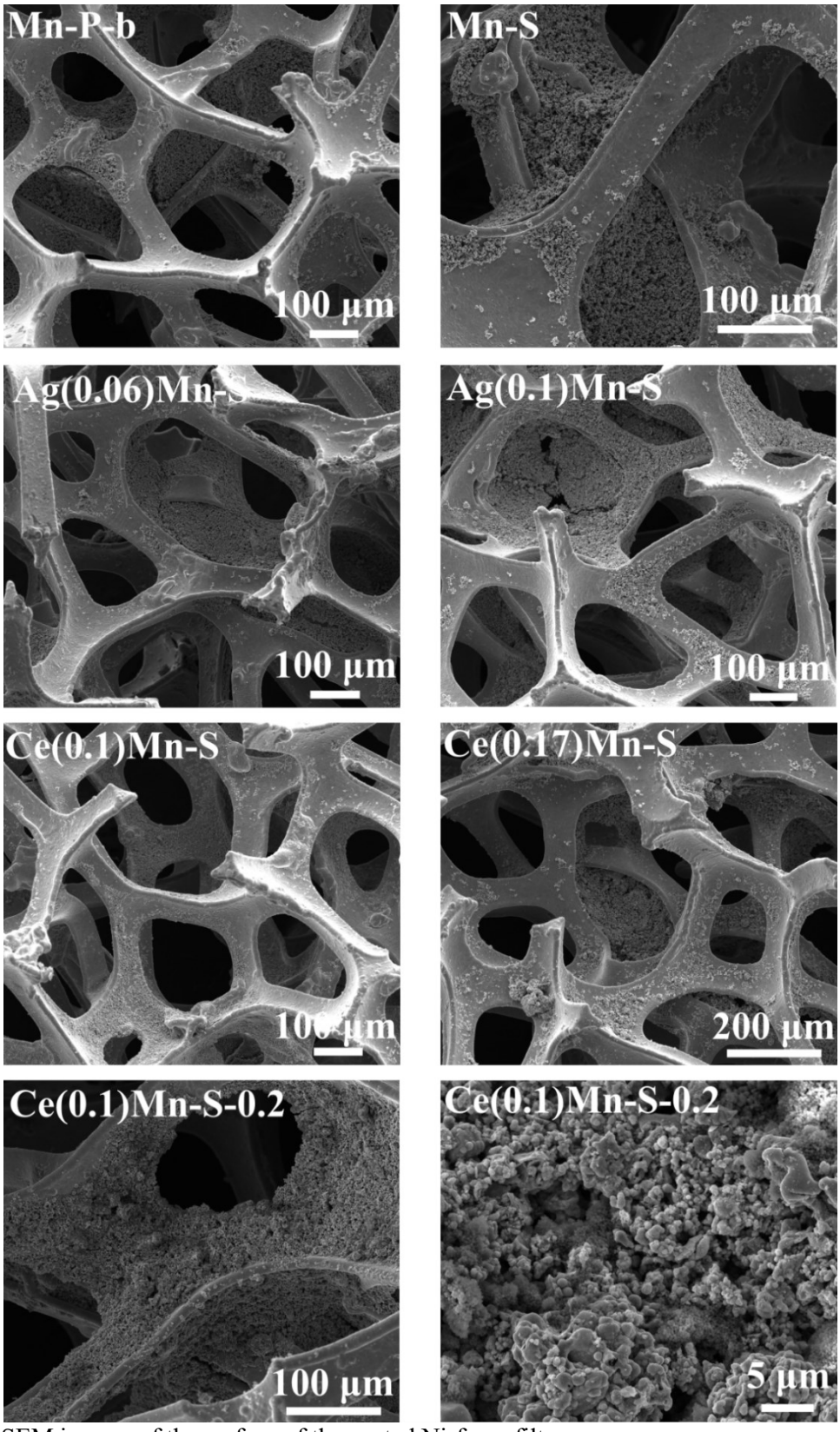

Figure 5.8. SEM images of the surface of the coated Ni-foam filters.

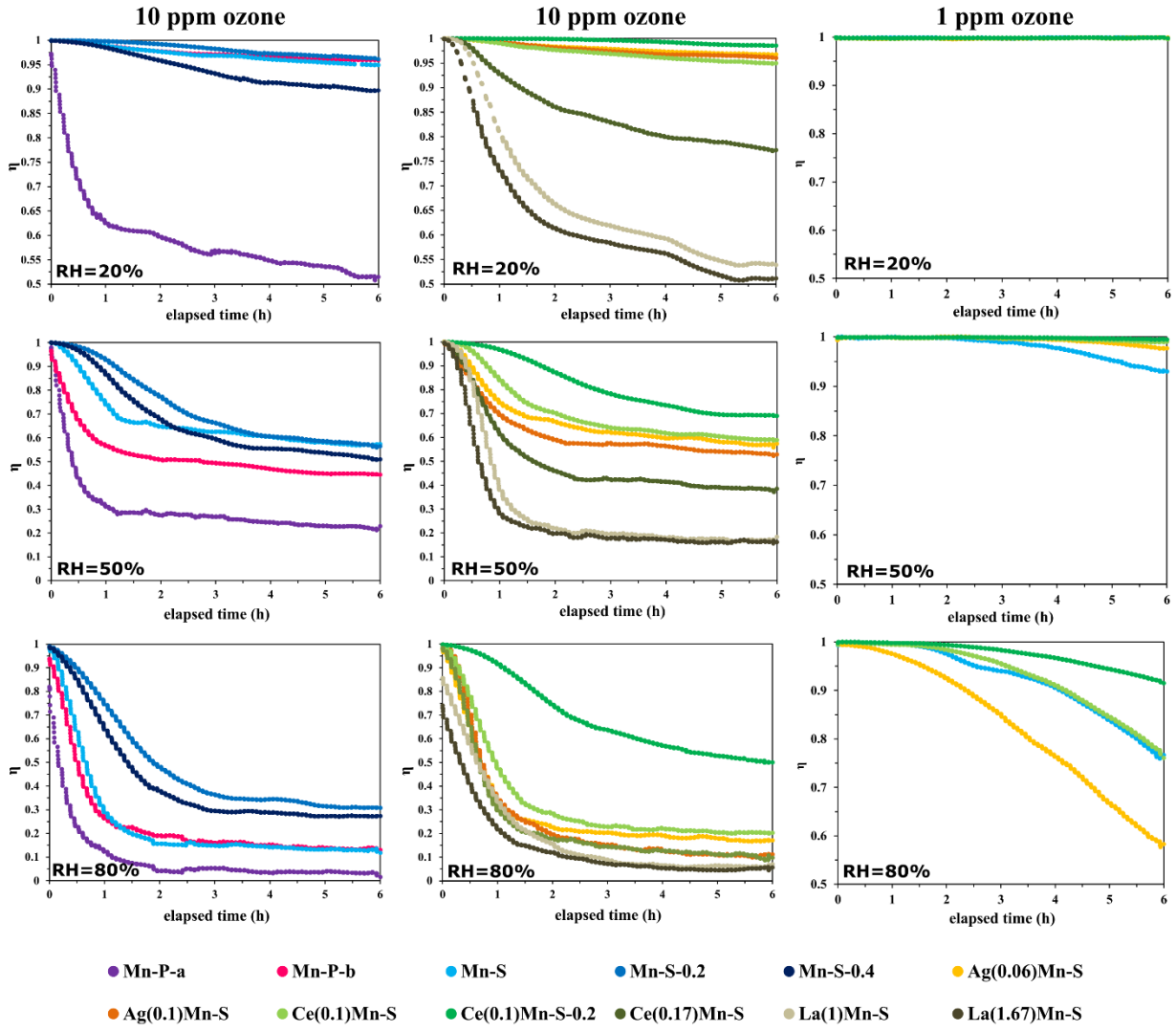

Figure 5.9. The ozone removal of filters coated with synthesized catalysts at two ozone concentration and three humidity levels. The airflow rate was 5 L/min, and the temperature was 20 °C. Humidity had a negative effect on all the catalysts. Doping with Ce and depositing PVDF beside the catalyst improved its efficiency significantly.

To gain insights into this variability, key catalytic parameters were analyzed. Doping increased the S_{BET} of the Mn-S catalyst and changed the particle size (Tables 5.3 and 5.4). Doping also changed the morphology of the catalysts (Figure 5.6). Pristine Mn-S had a flower-like spherical shape, doping with a lower level of Ce and Ag, transformed the morphology into flower-like hollow spherical shapes. At increased dopant levels, Ag resulted in nanofibers while Ce produced spheres like Mn-S. The particle sizes were also dopant dependent. Ce(0.1)Mn-S had the smallest size among the spheres while there was no substantial change in particle size for Ag(0.06)-doped samples. The combined effect of particle shape (hollow spherical structures) and size (smaller

particles) makes the lower doping level more favorable in terms of the reaction surface area. In addition, higher coating quality was observed for Ce(0.1)Mn-S filters (Figure 5.8) as smaller particles in suspensions tend to cause better dispersion and less agglomeration.

XPS characterization showed that changes in surface chemistry at lower amount of dopant could lead to higher catalytic activity than higher amounts. During the metal doping process, the dopant could substitute for the potassium ions within the tunnel or one of the manganese ions in the framework [35], [86], [203]. High-resolution XPS scan of Mn3s (Figure 5.5) revealed that the AOS of the doped catalyst using the lower amount was close to the Mn-S; however, intense doping increased AOS. Also, according to the high-resolution scan of Mn2p (Figure 5.5), Ag and Ce doping slightly decreased the $\frac{Mn^{3+}}{Mn^{4+}}$ ratio. Previously, it was reported that Ag ions can substitute for the K^+ ions inside the tunnel [120], while Ce ions can substitute for both K^+ and Mn ions [25], [66], [115], [119]. Variation in the charge balance leads to formation of oxygen vacancy, to hold up the neutrality of the material, which could decrease the AOS [35], [40], [101], [105], [189]. Since a lower amount of dopant changed AOS negligibly, the dopants are likely substituted with K^+ ions in the tunnel. The elemental composition results (Table 5.2) show the reduction in K abundance after doping, which confirmed this hypothesis. But further additions of dopant increased the AOS, highlighting that the distortion was not in favor of increasing the $\frac{Mn^{3+}}{Mn^{4+}}$ ratio. The most remarkable changes were in the O1s spectra (Figure 5.5). O_I and O_{II} in the high-resolution scan of O1s are ascribed to lattice oxygen and oxygen species adsorbed in oxygen vacancies, respectively. O_{II} amount, in other words, represents the density of surface oxygen vacancy [188]. Ce(0.1)Mn-S, with the best ozone decomposition performance, had the highest $\frac{O_{II}}{O_I}$ ratio implying that it had the greatest density of surface active sites. The reduced susceptibility of Ce(0.1)Mn-S to humidity at 80% RH is consistent with the high concentration of active sites observed in this characterization. These results show that the doping performed with the appropriate material at an optimized composition can significantly improve the catalyst activity at low and moderate RH but cannot solve the catalytic removal of ozone in highly humid conditions.

5.4.5.3. The impact of PVDF deposition besides MnO_x catalyst

Doping the Mn-S catalyst with Ce enhanced its performance, particularly below the 80% RH level. However, at 80% RH, water molecules could inhibit ozone molecules from reaching the active sites (i.e., oxygen vacancies). To overcome the detrimental effect of humidity, this study

presents a novel and feasible approach. PVDF polymer powder, a hydrophobic (PVDF contact angle ~145°) [209], [210] and ozone compatible material, was added to the catalyst suspension and dispersed using Tween 20 surfactant. A well-mixed suspension containing catalyst and polymer particles was coated on the Ni-foam filters. The patches of agglomerated polymer particles (hydrophobic zone), placed uniformly among catalyst particles (active hydrophilic zone), were observed in the SEM images (Figure 5.8). The ozone decomposition results illustrate the remarkable effect of the added hydrophobic polymer (Figure 5.9). PVDF-to-catalyst mass ratios of 0.2 and 0.4 were tested for Mn-S catalysts, termed Mn-S-0.2 and Mn-S-0.4, respectively. Mn-S-0.2 had better performance than Ag- and Ce-doped catalysts in all humid conditions. Below 80% RH, the Mn-S-0.4 had lower efficiency than the Ag- and Ce-doped catalysts; however, interestingly, at 80% RH, its efficiency was greater than both, which demonstrates the strong contribution of physical modifications in tackling humidity effects.

To leverage both physical and chemical effects, the most efficient doped catalyst, Ce(0.1)Mn-S, was modified by adding polymer. The modification produced a superior impact such that the efficiency of Ce(0.1)Mn-S-0.2 at 80% RH and 10 ppm ozone was 2.5 times higher than the Ce(0.1)Mn-S. At 1 ppm ozone level, Ce(0.1)Mn-S-0.2 had >99% efficiency up to 50% RH, and, at 80% RH, it had >91% efficiency after 6 h exposure to ozone, which was 1.2 times higher than the efficiency of Ce(0.1)Mn-S. Moreover, polymer incorporation prevents the sudden efficiency drop at early exposure times. Therefore, the filter could hold up the initial efficiency longer (Figure 5.9). For instance, comparing Ce(0.1)Mn-S and Ce(0.1)Mn-S-0.2, the latter had >90% efficiency by 1 h while the first one fell below 90% by 20 min.

To elucidate the mechanism governing the effect of hydrophobic polymer blends, first the detrimental effect of humidity was studied. Not only do water molecules compete with ozone for active sites, but also form water bridges in the neck between catalyst particles as a result of capillary condensation, according to the Kelvin equation [211], [212]. The deposited catalyst particles on the Ni-foam filter form raspberry-like densely packed agglomerates with concave sites. Thus, at high RH levels, water molecules condense in the interparticle cavities and cover the active sites, leading to efficiency loss. Chemical modification of catalyst could strengthen the active sites against humidity and enable ozone to win the competition, but it cannot inhibit the formation of water bridges at high RH. Depositing a hydrophobic polymer among the catalyst zones changes the hydrophilicity of the filter. Considering the excellent dispersion of PVDF

particles, sized 0.230±0.075 μm (Figure S5.2), among the catalyst particles, this could result in an interconnected network of hydrophobic and hydrophilic regions. These effects prevent the formation of water bridges in the neck between a hydrophobic and a hydrophilic surface and improve efficiency. The modification of surface wettability could also hinder water condensation between the catalyst particles and the Ni-foam filter, enhancing the active reaction surface. Using an excessive amount of polymer decreased the efficiency, due to the potential wrapping of the catalyst surface with PVDF agglomerates (Figure S5.3).

These findings indicate that the simultaneous improvement of the density of oxygen vacancies and their humidity resistance, along with physical modifications that prevent interparticle water bridges and capillary condensation, could result in a highly efficient MnOx-based catalytic media for ozone removal. It is envisioned that such catalysts will be of interest to a wide range of applications. A potential application could be usage as cartridges in face masks for protecting workers' health. Ce(0.1)Mn-S-0.2 showed >90% efficiency for 6 h at 1 ppm ozone and 80% RH, so, it can keep the concentration below the permissible exposure limit (PEL, 100 ppb). Also, at elevated ozone concentrations, the high initial efficiency was extended, and the filter could decrease the ozone concentration from the immediately-dangerous-to-human-health level (IDHL, 5 ppm) to the short-term exposure limit (STEL, 300 ppb) level for at least 1 h. Furthermore, the Ce(0.1)Mn-S-0.2 has the potential to be used in aircraft cabins and the exhaust of industrial ozone generators. Because the filter showed a superior performance at high RH, it can minimize energy consumption by reducing the operating temperature of ozone decomposition units. For this purpose, coating techniques for the catalyst/polymer blend should be improved in future works.

5.4.6. Theoretical calculations

All the structures were optimized using the DFT method at the PBE/Def2-SVP level of theory. To calculate the structural stability and thermodynamic parameters of the corresponding complexes, frequency calculations were performed, and it was confirmed that the stationary points correspond to minima with real frequencies. This indicates the stability of the Mn complexes with the selected atoms K, Ag, and Ce. The optimized geometries are shown in Figure 5.10 and the theoretical computation results are represented in Table 5.5. The Mn-O bond length in the Ce-doped catalyst was longer than the Ag-doped and the undoped ones. Longer Mn-O bond facilitates the formation of oxygen vacancies [24], which is conforming to the XPS results showing a higher density of oxygen vacancies for the Ce-doped catalyst.

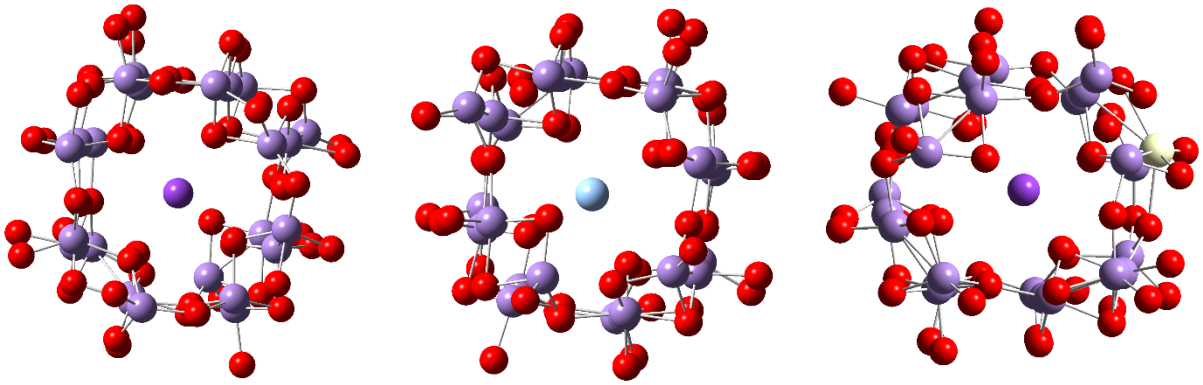

Figure 5.10. Optimized geometries of the Mn-S AgMn-S and CeMn-S catalysts at PBE/Def2-SVP level of theory. The dangling bonds at the edges of the corresponding structures were saturated by hydrogen atoms. (red spheres: O, light purple spheres: Mn, Dark purple: K, light blue: Ag, light yellow: Ce)

The calculated energies of the frontier orbitals, which are the highest occupied molecular orbital (HOMO) and lowest unoccupied molecular orbital (LUMO), indicate that the Ce-doped catalyst has the lowest HOMO-LUMO energy gap. The smaller band gap means that the catalyst can easily accept or donate electrons, making it more reactive [213]. Also, it implies that the catalyst has a higher ability to undergo the redox process [214], [215]. These findings confirm the highest catalytic activity of the Ce-doped catalyst compared to the Ag-doped and the undoped ones for ozone decomposition.

The ozone decomposition mechanism includes three steps (Equations 5.2-5.4). Among these steps, step three (Equation 5.4) has proved to be the limiting one [24], [63]. According to the frontier orbital theory [216], electron transfer occurs between the HOMO of the O_2^{2-} intermediate and the LUMO of the catalyst [91]. The orbital energies were calculated through DFT simulations and the HOMO and LUMO energies are reported in Table 5. The energy gap between HOMO of the O_2^{2-} and LUMO of the catalyst is the lowest for the Ce-doped catalyst, implying easier electron transfer and oxygen vacancy release. These results are consistent with the catalytic performance of the synthesized materials.

$$O_3 + Mn^{(n+2)+} - V_O \rightarrow O_2 + Mn^{(n)+} - O^{2-} \quad (5.2)$$

$$O_3 + Mn^{(n)+} - O^{2-} \rightarrow O_2 + Mn^{(n)+} - O_2^{2-} \quad (5.3)$$

$$Mn^{(n)+} - O_2^{2-} \rightarrow O_2 + Mn^{(n+2)+} - V_O \quad (5.4)$$

Table 5.5. Theoretical computation results. All the energies are in ev unit.

	Mn-S	AgMn-S	CeMn-S	O_2^{2-}
HOMO energy	-7.8645	-8.0047	-3.024	14.88
LUMO energy	-7.8315	-7.8887	-3.0006	18.25
$\mathbf{E_{LUMO} - E_{HOMO}}$	0.033	0.116	0.0234	3.37
$\boldsymbol{E_{HOMO,O_2^{2-}} - E_{LUMO,catalyst}}$	22.72	22.77	17.88	NA
Mn-O bond length (Å)	1.83	1.84	1.85	NA
Hardness[1]	0.0165	0.0580	0.0117	NA
Electronic chemical potential[2]	-7.8480	-7.9467	-3.0123	NA

[1] $hardness = \frac{E_{LUMO} - E_{HOMO}}{2}$

[2] $electronic\ chemical\ potential = \frac{E_{LUMO} + E_{HOMO}}{2}$

5.5. Conclusion

This study investigated the simultaneous chemical and physical modification of an MnO_x-based catalyst for ozone decomposition. The SIR method, a feasible synthesis procedure, produced Mn-S catalyst with superior properties than Mn-P-b, which was prepared via co-precipitation method. Moreover, Mn-S catalysts were successfully doped with transition metals including Ag, Ce, and La, through the SIR procedure. Metal doping with optimum type and amount of dopant, improved the catalyst's physicochemical properties, such as the specific surface area and the density of oxygen vacancies. Catalyst doping with La at the tested molar ratios ($\frac{La^{3+}}{Mn^{2+}} = 1,\ 1.67$) had adverse effect on the Mn-S properties such that La-doped catalyst had much lower efficiency than Mn-S. Ce(0.1)- and Ag(0.06)-doped catalysts (used the low level of dopant), showed a substantial improvement in ozone decomposition. Among the produced morphologies, varying from nanofiber to spherical, the flower-like hollow spherical shapes, observed in Ce(0.1)Mn-S, had the highest performance. Additionally, DFT calculations confirmed the higher density of oxygen vacancy of the Ce-doped catalyst compared to the Ag-doped and the undoped ones. The Ce-doped catalysts, however, still suffered from considerable efficiency loss due to detrimental effect of water molecules, particularly at 80% RH. This can be attributed to the higher likelihood of water condensation among catalyst particles, which can cover the active sites. Therefore, a physical

modification strategy was used to overcome this issue. The catalysts were physically blended with PVDF, a hydrophobic polymer, and deposited on Ni-foam filters. At optimum amounts, polymer addition resulted in a significant improvement in Ce(0.1)Mn-S performance. Even the undoped catalysts mixed with PVDF showed better removal efficiency than the Ce(0.1)- and Ag(0.06)-doped catalysts, which highlights the importance of the inhibition of interparticle water condensation. Leveraging both chemical and physical modification techniques an enhanced MnO_x-based catalyst, Ce(0.1)Mn-S-0.2, was prepared and evaluated. This catalyst has the potential to be used in several applications, from face mask cartridges to aircraft cabins.

5.6. Supporting information

5.6.1. Computational details

The choice of exchange-correlation functional, basis set, convergence criteria, and other computational parameters affect the accuracy and efficiency of the calculations. Therefore, it is crucial to carefully select the appropriate methods. The selected exchange-correlation Perdew-Burke-Ernzerhof (PBE) functional in this study, which belongs to the class of generalized gradient approximation (GGA) functionals, has been widely used for solid-state systems. The DEF2-SVP (split valence polarization) basis set was employed. It includes a set of valence functions that describe the core and valence electrons of the atom and a set of polarization functions that capture the electron correlation effects. However, to reduce the computational costs, an effective core potential (ECP) approach was used for heavier atoms (Mn, Ag, and Ce). The ECP replaces the potential experienced by the core electrons with an effective potential, reducing the computational burden while maintaining accuracy for valence electrons. Therefore, by using an ECP the number of electrons that need to be explicitly included in the electronic structure calculations is reduced. Stuttgart-Dresden (SDD) ECP was used in this study for Mn, Ag, and Ce atoms. SDD ECP replaces the core electrons of the heavy atoms with a pseudopotential. It can capture the effect of core electrons on the valence electrons.

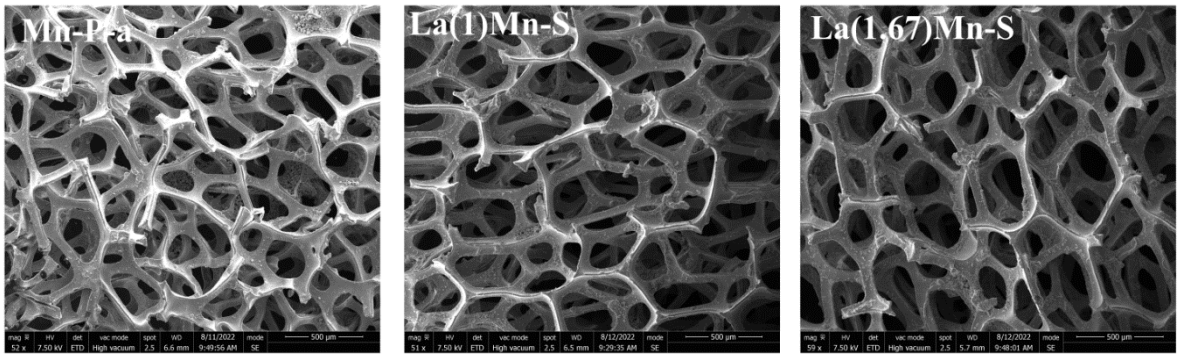

Figure S 5.1. SEM images of the synthesized catalysts coated on Ni-foam filter.

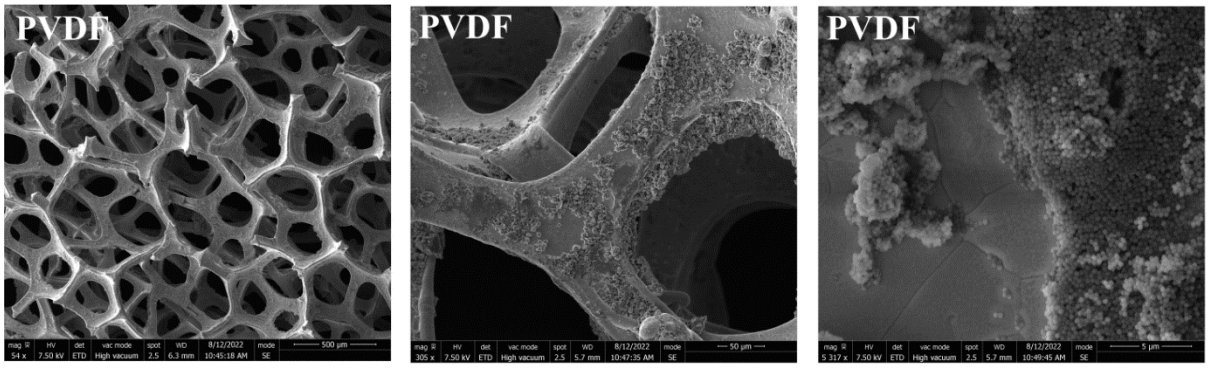

Figure S 5.2. SEM images of the Ni-foam filter coated with PVDF

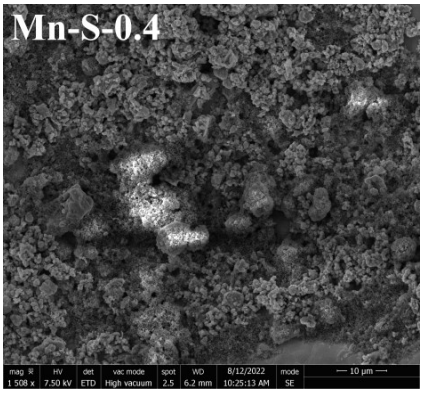

Figure S 5.3. SEM image of Ni-foam filter coated with Mn-S-0.4

Chapter 6. Conclusion and future works

6.1. Summary and conclusion

Ozone is one of the most important inorganic pollutants due to its wide application in industry as well as its capability to change air chemistry by generating secondary organic pollutants. Occupants and workers could be at risk of exposure to ozone beyond the permissible limits set by organizations like OSHA and WHO. In case of ozone leakage in the industrial environments, immediate evacuation is mandatory. Also, ozone can adversely affect the environment and agricultural production. Therefore, ozone removal is a critical issue to protect occupants' health and environment. Different technologies including AC-based filters, catalytic oxidation and photocatalytic oxidation have been investigated for ozone removal. Depending on the operational conditions, an AC-based media or a MnO_x-based catalyst can be used for efficient ozone decomposition. MnO_x-based catalytic processes have shown the best performances at high ozone levels and airflow rates. However, their efficiency declines significantly in the presence of high levels of water molecules. The main goal of this research was to develop a novel humid-resistant MnO_x-based catalyst. An enhanced MnO_x-based catalyst was synthesized via a feasible method, which has the capability of mass production. Metal doping, using silver, and cerium, was used to modify this catalyst. This modification resulted in increasing the specific surface area, and enhancing the density of oxygen vacancies. Also, the Ce-doped catalyst showed more resistance at high humidity levels than Ag-doped or the undoped ones. The Ce-doped catalyst was further modified by mixing it with PVDF polymer particles. This modification led to preventing the formation of water bridges between the catalyst particles and improving the efficiency. Moreover, the common ozone removal media, including ACs, and catalysts, were investigated thoroughly in this research to elucidate the impact of operational conditions on the materials performance, which led to facilitate selecting the best method for ozone removal. The major results of this research are presented more specifically in the following.

Chapter 3

- Testing all the materials according to the ASHRAE 145.2 standard method revealed that this test method cannot fulfil its requirements in a one-day test run since none of the materials could reach the 50% breakthrough.

- Coconut shell-based AC showed the best performance (among the eleven tested granular media) at ozone levels below 200 ppm during 6 h exposure to ozone, despite having lower specific surface area than coal-based ACs.
- At ozone levels higher than 200 ppm small size MnO_x-based catalyst had the superior performance compared to the other materials.
- KOH impregnated coal-based AC had an improved ozone removal performance by more than 60% compared to the virgin coal-based one.
- The chemisorption capacity of ACs is much higher than their catalytic capability.
- SEM images and XPS results showed the strong interaction between ozone and the coconut shell-based AC, highlighting its high chemisorption capacity than the other ACs that were tested in this study.
- The high chemisorption capacity of AC-based media makes them good candidates for indoor air applications in residential buildings and office buildings:
    - If the ozone concentration can rise above 1 ppm (<50 ppm) for a short-term, coconut shell and KOH impregnated coal ACs are the best choices among the AC-based media.
- When the ozone concentration is constantly high, like in the intake air pathway of aircraft cabins or the exhaust of ozone generation systems, catalyst-based media with a high density of stable active sites are desirable.

Chapter 4

- The ozone removal performance of granular media could vary over a wide range depending on the operational conditions.
- Due to differences in chemical and physical properties of granular materials, each ozone removal technology performs uniquely.
- Statistical and kinetic modeling analyses revealed important correlational relationships between operational parameters and ozone removal efficiency.
    - The airflow rate and ozone level were the most influential parameters for ACs whereas the effect of humidity was the most significant one on the catalyst's performance.
    - The effect of humidity was one of the most complex effects owing to the sophisticated chemical and physical interactions of water with the materials' surface.

- Increasing the humidity level from 0% to 70% had a negative effect on the removal performance of coal-based AC, a dual effect on coconut shell-based AC (first negative up to 35% and then positive until 70%), no effect on KOH impregnated coal-based, and a negative effect on MnO_x-based catalyst.

- The statistical analysis showed that the impact of two-way interactions of parameters could be significant; the most important ones were found to be *O_3*airflow* on ACs and *RH*airflow* on catalyst.
    - At low airflow rates, coconut shell AC and KOH impregnated coal AC were indifferent to ozone, and humidity had no effect on CAT-E, while at high airflow rates the impacts were considerable.
- Among ACs, the ozone removal efficiency of the coconut shell one, despite having the highest chemisorption capacity, experienced the most dramatic vulnerability to the change of the operational parameters, while KOH impregnated coal, having OH^- groups on its surface, experienced the least.
- For industrial applications, at elevated ozone concentrations, MnO_x-based catalysts could be the best candidate.
- Comparing the ACs with the catalyst revealed that, on average, the MnO_x-based catalyst is the most efficient ozone removal media.

Chapter 5

- The solid interface reaction method, a synthesis procedure, produced a catalyst with superior properties than the catalyst that was prepared via co-precipitation method.
- The catalysts were successfully doped with transition metals including Ag, Ce, and La, utilizing the solid interface reaction method.
- Metal doping with optimum type and amount of dopant, improved the catalyst's physicochemical properties, such as the specific surface area and the density of oxygen vacancies.
- Doping catalyst with La at the tested molar ratios ($\frac{La^{3+}}{Mn^{2+}} = 1,\ 1.67$) had adverse effect on the pristine catalyst's properties such that La-doped catalyst had much lower efficiency.
- Ce(0.1)- and Ag(0.06)-doped catalysts (used the low level of dopant), showed a substantial improvement in ozone decomposition.

- Among the produced morphologies, varying from nanofiber to spherical, the flower-like hollow spherical shapes, observed in Ce(0.1)-doped MnO_x, had the highest performance.
- The doped catalysts, however, still suffered from considerable efficiency loss due to detrimental effect of water molecules, particularly at 80% RH. This can be attributed to the higher likelihood of water condensation among catalyst particles, which can cover the active sites.
- The catalysts were physically blended with PVDF, a hydrophobic polymer, to overcome the adverse effect of water molecules. At optimum amounts, polymer addition resulted in a significant improvement in Ce(0.1)-doped MnO_x performance.
    - The undoped catalysts mixed with PVDF showed better removal efficiency than the Ce(0.1)- and Ag(0.06)-doped catalysts.
- The beneficial impact of blending the catalyst with PVDF (physical modification) on ozone decomposition performance at high humidity conditions highlighted the importance of the inhibition of interparticle water condensation.
- Leveraging both chemical and physical modification techniques an enhanced MnO_x-based catalyst was prepared and evaluated. This catalyst has the potential to be used in several applications, from face mask cartridges to aircraft cabins.

6.2. Future works

At the tropospheric level, ozone is generated through a series of reactions involving volatile organic compounds (VOCs) and NO_x. Therefore, the concentrations of these hazardous pollutants correlate. Especially in regions near traffic or downstream of wildfires, where the ozone concentration could be above the permissible limits, the levels of other pollutants could be high as well. Also, ozone has the capability to change air pollution chemistry. It is a strong oxidizer, and it can react with organic compounds containing carbon-carbon double bonds and produce secondary organic pollutants such as formaldehyde and acetaldehyde, which are known as carcinogens. Therefore, it is of utmost importance to study the performance of ozone removal media in the presence of other pollutants including VOCs, NO_x, and particulate matters.

Additionally, this study showed that water molecules play an important role in the ozone removal process of ACs and catalysts. Therefore, it recommended that the proposed empirical kinetic model be improved to include the humidity contribution in both ozone decomposition and media's deactivation. The statistical analyses revealed that the correlation between the operational

parameters and the removal efficiency of the materials is nonlinear. More investigations are suggested to improve the predictive regression model, which was obtained from the statistical studies.

An enhanced MnO_x-based catalyst was synthesized in this research leveraging chemical and physical modifications. One of the limitations of this work was the coating method. The amount of catalyst that was deposited on the Ni-foam filters was 1.36±0.11 mg/cm^2, and on average 0.14 g catalyst was deposited in total, which is remarkably lower than commercially fabricated filters. Ni-foam filter pressure drop is negligible; therefore, since coating process is a vast field of study and physical blending of the catalyst with a hydrophobic polymer add to the complexity, it is suggested to explore the coating procedures more profoundly and find the best method. Furthermore, the catalyst could be functionalized to become intrinsically hydrophobic. For instance, it is reported that fluorination converted the hydrophilic nature of graphite oxide to hydrophobic. Also, fabricating a highly porous composite mixed matrix media, benefiting the catalytic activity of the inorganic metal oxide and the hydrophobicity of the organic polymer could result in a humidity-resistant ozone decomposition media.

Several types of materials including ACs, metals, and metal oxides, were previously investigated for ozone decomposition, and their efficiency in various combinations of operational conditions at different scales were reported. Leveraging machine learning and artificial neural network methods could lead to recognizing the existing patterns and correlations, which could facilitate developing a predictive model for the ozone removal process.

Bibliography

[1] M. Marć, M. Śmiełowska, J. Namieśnik, and B. Zabiegała, "Indoor air quality of everyday use spaces dedicated to specific purposes---a review," *Environmental Science and Pollution Research*, vol. 25, pp. 2065–2082, Jan. 2018, doi: 10.1007/s11356-017-0839-8.

[2] S. Qin, L. Cheng, A. L. Selorm, and F. Yuan, "An overview of ozone research," *Journal of Advanced Oxidation Technologies*, vol. 21, 2018, doi: 10.26802/jaots.2017.0118.

[3] H. Karaca and Y. S. Velioglu, "Ozone applications in fruit and vegetable processing," *Food Reviews International*, vol. 23, pp. 91–106, 2007, doi: 10.1080/87559120600998221.

[4] S. Stucki, *Process Technologies for Water Treatment*, 1st ed. New York: Plenum Press, 1988.

[5] "Ozone Safe Work Practices," 2006.

[6] L. Varga and J. Szigeti, "Use of ozone in the dairy industry : A review," *Int J Dairy Technol*, vol. 69, pp. 157–168, 2016, doi: 10.1111/1471-0307.12302.

[7] A. A. Gonçalves, "Ozone – an Emerging Technology for the Seafood Industry," *Brazilian Archives of Biology and Thechnology*, vol. 52, pp. 1527–1539, 2009.

[8] M. Ondarts, J. Outin, L. Reinert, E. Gonze, and L. Duclaux, "Removal of ozone by activated carbons modified by oxidation treatments," *Eur Phys J Spec Top*, vol. 224, pp. 1995–1999, 2015, doi: 10.1140/epjst/e2015-02516-6.

[9] C. Subrahmanyam, D. A. Bulushev, and L. Kiwi-Minsker, "Dynamic behaviour of activated carbon catalysts during ozone decomposition at room temperature," *Appl Catal B*, vol. 61, pp. 98–106, 2005, doi: 10.1016/j.apcatb.2005.04.013.

[10] P. Lee and J. Davidson, "Evaluation of activated carbon filters for removal of ozone at the PPB level," *Am Ind Hyg Assoc J*, vol. 60, pp. 589–600, 1999, doi: 10.1080/00028899908984478.

[11] S. Yang, Z. Zhu, F. Wei, and X. Yang, "Carbon nanotubes / activated carbon fiber based air filter media for simultaneous removal of particulate matter and ozone," *Build Environ*, vol. 125, pp. 60–66, 2017, doi: 10.1016/j.buildenv.2017.08.040.

[12] S. Yang, J. Nie, F. Wei, and X. Yang, "Removal of ozone by carbon nanotubes/quartz fiber film," *Environ Sci Technol*, vol. 50, pp. 9592–9598, 2016, doi: 10.1021/acs.est.6b02563.

[13] C. Lee, L. Zhong, F. Haghighat, C. Coulthrust, and A. Bahloul, "Evaluation of ozone removal performance of ultraviolet photocatalytic oxidation air cleaning systems," in *ASHRAE Annual Conference*, 2016, pp. 1–9.

[14] I. S. H. Buchanan, M. J. Mendell, A. G. Mirer, and M. G. Apte, "Air filter materials, outdoor ozone and building-related symptoms in the BASE study," *Indoor Air*, vol. 18, pp. 144–155, 2008, doi: 10.1111/j.1600-0668.2008.00519.x.

[15] H. Destaillats *et al.*, "Secondary pollutants from ozone reactions with ventilation filters and degradation of filter media additives," *Atmos Environ*, vol. 45, pp. 3561–3568, 2011, doi: 10.1016/j.atmosenv.2011.03.066.

[16] A. Mills, S. K. Lee, and A. Lepre, "Photodecomposition of ozone sensitized by a film of titanium dioxide on glass," *J Photochem Photobiol A Chem*, vol. 155, no. 1–3, pp. 199–205, 2003, doi: 10.1016/S1010-6030(02)00388-X.

[17] Z. Lian, J. Ma, and H. He, “Decomposition of high-level ozone under high humidity over Mn-Fe catalyst: The influence of iron precursors,” *Catal Commun*, vol. 59, pp. 156–160, 2015, doi: 10.1016/j.catcom.2014.10.005.

[18] B. Dhandapani and S. T. Oyama, “Gas phase ozone decomposition catalysts,” *Appl Catal B*, vol. 11, pp. 129–166, 1997, doi: 10.1016/S0926-3373(96)00044-6.

[19] S. T. Oyama, “Chemical and catalytic properties of ozone,” *Catal Rev Sci Eng*, vol. 42, pp. 279–322, 2000, doi: 10.1081/CR-100100263.

[20] J.-Y. Gong, Y.-C. Chen, and K. Yu, “Photocatalytic decomposition of indoor ozone motivated by the white-light-emitting diode,” *Clean Technol Environ Policy*, vol. 19, pp. 2393–2404, 2017, doi: 10.1007/s10098-017-1427-9.

[21] K. Cho, K. Hwang, T. Sano, K. Takeuchi, and S. Matsuzawa, “Photocatalytic performance of Pt-loaded TiO2 in the decomposition of gaseous ozone,” *J Photochem Photobiol A Chem*, vol. 161, pp. 155–161, 2004, doi: 10.1016/S1010-6030(03)00287-9.

[22] Y. Lin and C. Lin, “Catalytic and photocatalytic degradation of ozone via utilization of controllable nano-Ag modified on TiO2,” *Environmental Progress*, vol. 27, pp. 496–502, 2008, doi: 10.1002/ep.

[23] P. Fu, P. Zhang, and J. Li, “Photocatalytic degradation of low concentration formaldehyde and simultaneous elimination of ozone by-product using palladium modified TiO2 films under UV254+185nm irradiation,” *Appl Catal B*, vol. 105, pp. 220–228, 2011, doi: 10.1016/j.apcatb.2011.04.021.

[24] J. Jia, P. Zhang, and L. Chen, “Catalytic decomposition of gaseous ozone over manganese dioxides with different crystal structures,” *Appl Catal B*, vol. 189, pp. 210–218, 2016, doi: 10.1016/j.apcatb.2016.02.055.

[25] Y. Liu and P. Zhang, “Catalytic decomposition of gaseous ozone over todorokite-type manganese dioxides at room temperature: Effects of cerium modification,” *Appl Catal A Gen*, vol. 530, pp. 102–110, 2017, doi: 10.1016/j.apcata.2016.11.028.

[26] M. Wang, P. Zhang, J. Li, and C. Jiang, “The effects of Mn loading on the structure and ozone decomposition activity of MnOx supported on activated carbon,” *Chinese Journal of Catalysis*, vol. 35, no. 3, pp. 335–341, 2014, doi: 10.1016/S1872-2067(12)60756-6.

[27] Y. U. Quanwei, Z. Ming, L. I. U. Zhimin, Z. Xiaoyu, Z. Lingmin, and C. Yaoqiang, “Catalytic decomposition of ozone in ground air by manganese-based monolith catalysts,” *Chinese Journal of Catalysis*, vol. 30, pp. 1–3, 2009, doi: 10.1016/S1872-2067(08)60082-0.

[28] J. Jia, P. Zhang, and L. Chen, “The effect of morphology of a-MnO2 on catalytic decomposition of gaseous ozone,” *Catal Sci Technol*, vol. 6, pp. 5841–5847, 2016, doi: 10.1039/C6CY00301J.

[29] T. Gopi *et al.*, “Catalytic decomposition of ozone on nanostructured potassium and proton containing δ-MnO2 catalysts,” *Catal Commun*, vol. 92, pp. 51–55, 2017, doi: 10.1016/j.catcom.2017.01.002.

[30] G. Zhu *et al.*, “Surface oxygen vacancy induced a-MnO 2 nanofiber for highly efficient ozone elimination,” *Appl Catal B*, vol. 209, pp. 729–737, 2017, doi: 10.1016/j.apcatb.2017.02.068.

[31] L. Li *et al.*, “Insight into the effect of oxygen vacancy concentration on the catalytic performance of MnO2,” *ACS Catal*, vol. 5, pp. 4825–4832, 2015, doi: 10.1021/acscatal.5b00320.

[32] C. Wang, J. Ma, F. Liu, H. He, and R. Zhang, “The effects of Mn2+ precursors on the structure and ozone decomposition activity of cryptomelane-type manganese oxide (OMS-2) catalysts,” *J Phys Chem*, vol. 119, pp. 23119–23126, 2015, doi: 10.1021/acs.jpcc.5b08095.

[33] Q. Yu *et al.*, “Influence of calcination temperature on the performance of Pd – Mn / SiO 2 – Al 2 O 3 catalysts for ozone decomposition,” *J Hazard Mater*, vol. 172, pp. 631–634, 2009, doi: 10.1016/j.jhazmat.2009.07.040.

[34] J. Jia, W. Yang, P. Zhang, and J. Zhang, “Facile synthesis of Fe-modified manganese oxide with high content of oxygen vacancies for efficient airborne ozone destruction,” *Appl Catal A Gen*, vol. 546, pp. 79–86, 2017, doi: 10.1016/j.apcata.2017.08.013.

[35] J. Ma, C. Wang, and H. He, “Transition metal doped cryptomelane-type manganese oxide catalysts for ozone decomposition,” *Appl Catal B*, vol. 201, pp. 503–510, 2017.

[36] I. Spasova, P. Nikolov, D. Mehandjiev, I. Spasova, P. Nikolov, and D. Mehandjiev, “Ozone decomposition over alumina-supported copper, manganese and copper-manganese catalysts,” *Ozone Sci Eng*, vol. 29, pp. 41–45, 2007, doi: 10.1080/01919510601111665.

[37] Y. Jiang *et al.*, “Influence of preparation temperature and acid treatment on the catalytic activity of MnO2,” *J Solid State Chem*, vol. 272, pp. 173–181, 2019, doi: 10.1016/j.jssc.2019.01.031.

[38] C. Jiang *et al.*, “Facile synthesis of activated carbon-supported porous manganese oxide via in situ reduction of permanganate for ozone decomposition,” *Ozone Sci Eng*, vol. 35, pp. 308–315, 2013, doi: 10.1080/01919512.2013.795854.

[39] J. Tatibouët, S. Valange, and H. Touati, “Near-ambient temperature ozone decomposition kinetics on manganese oxide-based catalysts,” *Appl Catal A Gen*, vol. 569, pp. 126–133, 2019, doi: 10.1016/j.apcata.2018.10.026.

[40] X. Li, J. Ma, L. Yang, G. He, C. Zhang, and R. Zhang, “Oxygen vacancies induced by transition metal doping in γ-MnO2 for highly efficient ozone decomposition,” *Environ Sci Technol*, vol. 52, pp. 12685–12696, 2018, doi: 10.1021/acs.est.8b04294.

[41] V. Bocci, “Physical-chemical properties of ozone- Natural production of Ozone: The toxicology of ozone,” in *Ozone*, Second.Springer Netherlands, 2011, pp. 1–4. doi: 10.1007/978-90-481-9234-2.

[42] M. L. Bell, A. Mcdermott, S. L. Zeger, and J. M. Samet, “Ozone and short term mortality in 95 US urban ccommunities , 1987-2000,” *Journal of American Medical Association*, vol. 292, pp. 2372–2378, 2004.

[43] M. Almeida-Silva, H. T. Wolterbeek, and S. M. Almeida, “Elderly exposure to indoor air pollutants,” *Atmos Environ*, vol. 85, pp. 54–63, 2014, doi: 10.1016/j.atmosenv.2013.11.061.

[44] G. E. Hatch, R. Slade, and J. McKee, “Fate of pathologically bound oxygen resulting from inhalation of labeled ozone in rats.,” *Environ Health Insights*, vol. 7, pp. 43–58, 2013, doi: 10.4137/EHI.S12673.

[45] R. J. Delfino, A. M. Murphy-Moulton, and M. R. Becklake, “Emergency room visits for respiratory illnesses among the elderly in Montreal: Association with low level ozone exposure,” *Environ Res*, vol. 76, pp. 67–77, 1998, doi: 10.1006/enrs.1997.3794.

[46] L. Zhong, C. S. Lee, and F. Haghighat, “Indoor ozone and climate change,” *Sustain Cities Soc*, vol. 28, pp. 466–472, 2017, doi: 10.1016/j.scs.2016.08.020.

[47] A. W. Nørgaard, J. D. Kudal, I. K. Koponen, and P. Wolkoff, “Ozone-initiated VOC and particle emissions from a cleaning agent and an air freshener : Risk assessment of acute airway effects,” *Environ Int*, vol. 68, pp. 209–218, 2014, doi: 10.1016/j.envint.2014.03.029.

[48] R. Barro, J. Regueiro, M. Llompart, and C. Garcia-jares, “Analysis of industrial contaminants in indoor air : Part 1 . Volatile organic compounds, carbonyl compounds, polycyclic aromatic hydrocarbons and polychlorinated biphenyls,” *J Chromatogr A*, vol. 1216, pp. 540–566, 2009, doi: 10.1016/j.chroma.2008.10.117.

[49] V. G. Mihucz and G. Záray, “Indoor air pollution,” *Comprehensive Analytical Chemistry*, vol. 73, pp. 45–71, 2016, doi: 10.1016/bs.coac.2016.02.003.

[50] A. Wisthaler *et al.*, “Products of ozone-initiated chemistry in a simulated aircraft environment,” *Environ Sci Technol*, vol. 39, pp. 4823–4832, 2005, doi: 10.1021/es047992j.

[51] Y. Takeuchi and T. Itoh, “Removal of ozone from air by activated carbon treatment,” *Separations Technology*, vol. 3, pp. 168–175, 1993, doi: 10.1016/0956-9618(93)80017-L.

[52] P. Krawczyk, “Effect of ozone treatment on properties of expanded graphite,” *Chemical Engineering Journal*, vol. 172, pp. 1096–1102, 2011, doi: 10.1016/j.cej.2011.06.005.

[53] A. S. Viner, P. A. Lawless, D. s. Ensor, and L. E. Sparks, “Ozone generation in dc-energized electrostatic precipitators,” *IEEE Trans Ind Appl*, vol. 28, pp. 504–512, 1992, doi: 10.1109/28.137427.

[54] F. Haghighat, C. S. Lee, B. Pant, G. Bolourani, N. Lakdawala, and A. Bastani, “Evaluation of various activated carbons for air cleaning - Towards design of immune and sustainable buildings,” *Atmos Environ*, vol. 42, pp. 8176–8184, 2008, doi: 10.1016/j.atmosenv.2008.07.061.

[55] C. J. Weschler, “New Directions : Ozone-initiated reaction products indoors may be more harmful than ozone itself,” *Atmos Environ*, vol. 38, pp. 5715–5716, 2004, doi: 10.1016/j.atmosenv.2004.08.001.

[56] C. J. Weschler, “Ozone’s impact on public health: Contributions from indoor exposures to ozone and products of ozone-initiated chemistry,” *Environ Health Perspect*, vol. 114, pp. 1489–1496, 2006, doi: 10.1289/ehp.9256.

[57] J. Zhang, P. Zhou, J. Liu, and J. Yu, "New understanding of the difference of photocatalytic activity among anatase, rutile and brookite TiO2," *Physical Chemistry Chemical Physics*, vol. 16, no. 38, pp. 20382–20386, 2014, doi: 10.1039/c4cp02201g.

[58] J. Kim, P. Zhang, J. Li, J. Wang, and P. Fu, "Photocatalytic degradation of gaseous toluene and ozone under UV 254+185 nm irradiation using a Pd-deposited TiO2 film," *Chemical Engineering Journal*, vol. 252, pp. 337–345, 2014, doi: 10.1016/j.cej.2014.05.015.

[59] Y. Lu, X. Zhao, M. Wang, Z. Yang, and X. Zhang, "Feasibility analysis on photocatalytic removal of gaseous ozone in aircraft cabins," *Build Environ*, vol. 81, pp. 42–50, 2014, doi: 10.1016/j.buildenv.2014.05.024.

[60] K. Yu and G. W. M. Lee, "Decomposition of gas-phase toluene by the combination of ozone and photocatalytic oxidation process (TiO 2 / UV , TiO 2 / UV / O 3 , and UV / O 3)," vol. 75, pp. 29–38, 2007, doi: 10.1016/j.apcatb.2007.03.006.

[61] J. Patzsch and J. Z. Bloh, "Improved photocatalytic ozone abatement over transition metal-grafted titanium dioxide," *Catal Today*, vol. 300, pp. 2–11, 2018, doi: 10.1016/j.cattod.2017.07.010.

[62] W. Li, G. V Gibbs, and S. T. Oyama, "Mechanism of ozone decomposition on a manganese oxide catalyst. 1. In situ raman spectroscopy and ab initio molecular orbital calculations," *Journal of American Chemical Society*, vol. 120, pp. 9041–9046, 1998.

[63] W. Li, G. V. Gibbs, and S. T. Oyama, "Mechanism of ozone decomposition on a manganese oxide catalyst. 2. Steady-state and transient kinetic studies," *J Am Chem Soc*, vol. 120, pp. 9047–9052, 1998, doi: 10.1021/ja981441+.

[64] J. Wang, J. Li, P. Zhang, and G. Zhang, "Understanding the 'seesaw effect' of interlayered K+ with different structure in manganese oxides for the enhanced formaldehyde oxidation," *Appl Catal B*, vol. 224, pp. 863–870, 2018, doi: 10.1016/j.apcatb.2017.11.019.

[65] G. Zhu *et al.*, "Tuning the K+ concentration in the tunnels of α-MnO2 to increase the content of oxygen vacancy for ozone elimination," *Environ Sci Technol*, vol. 52, pp. 8684–8692, 2018, doi: 10.1021/acs.est.8b01594.

[66] Y. Liu and P. Zhang, "Removing surface hydroxyl groups of Ce-modified MnO2 to significantly improve its stability for gaseous ozone decomposition," *J Phys Chem*, vol. 121, pp. 23488–23497, 2017, doi: 10.1021/acs.jpcc.7b07931.

[67] S. Gong, A. Wang, Y. Wang, H. Liu, N. Han, and Y. Chen, "Heterostructured Ni/NiO nanocatalysts for ozone decomposition," *ACS Appl Nano Mater*, vol. 3, pp. 597–607, 2020, doi: 10.1021/acsanm.9b02143.

[68] S. Gong, W. Li, and Y. Chen, "Low temperature decomposition of ozone by facilely synthesized cuprous oxide catalyst," *New Journal of Chemistry*, vol. 41, pp. 4828–4834, 2017, doi: 10.1039/C7NJ00253J.

[69] S. Gong, J. Chen, X. Wu, N. Han, and Y. Chen, "In-situ synthesis of Cu2O/reduced graphene oxide composite as effective catalyst for ozone decomposition," *Catal Commun*, vol. 106, pp. 25–29, 2018, doi: 10.1016/j.catcom.2017.12.003.

[70] S. Gong, A. Wang, J. Zhang, J. Guan, N. Han, and Y. Chen, “Gram-scale synthesis of ultra-fine Cu2O for highly efficient ozone decomposition,” *RCS Advances*, vol. 10, pp. 5212–5219, 2020, doi: 10.1039/c9ra09873a.

[71] T. Mathew, K. Suzuki, Y. Ikuta, Y. Nagai, N. Takahashi, and H. Shinjoh, “Mesoporous ferrihydrite-based iron oxide nanoparticles as highly promising materials for ozone removal,” *Angewandte Chemie*, vol. 123, pp. 7519–7522, 2011, doi: 10.1002/ange.201102007.

[72] H. Wang *et al.*, “An iron-containing metal – organic framework as a highly efficient catalyst for ozone decomposition,” *Angewandte Chemie*, vol. 130, pp. 16654–16658, 2018, doi: 10.1002/ange.201810268.

[73] J. Gascon, A. Corma, F. Kapteijn, and F. X. Llabrés I Xamena, “Metal organic framework catalysis: Quo vadis?,” *ACS Catal*, vol. 4, no. 2, pp. 361–378, 2014, doi: 10.1021/cs400959k.

[74] W. Tang *et al.*, “Higher oxidation state responsible for ozone decomposition at room temperature over manganese and cobalt oxides: Effect of calcination temperature,” *Ozone Sci Eng*, vol. 36, pp. 502–512, 2014, doi: 10.1080/01919512.2014.894454.

[75] Y. Ding, X. Zhang, L. Chen, X. Wang, N. Zhang, and Y. Liu, “Oxygen vacancies enabled enhancement of catalytic property of Al reduced anatase TiO2 in the decomposition of high concentration ozone,” *J Solid State Chem*, vol. 250, pp. 121–127, 2017, doi: 10.1016/j.jssc.2017.03.022.

[76] T. Batakliev *et al.*, “Ozone decomposition reaction over α -Alumina- supported silver catalyst : Comparative study of catalytic surface reactivity,” *Ozone Sci Eng*, vol. 37, pp. 216–220, 2015, doi: 10.1080/01919512.2014.957261.

[77] P. Nikolov *et al.*, “Ozone decomposition on Ag/SiO2 and Ag/clinoptilolite catalysts at ambient temperature,” *J Hazard Mater*, vol. 184, no. 1–3, pp. 16–19, 2010, doi: 10.1016/j.jhazmat.2010.07.056.

[78] N. Kumar *et al.*, “Ag-modified H-Beta , H-MCM-41 and SiO2: Influence of support, acidity and Ag content in ozone decomposition at ambient temperature,” *Catal Today*, vol. 119, pp. 342–346, 2007, doi: 10.1016/j.cattod.2006.08.048.

[79] N. Kumar, P. M. Konova, A. Naydenov, T. Heikilla, T. Salmi, and D. Y. Murzin, “Synthesis of novel Ag modified MCM-41 mesoporous molecular sieve and beta zeolite catalysts for ozone decomposition at ambient temperature,” *Catal Letters*, vol. 98, pp. 57–60, 2004.

[80] V. Blaskov *et al.*, “Synthesis and catalytic activity of silver-coated perlite in the reaction of ozone decomposition,” *Ozone Sci Eng*, vol. 37, pp. 252–256, 2015, doi: 10.1080/01919512.2014.983453.

[81] E. F. Mohamed, G. Awad, H. Zaitan, C. Andriantsiferana, and M. Manero, “Transition metals-incorporated zeolites as environmental catalysts for indoor air ozone decomposition,” *Environ Technol*, vol. 0, no. 0, pp. 1–9, 2017, doi: 10.1080/09593330.2017.1315457.

[82] H. Valdés, S. Alejandro, and C. A. Zaror, “Natural zeolite reactivity towards ozone : The role of compensating cations,” *J Hazard Mater*, vol. 227–228, pp. 34–40, 2012, doi: 10.1016/j.jhazmat.2012.04.067.

[83] S. Alejandro, H. Valdés, and C. A. Zaror, “Natural zeolite reactivity towards ozone : The role of acid surface sites,” *Journal of Advanced Oxidation Technologies*, vol. 14, 2011, doi: 10.1515/jaots-2011-0201.

[84] X. Li *et al.*, “Etched p-type Si nanowires for efficient ozone decomposition,” *Nanoscale Res Lett*, vol. 14, pp. 10–14, 2019, doi: 10.1186/s11671-019-3205-6.

[85] Y. Wang, H. Arandiyan, and J. Scott, “Recent advances in ordered meso / macroporous metal oxides for heterogeneous catalysis : a review,” *J Mater Chem A Mater*, vol. 5, pp. 8825–8846, 2017, doi: 10.1039/C6TA10896B.

[86] J. E. Post, “Manganese oxide minerals: Crystal structures and economic and,” *PNAS*, vol. 96, pp. 3447–3454, 1999.

[87] Y. Rao, D. Zeng, X. Cao, G. Qin, and S. Li, “Synthesis of doped MnOx/diatomite composites for catalyzing ozone decomposition,” *Ceram Int*, vol. 45, no. 6, pp. 6966–6971, 2019, doi: 10.1016/j.ceramint.2018.12.195.

[88] M. Sun *et al.*, “Enhanced catalytic performance by oxygen vacancy and active interface originated from facile reduction of OMS-2,” *Chemical Engineering Journal*, vol. 331, no. May 2017, pp. 626–635, 2018, doi: 10.1016/j.cej.2017.09.028.

[89] B. Peng *et al.*, “Highly active OMS-2 for catalytic ozone decomposition under humid conditions,” *Pet Sci*, vol. 16, no. 4, pp. 912–919, 2019, doi: 10.1007/s12182-019-0335-5.

[90] D. A. Tompsett, S. C. Parker, and M. S. Islam, “Rutile (β-)MnO2 surfaces and vacancy formation for high electrochemical and catalytic performance,” *J Am Chem Soc*, vol. 136, no. 4, pp. 1418–1426, 2014, doi: 10.1021/ja4092962.

[91] Y. Chen, W. Qu, C. Li, J. Chen, Z. Ma, and X. Tang, “Ultra-low-temperature ozone abatement on α-MnO2(001) facets with down-shifted lowest unoccupied orbitals,” *Ind Eng Chem Res*, vol. 57, pp. 12590–12594, 2018, doi: 10.1021/acs.iecr.8b03491.

[92] S. Rong, P. Zhang, F. Liu, and Y. Yang, “Engineering crystal facet of α-MnO2 nanowire for highly efficient catalytic oxidation of carcinogenic airborne formaldehyde,” *ACS Catal*, vol. 8, pp. 3435–3446, 2018, doi: 10.1021/acscatal.8b00456.

[93] Y. Yang, P. Zhang, and J. Jia, “Vanadium-doped MnO2 for efficient room-temperature catalytic decomposition of ozone in air,” *Appl Surf Sci*, vol. 484, no. January, pp. 45–53, 2019, doi: 10.1016/j.apsusc.2019.04.084.

[94] L. Wang *et al.*, “Highly eficient vacancy-driven photothermal therapy mediated by ultrathin MnO2 nanosheets,” *Applied Materials & Interfaces*, vol. 11, pp. 6267–6275, 2019, doi: 10.1021/acsami.8b20639.

[95] Y. Liu, W. Yang, P. Zhang, and J. Zhang, “Nitric acid-treated birnessite-type MnO2: An efficient and hydrophobic material for humid ozone decomposition,” *Appl Surf Sci*, vol. 442, pp. 640–649, 2018, doi: 10.1016/j.apsusc.2018.02.204.

[96] J. Liu *et al.*, “Experimental and theoretical investigation of mesoporous MnO2 nanosheets with oxygen vacancies for high-efficiency catalytic DeNOx,” *ACS Catal*, vol. 8, pp. 3865–3874, 2018, doi: 10.1021/acscatal.8b00267.

[97] T. Lin, L. Yu, M. Sun, G. Cheng, B. Lan, and Z. Fu, “Mesoporous a-MnO2 microspheres with high specific surface area: Controlled synthesis and catalytic activities,” *Chemical Engineering Journal*, vol. 286, pp. 114–121, 2016, doi: 10.1016/j.cej.2015.09.024.

[98] S. Birgisson, D. Saha, and B. B. Iversen, “Formation mechanisms of nanocrystalline MnO2 polymorphs under hydrothermal conditions,” *Cryst Growth Des*, vol. 18, pp. 827–838, 2018, doi: 10.1021/acs.cgd.7b01304.

[99] Y. Xu, J. Huang, S. Yang, J. Wang, W. Chen, and Y. Chen, “Crystalline-phase-dependent catalytic performance of MnO2 for oxidation reactions,” *Sci China Mater*, vol. 60, pp. 1196–1204, 2017.

[100] J. Wang, J. Li, C. Jiang, P. Zhou, P. Zhang, and J. Yu, “The effect of manganese vacancy in birnessite-type MnO2 on room-temperature oxidation of formaldehyde in air,” *Appl Catal B*, vol. 204, pp. 147–155, 2017, doi: 10.1016/j.apcatb.2016.11.036.

[101] S. Liu, J. Ji, Y. Yu, and H. Huang, “Facile synthesi of amorphous mesoporous manganese oxides for efficient catalytic decomposition of ozone,” *Catal Sci Technol*, vol. 8, pp. 4264–4273, 2018, doi: 10.1039/C8CY01111G.

[102] Y. Yu, S. Liu, J. Ji, and H. Huang, “Amorphous MnO2 surviving calcination: an efficient catalyst for ozone decomposition,” *Catal Sci Technol*, vol. 9, pp. 5090–5099, 2019, doi: 10.1039/c9cy01426h.

[103] J. Jia and P. Zhang, “Catalytic decomposition of airborne ozone by MnCO3 and its mechanism,” *Ozone Sci Eng*, vol. 40, pp. 21–28, 2018, doi: 10.1080/01919512.2017.1328272.

[104] Y. Yang, J. Jia, Y. Liu, and P. Zhang, “The effect of tungsten doping on the catalytic activity of α -MnO 2 nanomaterial for ozone decomposition under humid condition,” *Appl Catal A Gen*, vol. 562, pp. 132–141, 2018, doi: 10.1016/j.apcata.2018.06.006.

[105] C. H. Chen *et al.*, “Structural distortion of molybdenum-doped manganese oxide octahedral molecular sieves for enhanced catalytic performance,” *Inorg Chem*, vol. 54, pp. 10163–10171, 2015, doi: 10.1021/acs.inorgchem.5b00906.

[106] A. R. Puigdollers, P. Schlexer, S. Tosoni, and G. Pacchioni, “Increasing oxide reducibility: The role of metal/oxide interfaces in the formation of oxygen vacancies,” *ACS Catal*, vol. 7, pp. 6493–6513, 2017.

[107] X. Chen, Z. Zhao, S. Liu, J. Huang, J. Xie, and Y. Zhou, “Ce-Fe-Mn ternary mixed-oxide catalysts for catalytic decomposition of ozone at ambient temperatures,” *Journal of Rare Earths*, vol. 38, pp. 175–181, 2020, doi: 10.1016/j.jre.2019.01.010.

[108] R. Cao, P. Zhang, Y. Liu, and X. Zheng, “Ammonium-treated birnessite-type MnO2 to increase oxygen vacancies and surface acidity for stably decomposing ozone in humid condition,” *Appl Surf Sci*, vol. 495, p. 143607, 2019, doi: 10.1016/j.apsusc.2019.143607.

[109] R. Radhakrishnan, S. T. Oyama, J. G. Chen, and K. Asakura, “Electron transfer effects in ozone decomposition on supported manganese oxide,” *Journal of Physical Chemistry B*, vol. 105, no. 19, pp. 4245–4253, 2001, doi: 10.1021/jp003246z.

[110] L. Tao, G. Zhao, P. Chen, Z. Zhang, and Y. Liu, “High-performance Co-MnOx composite oxide catalyst structured onto Al-fiber felt for high-throughput O3 decomposition,” *ChemCatChem*, vol. 11, pp. 1131–1142, 2019, doi: 10.1002/cctc.201801401.

[111] Y. Yu *et al.*, “Activated carbon supported MnO nanoparticles for efficient ozone decomposition at room temperature,” *Catal Today*, vol. 355, pp. 573–579, 2020, doi: 10.1016/j.cattod.2019.05.063.

[112] M. Kim, E. Park, and J. Jurng, “Oxidation of gaseous formaldehyde with ozone over MnOx/TiO2 catalysts at room temperature (25°C),” *Powder Technol*, vol. 325, pp. 368–372, 2018, doi: 10.1016/j.powtec.2017.10.031.

[113] J. Ji, Y. Fang, L. He, and H. Huang, “Efficient catalytic removal of airborne ozone under ambient conditions over manganese oxides immobolized on carbon nanotubes,” *Catal Sci Technol*, vol. 9, pp. 4036–4046, 2019, doi: 10.1039/c9cy00762h.

[114] X. Li, J. Ma, C. Zhang, R. Zhang, and H. He, “Detrimental role of residual surface acid ions on ozone decomposition over Ce-modified g-MnO2 under humid conditions,” *Journal of Environmental Sciences*, vol. 91, pp. 43–53, 2020, doi: 10.1016/j.jes.2019.12.004.

[115] L. Yang, J. Ma, X. Li, C. Zhang, and H. He, “Enhancing oxygen vacancies of Ce-OMS -2 via optimized hydrothermal conditions to improve catalytic ozone decomposition,” *Ind Eng Chem Res*, vol. 59, pp. 118–128, 2020, doi: 10.1021/acs.iecr.9b05967.

[116] L. Yang, J. Ma, X. Li, G. He, C. Zhang, and H. He, “Tuning the fill percentage in the hydrothermal synthesis process to increase catalyst performance for ozone decomposition,” *Journal of Environmental Sciences*, vol. 87, pp. 60–70, 2019, doi: 10.1016/j.jes.2019.06.007.

[117] W. Hong, T. Zhu, Y. Sun, H. Wang, X. Li, and F. Shen, “Enhancing oxygen vacancies by introducing Na+ into OMS-2 tunnels to promote catalytic ozone decomposition,” *Environ Sci Technol*, vol. 53, pp. 13332–13343, 2019, doi: 10.1021/acs.est.9b03689.

[118] J. Ma, X. Li, C. Zhang, and Q. Ma, “Novel CeMnaOx catalyst for highly efficient catalytic decomposition of ozone,” *Appl Catal B*, vol. 264, pp. 118498–118507, 2020, doi: 10.1016/j.apcatb.2019.118498.

[119] L. Li, P. Zhang, and R. Cao, “Porous manganese oxides synthesized with natural products at room temperature: a superior humidity-tolerant catalyst for ozone decomposition,” *Catal Sci Technol*, vol. 10, pp. 2254–2267, 2020, doi: 10.1039/d0cy00196a.

[120] X. Li, J. Ma, C. Zhang, R. Zhang, and H. He, “Facile synthesis of Ag-modified manganese oxide for effective catalytic ozone decomposition,” *Journal of Environmental Sciences*, vol. 80, pp. 159–168, 2019, doi: 10.1016/j.jes.2018.12.008.

[121] D. B. Day *et al.*, “Association of ozone exposure with cardiorespiratory pathophysiologic mechanisms in healthy adults,” *JAMA Intern Med*, vol. 177, no. 9, pp. 1344–1353, 2017, doi: 10.1001/jamainternmed.2017.2842.

[122] C. J. Weschler, H. C. Shields, and D. V. Naik, “Indoor ozone exposures,” *J Air Waste Manage Assoc*, vol. 39, no. 12, pp. 1562–1568, 1989, doi: 10.1080/08940630.1989.10466650.

[123] C. J. Weschler, “Ozone in indoor environments: Concentration and chemistry,” *Indoor Air*, vol. 10, no. 4, pp. 269–288, 2000, doi: 10.1034/j.1600-0668.2000.010004269.x.

[124] M. G. Khararoodi, C. S. Lee, and F. Haghighat, “Modelling of sorbent-based gas filters for indoor environment: A comprehensive review,” *Build Environ*, vol. 208, p. 108579, Jan. 2022, doi: 10.1016/J.BUILDENV.2021.108579.

[125] A. Wisthaler and C. J. Weschler, “Reactions of ozone with human skin lipids : Sources of carbonyls , dicarbonyls , and hydroxycarbonyls in indoor air,” *PNAS*, vol. 107, pp. 6568–6575, 2010, doi: 10.1073/pnas.0904498106.

[126] “Ocupational Safety and Health Administration.” https://www.osha.gov/chemicaldata/9

[127] M. Namdari, C.-S. Lee, and F. Haghighat, “Active ozone removal technologies for a safe indoor environment: A comprehensive review,” *Build Environ*, vol. 187, p. 107370, 2021, doi: 10.1016/j.buildenv.2020.107370.

[128] A. Draou, S. Nemmich, K. Nassour, and Y. Benmimoun, “Experimental analysis of a novel ozone generator configuration for use in water treatment applications,” *International Journal of Environmental Studies*, pp. 1–13, 2018, doi: 10.1080/00207233.2018.1499698.

[129] B. L. Loeb *et al.*, “Worldwide ozone capacity for treatment of drinking water and wastewater : A review,” *Ozone Sci Eng*, vol. 34, pp. 64–77, 2012, doi: 10.1080/01919512.2012.640251.

[130] B. D. Lachenal, G. Pipon, and C. Chirat, “Final pulp bleaching by ozonation: Chemical justification and practical operating conditions,” *Pulp and Paper Canada*, vol. 107, pp. 31–34, 2006.

[131] R. J. Farrauto and J. N. Armor, “Moving from discovery to real applications for your catalyst,” *Appl Catal A Gen*, vol. 527, pp. 182–189, 2016, doi: 10.1016/j.apcata.2016.09.008.

[132] F. Wu, M. Wang, Y. Lu, X. Zhang, and C. Yang, “Catalytic removal of ozone and design of an ozone converter for the bleeding air purification of aircraft cabin,” *Build Environ*, vol. 115, pp. 25–33, 2017, doi: 10.1016/j.buildenv.2017.01.007.

[133] S. Bhangar, S. C. Cowlin, B. C. Singer, R. G. Sextro, and W. W. Nazaroff, “Ozone levels in passenger cabins of commercial aircraft on North American and transoceanic routes,” *Environ Sci Technol*, vol. 42, no. 11, pp. 3938–3943, 2008, doi: 10.1021/es702967k.

[134] M. Bahri and F. Haghighat, “Plasma-based indoor air cleaning technologies: The state of the art-review,” *Clean (Weinh)*, vol. 42, pp. 1667–1680, 2014, doi: 10.1002/clen.201300296.

[135] M. Tang, “Ozone Removal Tests for Activated Carbon Filters,” *ASHRAE Trans*, vol. 126, pp. 467–475, 2020.

[136] W. J. Fisk, M. Spears, D. P. Sullivan, and M. Mendell, “Ozone removal by filters containing activated carbon : a pilot study,” in *Healthy Buildings*, Syracus, 2009.

[137] C. O. Muller *et al.*, "ANSI/ASHRAE STANDARD 145.1-2015 Laboratory Test Method for Assessing the Performance of Gas-Phase Air-Cleaning Systems : Loose Granular Media," 2015.

[138] S. Brunauer, P. H. Emmett, and E. Teller, "Adsorption of Gases in Multimolecular Layers," *Journal of American Chemical Society*, vol. 60, no. 2, pp. 309–319, 1938.

[139] J. H. de Boer, B. C. Lippens, B. G. Linsen, J. C. P. Broekhoff, A. van den Heuvel, and T. J. Osinga, "The t-Curve of Multimolecular N2-Adsorption," *J Colloid Interface Sci*, vol. 21, no. 4, pp. 405–414, 1966, doi: 10.1016/0095-8522(66)90006-7.

[140] K. Han, J. S. Zhang, B. Guo, and C. He, "Laboratory comparison of relative performance of gas phase filtration media at high and low O 3/NO 2 challenge concentrations (ASHRAE RP-1557)," *HVAC and R Research*, vol. 20, no. 5, pp. 522–531, 2014, doi: 10.1080/10789669.2014.908691.

[141] H. Valdés, M. Sánchez-Polo, J. Rivera-Utrilla, and C. A. Zaror, "Effect of ozone treatment on surface properties of activated carbon," *Langmuir*, vol. 18, no. 6, pp. 2111–2116, 2002, doi: 10.1021/la010920a.

[142] R. Hilton, P. Bick, A. Tekeei, E. Leimkuehler, P. Pfeifer, and G. J. Suppes, "Mass balance and performance analysis of potassium hydroxide activated carbon," *Ind Eng Chem Res*, vol. 51, no. 26, pp. 9129–9135, 2012, doi: 10.1021/ie301293t.

[143] Y. W. Lee, D. K. Choi, and J. W. Park, "Surface chemical characterization using AES/SAM and ToF-SIMS on KOH-impregnated activated carbon by selective adsorption of NOx," *Ind Eng Chem Res*, vol. 40, no. 15, pp. 3337–3345, 2001, doi: 10.1021/ie001068q.

[144] Y. W. Lee, H. J. Kim, J. W. Park, B. U. Choi, D. K. Choi, and J. W. Park, "Adsorption and reaction behavior for the simultaneous adsorption of NO-NO2 and SO2 on activated carbon impregnated with KOH," *Carbon N Y*, vol. 41, no. 10, pp. 1881–1888, 2003, doi: 10.1016/S0008-6223(03)00105-2.

[145] L. Forni, D. Bahnemann, and E. J. Hart, "Mechanism of the hydroxide ion initiated decomposition of ozone in aqueous solution," *Journal of Physical Chemistry*, vol. 86, no. 2, pp. 255–259, 1982, doi: 10.1021/j100391a025.

[146] G. Merényi, J. Lind, S. Naumov, and C. Von Sonntag, "The reaction of ozone with the hydroxide ion: Mechanistic considerations based on thermokinetic and quantum chemical calculations and the role of HO 4- in superoxide dismutation," *Chemistry - A European Journal*, vol. 16, no. 4, pp. 1372–1377, 2010, doi: 10.1002/chem.200802539.

[147] K. Han, J. S. Zhang, B. Guo, and C. He, "Laboratory comparison of relative performance of gas phase filtration media at high and low O 3/NO 2 challenge concentrations (ASHRAE RP-1557)," *HVAC and R Research*, vol. 20, no. 5, pp. 522–531, 2014, doi: 10.1080/10789669.2014.908691.

[148] "https://reptox.cnesst.gouv.qc.ca/Pages/fiche-complete.aspx?no_produit=2006," *CNESST*.

[149] M. Ghasemi, F. Haghighat, C.-S. Lee, and M. Namdari, "The Effect of VOC and Environmental Parameters on Ozone Sensors Performance," vol. (submitted, 2023.

[150] “Ozone Generation Market Forecasts to 2028 – Global Analysis By Technology (Cold Plasma, Corona Discharge), Application (Potable Water Treatment, Medicine), End User (Commercial, Industrial) and By Geography,” *MRC Statistics*, 2022. https://www.strategymrc.com/report/ozone-generation-market

[151] M. Namdari, C. S. Lee, F. Haghighat, A. Bahloul, and M. Huard, “Reviewing MnO x -based catalysts for decomposition of indoor ozone,” *IOP Conf Ser Mater Sci Eng*, vol. 609, p. 042079, Oct. 2019, doi: 10.1088/1757-899X/609/4/042079.

[152] J. S. Kiurski, B. B. Marić, S. M. Aksentijević, I. B. Oros, and V. S. Kecić, “Occupational Hazards in Printing Industry,” *International Journal of Environmental Science and Technology*, vol. 13, pp. 955–972, 2016, doi: 10.1007/s13762-016-0937-z.

[153] V. Valuntaite, R. Chadysiene, R. Girgzdiene, and A. Girgzdys, “Variation of Ozone Concentration and UV Radiation Intensity During Welding Process,” in *The 7th international Conference Environmental Engineering*, Vilnius, 2008, pp. 22–23.

[154] T. N. McManus and A. N. Haddad, “Ozone: a critical contaminant produced during gas metal arc welding (GMAW) on aluminum alloys—resolving the short- versus long-duration sampling discrepancy,” *Air Qual Atmos Health*, vol. 12, pp. 97–106, 2019, doi: 10.1007/s11869-018-0634-9.

[155] A. C. Olin *et al.*, “Respiratory health among bleachery workers exposed to ozone and chlorine dioxide,” *Scand J Work Environ Health*, vol. 28, pp. 117–123, 2002, doi: 10.5271/sjweh.655.

[156] C. Millet, D. N. Nguyen, L. Lépine, M. Bélec, D. Lessard-Déziel, and C. Guddemi, “Case study - High Ozone Concentration in Hydro Generators,” in *2009 IEEE Electrical Insulation Conference*, Montreal, 2009, pp. 178–182. doi: 10.1109/EIC.2009.5166340.

[157] S. I. V. Sousa, M. C. M. Alvim-Ferraz, F. G. Martins, and M. C. Pereira, “Ozone Exposure and Its Influence on the Worsening of Childhood Asthma,” *Allergy: European Journal of Allergy and Clinical Immunology*, vol. 64, pp. 1046–1055, 2009, doi: 10.1111/j.1398-9995.2009.01946.x.

[158] S. I. V. Sousa, C. Ferraz, M. C. M. Alvim-Ferraz, F. G. Martins, L. G. Vaz, and M. C. Pereira, “Spirometric Tests to Assess the Prevalence of Childhood Asthma at Portuguese Rural Areas: Influence of Exposure to High Ozone Levels,” *Environ Int*, vol. 37, no. 2, pp. 474–478, 2011, doi: 10.1016/j.envint.2010.11.014.

[159] Y. Ma, S. Yang, J. Zhou, Z. Yu, and J. Zhou, “Effect of Ambient Air Pollution on Emergency Room Admissions for Respiratory Diseases in Beijing, China,” *Atmos Environ*, vol. 191, no. December 2017, pp. 320–327, 2018, doi: 10.1016/j.atmosenv.2018.08.027.

[160] R. T. Brunett *et al.*, “Effects of Low Ambient Levels of Ozone and Sulfates on the Frequency of Respiratory Admissons to Ontario Hospitals,” *Environ Res*, vol. 65, pp. 172–194, 1994.

[161] S. R. Arnold *et al.*, “Simulated Global Climate Response to Tropospheric Ozone-Induced Changes in Plant Transpiration,” *Geophys Res Lett*, vol. 45, pp. 13070–13079, 2018, doi: 10.1029/2018GL079938.

[162] M. Namdari, C. Lee, and F. Haghighat, "A Systematic Comparative Study of Granular Activated Carbons and Catalysts for Ozone Removal," *Build Environ*, vol. 224, p. 109510, 2022, doi: 10.1016/j.buildenv.2022.109510.
[163] D. C. Montgomery, *Design and Analysis of Experiments*, 5th Editio. John Wiley and Sons.
[164] S. H. Chang, T. T. Teng, and N. Ismail, "Screening of factors influencing Cu(II) extraction by soybean oil-based organic solvents using fractional factorial design," *J Environ Manage*, vol. 92, no. 10, pp. 2580–2585, 2011, doi: 10.1016/j.jenvman.2011.05.025.
[165] M. S. Elazazy, A. A. Issa, M. Al-Mashreky, M. Al-Sulaiti, and K. Al-Saad, "Application of fractional factorial design for green synthesis of cyano-modified silica nanoparticles: Chemometrics and multifarious response optimization," *Advanced Powder Technology*, vol. 29, no. 5, pp. 1204–1215, 2018, doi: 10.1016/j.apt.2018.02.012.
[166] Y. Chen, C. J. Lin, G. Jones, S. Fu, and H. Zhan, "Enhancing biodegradation of wastewater by microbial consortia with fractional factorial design," *J Hazard Mater*, vol. 171, no. 1–3, pp. 948–953, 2009, doi: 10.1016/j.jhazmat.2009.06.100.
[167] S. B. K. Kouachi, S. B. Bacha, and G. L. A. Soualah, "Kinetic study of methyl orange decolorization by the Fenton process based on fractional factorial design," *Reaction Kinetics, Mechanisms and Catalysis*, vol. 130, no. 2, pp. 1123–1140, 2020, doi: 10.1007/s11144-020-01803-x.
[168] K. Al-saad, M. El-azazy, A. A. Issa, A. Al-yafie, and A. S. El-shafie, "Recycling of Date Pits Into a Green Adsorbent for Removal of Heavy Metals : A Fractional Factorial Design-Based Approach," *Front Chem*, vol. 7, pp. 1–16, 2019, doi: 10.3389/fchem.2019.00552.
[169] M. S. Secula, I. Cretescu, B. Cagnon, L. R. Manea, C. S. Stan, and I. G. Breaban, "Fractional Factorial Design Study on the Performance of GAC-Enhanced Electrocoagulation Process Involved in Color Removal from Dye Solutions," *Materials*, vol. 6, pp. 2723–2746, 2013, doi: 10.3390/ma6072723.
[170] D. Zhang, R. Wang, and X. Yang, "Application of fractional factorial design to ZSM-5 synthesis using ethanol as template," *Microporous and Mesoporous Materials*, vol. 126, no. 1–2, pp. 8–13, 2009, doi: 10.1016/j.micromeso.2009.03.015.
[171] T. T. Allen, *Introduction to engineering statistics and lean six sigma: Statistical quality control and design of experiments and systems*. 2018. doi: 10.1007/978-1-4471-7420-2.
[172] H. S. Fogler, *Elements of Chemical Reaction Engineering*, 5th ed. Philadelphia, PA: Prentice Hall, 2016.
[173] M. G. Khararoodi, F. Haghighat, and C. S. Lee, "Removal of indoor air ozone using carbon-based filters: Systematic development and validation of a predictive model," *Build Environ*, vol. 219, no. May, p. 109157, 2022, doi: 10.1016/j.buildenv.2022.109157.
[174] M. Malayeri, F. Haghighat, and C. S. Lee, "Modeling of volatile organic compounds degradation by photocatalytic oxidation reactor in indoor air: A review," *Build Environ*, vol. 154, no. January, pp. 309–323, 2019, doi: 10.1016/j.buildenv.2019.02.023.

[175] J. Von Seckendorff, P. Scheck, M. Tonigold, and R. Fischer, “Numerical Shape Development Study in View of Random Packed Beds – The Yo-Yo Shape,” *Chemical Engineering Journal*, vol. 404, p. 126468, 2021, doi: 10.1016/j.cej.2020.126468.

[176] I. I. Laskar, Z. Hashisho, J. H. Phillips, J. E. Anderson, and M. Nichols, “Competitive Adsorption Equilibrium Modeling of Volatile Organic Compound (VOC) and Water Vapor onto Activated Carbon,” *Sep Purif Technol*, vol. 212, pp. 632–640, 2019, doi: 10.1016/j.seppur.2018.11.073.

[177] N. Qi and M. D. Levan, “Adsorption Equilibrium Modeling for Water on Activated Carbons,” *Carbon N Y*, vol. 43, pp. 2258–2263, 2005, doi: 10.1016/j.carbon.2005.03.040.

[178] N. Wakao and T. Funazkri, “Effect of Fluid Dispersion Coefficients on Particle-to-Fluid Mass Transfer Coefficients in Packed beds Correlation of Sherwood Numbers,” *Chem Eng Sci*, vol. 33, pp. 1375–1384, 1978, doi: 10.1016/0009-2509(78)85120-3.

[179] J. J. Zhang, Y. Wei, and Z. Fang, “Ozone pollution: A major health hazard worldwide,” *Frontiers in Immunology*, vol. 10, no. OCT. Frontiers Media S.A., 2019. doi: 10.3389/fimmu.2019.02518.

[180] E. I. Epelle *et al.*, “Ozone application in different industries: A review of recent developments,” *Chemical Engineering Journal*, vol. 454. Elsevier B.V., Feb. 15, 2023. doi: 10.1016/j.cej.2022.140188.

[181] M. B. Rice, T. L. Guidotti, and K. R. Cromar, “Scientific Evidence Supports Stronger Limits on Ozone,” *Am J Respir Crit Care Med*, vol. 191, pp. 501–503, 2015.

[182] M. Lippmann, “Health Effects Of Ozone A Critical Review,” *J Air Pollut Control Assoc*, vol. 39, pp. 672–695, May 1989, doi: 10.1080/08940630.1989.10466554.

[183] WHO, “Health Aspects of Air Pollution with Particulate Matter, Ozone and Nitrogen Dioxide,” *Report on a WHO Working Group Bonn, Germany 13–15 January 2003*, no. January, p. 98, 2003, doi: 10.2105/AJPH.48.7.913.

[184] “Powered Air Purifier Respirator Market 2022-2028,” *Research and Markets*, Jan. 2023. https://www.researchandmarkets.com/reports/5734828/powered-air-purifier-respirator-market#rela4-5716716 (accessed Apr. 12, 2023).

[185] M. Namdari, C. S. Lee, and F. Haghighat, “The effect of operational conditions on the performance of granular ozone removal media: Statistical experimental design and kinetic modeling,” *Build Environ*, vol. 235, May 2023, doi: 10.1016/j.buildenv.2023.110216.

[186] M. Tang, J. A. Siegel, R. L. Corsi, and A. Novoselac, “Evaluation of ozone removal devices applied in ventilation systems,” *Build Environ*, vol. 225, Nov. 2022, doi: 10.1016/j.buildenv.2022.109582.

[187] H. Xu *et al.*, “Gaseous Heterogeneous Catalytic Reactions over Mn-Based Oxides for Environmental Applications: A Critical Review,” *Environmental Science and Technology*, vol. 51, no. 16. American Chemical Society, pp. 8879–8892, Aug. 15, 2017. doi: 10.1021/acs.est.6b06079.

[188] L. Zhang, S. Wang, L. Lv, Y. Ding, D. Tian, and S. Wang, “Insights into the Reactive and Deactivation Mechanisms of Manganese Oxides for Ozone Elimination: The Roles of

Surface Oxygen Species," *Langmuir*, vol. 37, no. 4, pp. 1410–1419, Feb. 2021, doi: 10.1021/acs.langmuir.0c02841.

[189] R. Yang *et al.*, "MnO2-Based Materials for Environmental Applications," *Advanced Materials*, vol. 33, no. 9. Wiley-VCH Verlag, Mar. 01, 2021. doi: 10.1002/adma.202004862.

[190] C. Peng, D. Yu, L. Wang, X. Yu, and Z. Zhao, "Recent advances in the preparation and catalytic performance of Mn-based oxide catalysts with special morphologies for the removal of air pollutants," *Journal of Materials Chemistry A*, vol. 9, no. 22. Royal Society of Chemistry, pp. 12947–12980, Jun. 14, 2021. doi: 10.1039/d1ta00911g.

[191] I. Y. Kim, H. Ha, T. W. Kim, Y. Paik, J. Choy, and S. Hwang, "Origin of improved electrochemical activity of B-MnO2 nanorods: Effect of the Mn valence in the precursor on the crystal structure and electrode activity of manganates," *Journal of Physical Chemistry C*, vol. 113, pp. 21274–21282, 2009.

[192] S. Gong, Z. Xie, W. Li, X. Wu, N. Han, and Y. Chen, "Highly active and humidity resistive perovskite LaFeO3 based catalysts for efficient ozone decomposition," *Appl Catal B*, vol. 241, pp. 578–587, 2019, doi: 10.1016/j.apcatb.2018.09.041.

[193] E. P. Barrett, L. G. Joyner, and P. P. Halenda, "The Determination of Pore and Area Distribution in Porous Substances. I. Computations from Nitrogen Isotherms," *J Am Chem Soc*, vol. 73, pp. 373–380, 1951.

[194] F. Neese, "The ORCA program system," *Wiley Interdiscip Rev Comput Mol Sci*, vol. 2, no. 1, pp. 73–78, Jan. 2012, doi: 10.1002/wcms.81.

[195] M. Khavani, A. Mehranfar, and M. R. K. Mofrad, "Effects of Ionic Liquids on the Stabilization Process of Gold Nanoparticles," *Journal of Physical Chemistry B*, vol. 126, pp. 9617–9631, Nov. 2022, doi: 10.1021/acs.jpcb.2c05878.

[196] J. P. Perdew, K. Burke, and M. Ernzerhof, "Generalized Gradient Approximation Made Simple," *Phys Rev Lett*, vol. 77, pp. 3865–3868, 1996.

[197] F. Weigend and R. Ahlrichs, "Balanced basis sets of split valence, triple zeta valence and quadruple zeta valence quality for H to Rn: Design and assessment of accuracy," *Physical Chemistry Chemical Physics*, vol. 7, no. 18, pp. 3297–3305, Sep. 2005, doi: 10.1039/b508541a.

[198] F. Weigend, "Accurate Coulomb-fitting basis sets for H to Rn," *Physical Chemistry Chemical Physics*, vol. 8, no. 9, pp. 1057–1065, 2006, doi: 10.1039/b515623h.

[199] M. Dolg, U. Wedig, H. Stoll, and H. Preuss, "Energy-adjusted ab initio pseudopotentials for the first row transition elements," *J Chem Phys*, vol. 86, no. 2, pp. 866–872, 1986, doi: 10.1063/1.452288.

[200] D. Andrae, U. Haubermann, M. Dolg, H. Stoll, and H. Preub, "Energy-adjusted ab initio pseudopotentials for the second and third row transition elements," *Theor Chim Acta*, vol. 77, pp. 123–141, 1990.

[201] M. Dolg, H. Stoll, and H. Preuss, "Energy-adjusted ab initio pseudopotentials for the rare earth elements," *J Chem Phys*, vol. 90, no. 3, pp. 1730–1734, 1989, doi: 10.1063/1.456066.

[202] A. S. Poyraz *et al.*, “Synthesis of cryptomelane type α-MnO2 (K:XMn8O16) cathode materials with tunable K+ content: The role of tunnel cation concentration on electrochemistry,” *J Mater Chem A Mater*, vol. 5, no. 32, pp. 16914–16928, 2017, doi: 10.1039/c7ta03476h.

[203] J. E. Post, R. B. Von Dreele, and P. R. Buseck, “Symmetry and cation displacements in hollandites: structure refinements of hollandite, cryptomelane and priderite.,” *Acta Crystallogr*, vol. B38, no. Part 4, pp. 1056–1065, 1982, doi: 10.1107/s0567740882004968.

[204] N. Kijima, H. Yasuda, T. Sato, and Y. Yoshimura, “Preparation and characterization of open tunnel oxide α-MnO2 precipitated by ozone oxidation,” *J Solid State Chem*, vol. 159, pp. 94–102, 2001, doi: 10.1006/jssc.2001.9136.

[205] C. Sangwichien and G. Aranovich, “Density functional theory predictions of adsorption isotherms with hysteresis loops,” *Colloids Surf A Physicochem Eng Asp*, vol. 206, pp. 313–320, 2002, [Online]. Available: www.elsevier.com/locate/colsurfa

[206] K. S. W. Sing and R. T. Williams, “Review Physisorption Hysteresis Loops and the Characterization of Nanoporous Materials,” *Adsorption Science and Technology*, vol. 22, pp. 773–782, 2004.

[207] H. Morikawa, “Planar Defects of Cu3Se2 Crystals Produced by Solid-State Reaction,” *Jpn J Appl Phys*, vol. 11, pp. 431–436, 1972.

[208] W. Si, Y. Wang, S. Zhao, F. Hu, and J. Li, “A Facile Method for in Situ Preparation of the MnO2/LaMnO3 Catalyst for the Removal of Toluene,” *Environ Sci Technol*, vol. 50, no. 8, pp. 4572–4578, May 2016, doi: 10.1021/acs.est.5b06255.

[209] S. Munirasu, F. Banat, A. Ahmed, and M. Abu, “Intrinsically superhydrophobic PVDF membrane by phase inversion for membrane distillation,” *Desalination*, vol. 417, pp. 77–86, 2017, doi: 10.1016/j.desal.2017.05.019.

[210] M. Kamaz, A. Sengupta, A. Gutierrez, Y. H. Chiao, and R. Wickramasinghe, “Surface modification of PVDF membranes for treating produced waters by direct contact membrane distillation,” *Int J Environ Res Public Health*, vol. 16, no. 5, Mar. 2019, doi: 10.3390/ijerph16050685.

[211] S. Leroch and M. Wendland, “Influence of capillary bridge formation onto the silica nanoparticle interaction studied by grand canonical Monte Carlo simulations,” *Langmuir*, vol. 29, no. 40, pp. 12410–12420, Oct. 2013, doi: 10.1021/la402002f.

[212] B. Torun, C. Kunze, C. Zhang, T. D. Kühne, and G. Grundmeier, “Study of water adsorption and capillary bridge formation for SiO2 nanoparticle layers by means of a combined in situ FT-IR reflection spectroscopy and QCM-D set-up,” *Physical Chemistry Chemical Physics*, vol. 16, no. 16, pp. 7377–7384, Mar. 2014, doi: 10.1039/c3cp54912g.

[213] R. G. Pearson, “Chemical Hardness and Bond Dissociation Energies,” *Journal of American Chemical Society*, vol. 110, pp. 7684–7690, 1988, [Online]. Available: https://pubs.acs.org/sharingguidelines

[214] C. H. Choi, M. W. Chung, H. C. Kwon, S. H. Park, and S. I. Woo, “B, N- and P, N-doped graphene as highly active catalysts for oxygen reduction reactions in acidic media,” *J Mater Chem A Mater*, vol. 1, pp. 3694–3699, Mar. 2013, doi: 10.1039/c3ta01648j.

[215] J. I. Aihara, “Reduced HOMO-LUMO Gap as an Index of Kinetic Stability for Polycyclic Aromatic Hydrocarbons,” *Journal of Physical Chemistry A*, vol. 103, no. 37, pp. 7487–7495, Sep. 1999, doi: 10.1021/jp990092i.

[216] K. Fukui, “Role of Frontier Orbitals in Chemical Reactions,” *Science (1979)*, vol. 218, p. 747, 1982.